Controlling Dephasing of Coupled Qubits via Shared-Bath Coherence

Luke Michael Joseph Hall

A thesis submitted for the degree of Doctor of Philosophy

Cardiff University

August 2025

Abstract

Quantum dots are nanoscale semiconductor crystals in which charge carriers are confined in all three spatial dimensions. The discrete energy levels of quantum dots make them promising candidates for qubits in quantum information processing. However, at any temperature, there are lattice vibrations, known as phonons, in the surrounding material. When a quantum dot is optically excited, an exciton, a bound electron-hole pair, is created and there is an unavoidable coupling of the exciton to the phonons. The interaction of a quantum system with these phonons causes decoherence, limiting the coherence time, which restricts the utility of qubits in quantum information processing applications. In this thesis, the decoherence in a system of two spatially separated, electronically decoupled qubits, with direct or mediated coupling, interacting with a shared three-dimensional bath is investigated. For illustration, Förster or cavity-mediated coupling between semiconductor quantum dots interacting with acoustic phonons is treated. Using the rigorous Trotter decomposition with linked cluster expansion technique, a reduction in decoherence at specific distances between the quantum dots is observed. This reduction results from the collective coupling of the qubits to shared phonon modes, enabled by the coherent properties of the bath. In particular, when the qubit separation is an integer multiple of the phonon wavelength, selected by the energy splitting of the coupled qubit states, there is a reduction in the decoherence. We show that a near-vanishing dephasing rate, which can be referred to as

a one-dimensional regime, can be achieved by utilising strong quantum dot-cavity coupling strengths. We quantify the separations at which the one-dimensional-like regime persists before transitioning to the expected three-dimensional behaviour. To calculate the dynamics of these extended quantum systems, traditional path-integral based tensor-multiplication schemes are not sufficient. To tackle this, an optimisation scheme is developed, using a matrix representation of tensors and their singular value decomposition to filter out unimportant contributions. Importantly, more memory-efficient representations for the tensors exist; however, this approach enables the usage of an extrapolation scheme which approximates the *exact* long-time dynamics. This optimisation dramatically reduces both computational time and memory usage compared with the traditional methods.

List of Publications

The work introduced in this thesis is based on the following works submitted for publication (or soon to be submitted).

- L. M. J. Hall, L. S. Sirkina, A. Morreau, W. Langbein, and E. A. Muljarov, "Controlling dephasing of coupled qubits via shared-bath coherence" Phys. Rev. B 112, 045303 (2025).

- L. M. J. Hall, A. Gisdakis, and E. A. Muljarov, "Optimization of path-integral tensor-multiplication schemes in open quantum systems" (2025), arXiv:2502.15136.

- L. S. Sirkina, L. M. J. Hall, A. Morreau, W. Langbein, and E. A. Muljarov, "Förster transfer between quantum dots in a shared phonon environment: A rigorous approach, revealing the role of pure dephasing" (In Preparation).

The results of this work were also contained in a poster presentation at the following event:

- L. M. J. Hall, L. S. Sirkina, A. Morreau, W. Langbein, and E. A. Muljarov: "Dephasing of Long Distance Coupled Qubits", Optics of Excitons in

Confined Systems (OECS 18) (2023).

- L. S. Sirkina, L. M. J. Hall, A. Morreau, W. Langbein, and E. A. Muljarov: "Förster transfer between coupled quantum dots in a common phonon environment", OECS 18 (2023).

The results were also presented in the following talk:

- "Dephasing of Long Distance Coupled Qubits", Theory Seminar, Cardiff (2024)

Acknowledgements

Firstly, I would like to thank Nan, the love of my life, for always being there for me throughout my university journey, which began almost a decade ago. Your support and love means everything to me.

I am deeply grateful to my supervisor, Egor Muljarov, whose guidance and encouragement have helped me grow both as a researcher and as a person. I will truly miss our weekly meetings, where we shared tea and had wide-ranging discussions that extended well beyond physics.

I would also like to thank my second supervisor, Wolfgang Langbein, for his valuable insights and ideas during our meetings. I especially appreciate the time and care he devoted to commenting on paper drafts.

My sincere thanks go to Liubov Sirkina, with whom I had the pleasure of collaborating throughout much of my PhD—it has been a real joy to work together. I am also grateful to Amy Morreau, who co-supervised my MPhys project with Egor and collaborated in this research.

I would also like to express my appreciation to my brother, Callum Hall, and my friend, Arsenios Gisdakis. Studying alongside them both during our undergraduate years made the journey all the more enjoyable. I am especially grateful to Arsenios for his collaboration on parts of the work presented in this thesis.

Finally, I thank the department for accepting me onto the foundation year ten years ago, giving me a path into studying physics. Coming from a non-traditional educational background, I did not have the qualifications to enter the undergraduate course directly, and at one point, I thought that studying physics might be out of reach. I will always be thankful for the opportunity.

Funding

I acknowledge support from the EPSRC under grant number EP/T517951/1

Contents

Chapter 1

Introduction

When solids are scaled down to the nanometer range, they exhibit dramatically different physical properties compared to their bulk counterparts. One of the most notable changes is observed in the electronic energy structure due to quantum confinement. Semiconductor quantum dots (QDs) are nanoscale semiconductor structures where charge carriers experience quantum confinement in all three spatial dimensions, leading to discrete energy levels—formed when a narrow bandgap material is enclosed within a wider bandgap material. Common material choices include gallium arsenide (GaAs), aluminium gallium arsenide (AlGaAs) and indium gallium arsenide (InGaAs), of which the properties of the latter are used throughout this thesis. In these structures, charge carriers experience three-dimensional (3D) quantum confinement, leading to discrete energy levels [1–3]. These energy levels can be fine-tuned by modifying the QD size and shape [4] making them remarkably versatile for various applications. Excitation of an electron from the valence band (VB) to the conduction band (CB) creates a positively charged quasi-particle called a hole in the VB. In quantum dots, spatial confinement leads to quantised energy levels for both carriers, forming an exciton. The Coulomb interaction between the electron and hole introduces additional corrections to their energies and wave functions, which is not taken into account in this

thesis.

Of particular importance to this thesis is a QDs ability to exhibit coherence between the excited and ground excitonic states, making them a promising candidate for qubits—the basic units of quantum computing.

When QDs are spatially separated and uncoupled, each can act as an independent single-photon emitter. In such systems, if coherence is maintained between the excited and ground states of each individual dot, it enables the emission of indistinguishable photons. This indistinguishability is crucial for two-photon interference effects, which have been observed experimentally [5–7]. Importantly, these results demonstrate that coherence must be preserved within each QD, even in the absence of inter-dot coupling. While coherence in single-dot systems is valuable for generating indistinguishable photons, more complex architectures, such as quantum logic gates, require coupling between multiple QDs. When two QDs are directly coupled, their states hybridise, and the system behaves as a single, extended quantum emitter. In this regime, maintaining coherence between the hybridised states becomes essential, for example in the implementation of two-qubit gates [8, 9]. Long-range qubit interactions can also be mediated via strong coupling to photonic cavities [10], but regardless of the interaction mechanism, preserving coherence in coupled systems remains a fundamental challenge due to unavoidable coupling to the environment [11, 12].

QDs, which are often described as "artificial atoms" due to their discrete energy levels, differ from isolated atoms because they are embedded within a solid-state environment. This leads to interactions with quantised lattice vibrations, known as phonons — which act as a source of decoherence. These exciton-phonon interactions strongly influence the coherence and dynamics of QD systems, as demonstrated by extensive theoretical and experimental research [13–32].

Several mechanisms underlie exciton-phonon interactions in QDs, including defor-

mation potential coupling, piezoelectric coupling, and Fröhlich coupling. Among these, deformation potential coupling to longitudinal acoustic (LA) phonons is typically the dominant source of dephasing at low temperatures [33–35]. Although exceptions do exist, such as GaN-based QDs, where piezoelectric coupling can surpass deformation potential coupling [14]. In contrast, Fröhlich coupling primarily involves longitudinal optical (LO) phonons, which usually contribute little to dephasing in GaAs-based QDs [36] at low temperatures. In particular, below a temperature of 50K, the dominant source of dephasing is the deformation potential coupling [37], phonon anharmonicity [38], and radiative decay.

The interaction between QDs and phonons differs significantly from carrier-phonon interactions in bulk semiconductors. Firstly, there is energy conservation in both QDs and bulk semiconductors, but a strict momentum conservation takes places only in the latter, as QDs break translational symmetry. In bulk materials, phonons often mediate transitions between states of the electronic continuum. However, in QDs, the discrete nature of the energy levels often leads to a mismatch between the energy level differences and the typical phonon energies, known as the phonon bottleneck [39, 40]. As a result, the coupling between QD electronic states via phonons is relatively weak. Instead, on ultrafast timescales (ranging from a few to tens of picoseconds), interactions with acoustic phonons become the dominant mechanism of pure dephasing [13, 41]. The term pure dephasing arises from the fact that, unlike transitions between electronic states, these interactions affect the coherence of electronic states without altering their population.

In fact, following excitation with an ultrafast laser pulse, QD-phonon interactions primarily influence the coherence dynamics of the system. This behaviour is well-described by the exactly-solvable independent boson (IB) model (detailed in Section 2.3), where even at low temperatures, acoustic phonons induce a rapid non-Markovian decay of the QD coherence [42]. This rapid loss of coherence manifests itself as broad side bands, known as the phonon broadband (BB), in the QD absorption spectrum [14].

In systems with additional interactions, such as coupling to optical cavity modes or other QDs, new hybridised states can emerge in the strong-coupling regime. There is a coherent oscillatory exchange of energy between a QD and, for example, a cavity mode [15] described by the Jaynes-Cummings (JC) model (detailed in Section 2.2). This coherent energy transfer is observed as Rabi oscillations, where excitation is periodically exchanged between the QD exciton and a photon in the cavity mode. Phonons modify this interaction, dressing the hybridised QD-cavity states. Unlike bare QD and cavity states, where pure dephasing cannot induce transitions, the hybridised states can experience phonon-mediated transitions, leading to a damping of Rabi oscillations [43–45]. In the frequency domain, this damping appears as a broadening of the zero-phonon line (ZPL), the sharp peak associated with the exciton transition frequency. This damping of the Rabi oscillations is observed as a nearly Markovian long-time decay of the coherences due to real or virtual phonon-assisted transitions [37, 46].

Historically, the dominating source of decoherence in a multi-qubit system inside a cavity was due to the leakage of photons from the cavity due to its low quality factor, causing coupling with the continuum of external photonic modes. Therefore, previous works have focused on exploiting the photonic bath coherent properties to reduce dephasing, such as decoherence-free subspaces of subradiant quantum superpositions [47, 48]. Specifically, the introduction of a second qubit coupled to the same cavity gives rise to a subradiant superposition state that is decoupled from the lossy cavity. However, although the quality factor of optical cavities dramatically increased over the past decade, the coherence times remain limited. As discussed, now acoustic phonons present the major intrinsic source of decoherence in QD systems.

While the interaction of hybridised QD states with a shared environment usually causes their dephasing, one of the key results of this thesis show that the decoherence can be reduced, or completely suppressed, in coupled QD systems. This suppression results from the collective coupling of the QD qubits to the same

phonon modes [49], enabled by the coherent properties of the bath. In particular, when the qubit separation is an integer multiple of the phonon wavelength, selected by the energy splitting of the coupled qubit states, there is a reduction in the decoherence.

To investigate these effects, this thesis explores coherence in multi-QD-cavity systems with acoustic phonon coupling. The core elements are introduced in the next chapter, beginning with a definition of key concepts, followed by a discussion of the JC model to describe light-matter interactions. Next, QD-phonon interactions are explored using the IB model. Both the JC and IB model are exactly solvable, and utilising these models when addressing the problem of phonon-induced dephasing in the multi-QD–cavity systems is natural. However, the combination of the two models presents a significant challenge. To combine the models, Feynman's path-integral formulation provides an effective tool, giving an asymptotically exact solution for the density matrix dynamics. The later chapters of this thesis develop a path-integral technique, combining Trotter's decomposition with linked cluster expansion to treat systems containing multiple QDs coupled to the same phonon bath. These path-integral formulations lead to tensor-multiplication schemes which are computationally expensive, and to address this, this thesis provides an optimisation scheme to reduce computational requirements. The optimisation is based on remapping the tensors as matrices and employing a singular-value decomposition (SVD) scheme to filter out unimportant contributions to reduce memory requirements and computational time.

Chapter 2

Background

2.1 The density matrix and coherences

This thesis focuses on the linear optical response, which we call throughout the linear optical polarisation or more simply, the linear polarisation. In this context, the linear polarisation corresponds to the off-diagonal elements of the density matrix representing the coherences within the system. To understand this concept, it is useful to introduce the the density matrix and clarify the significance of its various elements.

The density matrix, denoted ρ, is a fundamental tool in quantum mechanics used to describe the state of a quantum system, especially when dealing with mixed states or systems subject to environmental interactions. It generalises the concept of a wave function $|\Psi\rangle$ to take into account statistical mixtures of quantum states. For a system with a set of basis states $|i\rangle$, the density matrix is expressed as

$$\rho_{\text{total}} = \sum_{i,j} \rho_{ij} \left|i\right\rangle \left\langle j\right|, \tag{2.1.1}$$

where $\rho_{ij} = \langle i| \rho |j\rangle$ are the elements of the matrix. The elements ρ_{ij} contain

information about the populations and coherences of the system. The diagonal elements, ρ_{ii}, represent the population of the system in the corresponding basis state $|i\rangle$. Physically, this is the probability of finding the system in state $|i\rangle$. The off-diagonal elements, ρ_{ij} $(i \neq j)$, represent the coherences between the basis states $|i\rangle$ and $|j\rangle$, encoding the quantum superpositions. Since this thesis focuses on the linear polarisation, emphasis is placed on the off-diagonal elements. Their evolution reveals how the system maintains or loses coherence due to interactions with the environment. However, when a system interacts with a phonon environment, the full density matrix ρ_{total} contains both the system and phonon degrees of freedom, making it impractical to work with ρ_{total} directly due to the large phonon Hilbert space. Instead, the reduced density matrix describing only the system is used, given by

$$\rho_{\text{s}} = \text{Tr}\{\rho_{\text{total}}\}_{\text{ph}}, \tag{2.1.2}$$

where the phonon degrees of freedom are traced out. This results in an effective evolution for ρ_{s} that incorporates dissipative and decoherence effects due to phonon interactions, rather than explicitly including phonon states.

For illustration, consider a QD-cavity system without phonons, where the reduced density matrix (equivalent to the full density matrix in this case) can be expressed in a basis of three possible states (considering only single particle states). We have the state $|0\rangle$, which represents the absolute ground state of the exciton and cavity, the first excited exciton state $|X\rangle$ and the cavity with a single photon $|C\rangle$. Then, the density matrix of the QD-cavity system is given by

$$\rho(t) = \sum_{i,j=0,X,C} \rho_{ij}(t) \left|i\right\rangle \left\langle j\right|, \tag{2.1.3}$$

where the time dependent coefficients are expressed as $\rho_{ij}(t)$.

Introducing now the exciton or cavity creation ($d^\dagger$ or $a^\dagger$) and destruction operators (d or a), defined as

$$d^\dagger = \left|X\right\rangle \left\langle 0\right|, \qquad d = \left|0\right\rangle \left\langle X\right|, \tag{2.1.4}$$

$$a^\dagger = |C\rangle\langle 0|\,, \qquad a = |0\rangle\langle C|\,, \tag{2.1.5}$$

the creation or destruction effects of these operators can be seen by applying them on the system states

$$d^\dagger|0\rangle = |X\rangle\langle 0|0\rangle = |X\rangle\,, \qquad d|X\rangle = |0\rangle\langle X|X\rangle = |0\rangle$$

and

$$a^\dagger|0\rangle = |C\rangle\langle 0|0\rangle = |C\rangle\,, \qquad a|C\rangle = |0\rangle\langle C|C\rangle = |0\rangle\,,$$

where the orthonormality of the states has been used, $\langle n|m\rangle = \delta_{nm}$, where δ_{nm} is the Kronecker delta. In addition, note that the states are limited to single particle states, such that $a^\dagger|X\rangle = d^\dagger|C\rangle = 0$. Furthermore, applying a destruction operator onto the ground state gives zero, i.e. $d|0\rangle = a|0\rangle = 0$.

The expectation value of an operator $\hat{O}$ in the density matrix formalism is given by the trace formula,

$$\langle\hat{O}\rangle = \mathrm{Tr}\Big\{\rho\hat{O}\Big\} \tag{2.1.6}$$

and by definition the polarisation is

$$\mathrm{P}(t) = \mathrm{Tr}\{\rho(t)c\}, \tag{2.1.7}$$

where c is the destruction operator associated with the measurement channel. Since the polarisation that is measured is determined by the operator c, if it is d (a), then the polarisation will represent the coherence between the first excited excitonic (photon) state, $|X\rangle$ ($|C\rangle$), and the ground state $|0\rangle$. To get a non-trivial polarisation, a pulsed excitation is applied to the ground state of the system and has the form

$$H_{\mathrm{ext}}(t) = \mathcal{V}\delta(t), \tag{2.1.8}$$

with

$$\mathcal{V} = \mu(\tilde{c}^\dagger + \tilde{c}), \tag{2.1.9}$$

where μ is a constant, and $\tilde{c}^\dagger$ is a general creation operator, referring to either

the exciton creation operator ($d^\dagger$) or cavity photon creation operator ($a^\dagger$). The operator chosen depends on the mode of excitation being considered. The reason both the creation and destruction operator appears in $\mathcal{V}$ is due to Hermiticity, and consequently the excitation is symmetrically applied to the density matrix. The excitation is applied at time $t = 0$, and the density matrix of the QD-cavity system immediately after the pulsed excitation is given by the following transformation,

$$\rho(0_+) = e^{-i\int_{-\infty}^{\infty} H_{\text{ext}}(t')dt'}\rho(-\infty)e^{i\int_{-\infty}^{\infty} H_{\text{ext}}(t')dt'} = e^{-i\mathcal{V}}\rho(-\infty)e^{i\mathcal{V}}. \tag{2.1.10}$$

Here $\rho(-\infty)$ is the density matrix of the system in the fully unexcited state, $|0\rangle\langle 0|$. By expanding the operator $e^{-i\mathcal{V}}$ as a Taylor series and applying it to the ground state $|0\rangle$, the effect of the excitation can be seen. Assuming the excitation occurs in the excitonic channel, the Taylor series gives

$$e^{-i\mu(d^\dagger+d)}|0\rangle = \left(1 - i\mu(d^\dagger + d) - \frac{\mu^2}{2}(d^\dagger + d)^2 + ...\right)|0\rangle \ . \tag{2.1.11}$$

For a weak pulse the expansion can be truncated to first order, yielding $|0\rangle - i\mu|X\rangle$, therefore creating a coherent superposition of the ground state $|0\rangle$ and the single-exciton state $|X\rangle$. In the case of cavity channel excitation, this creates a Glauber coherent state [50], however we reduce consideration to single-particle effects and therefore it is only a superposition of $|0\rangle$ and $|C\rangle$ (one-photon cavity state). The following time-evolution of the density matrix immediately after the pulsed excition is given by standard time-evolution in the Schrödinger representation (see Appendix A for details on representations),

$$\rho(t) = e^{-iHt}\rho(0_+)e^{iHt} = e^{-iHt}e^{-i\mathcal{V}}\rho(-\infty)e^{i\mathcal{V}}e^{iHt}, \tag{2.1.12}$$

where H is the system Hamiltonian. By definition, using Eq. (2.1.7), the polarisation is

$$\mathrm{P}(t) = \mathrm{Tr}\{e^{-iHt}e^{-i\mathcal{V}}\rho(-\infty)e^{i\mathcal{V}}e^{iHt}c\}. \tag{2.1.13}$$

However, in this thesis, Eq. (2.1.13) is reduced to the linear optical polarisation by accounting for only terms linear in μ. The linear optical polarisation is then given

by

$$\mathrm{P_L}(t) = \mathrm{Tr}\{e^{-iHt}\mathcal{V}\rho(-\infty)e^{iHt}c\}, \tag{2.1.14}$$

where the unimportant factor $-i\mu$ has been dropped. Eq. (2.1.14) describes the linear response to a pulsed excitation in the channel determined by $\tilde{c}^\dagger$ and $\tilde{c}$ in $\mathcal{V}$, and subsequent measurement in the channel determined by c. For the rest of the thesis, the subscript L is dropped since we only consider the linear response.

2.2 Jaynes-Cummings (JC) model

We use the Jaynes-Cummings model to capture the essential features of light-matter interaction by describing the coupling between a single fermionic two-level system and a bosonic photon mode, in the absence of phonons [51]. In the full JC model, multiple excitation levels can exist, where higher-energy states involve additional cavity photons. These give rise to a series of coupled states forming what is known as the Jaynes-Cummings ladder [52]. Here we consider an excitonic system with only a ground state $|0\rangle$ and a single excited state $|X\rangle$, forming a two-level system, coupled to a single mode of a photonic cavity $|C\rangle$, where a single excitation is shared between the exciton and the cavity mode. The Hamiltonian of this exciton-cavity system is given by (with $\hbar = 1$ taken throughout)

$$H = \omega_X d^\dagger d + \omega_C a^\dagger a + g(a^\dagger d + d^\dagger a), \tag{2.2.1}$$

where $d^\dagger(a^\dagger)$ is the exciton (photon) creation operator, $\omega_X(\omega_C)$ is the exciton (photon) energies and g is the exciton-cavity coupling strength. The exciton and cavity photon frequencies are, in general, complex and written as

$$\omega_{X,C} = \Omega_{X,C} - i\gamma_{X,C}. \tag{2.2.2}$$

The imaginary component, γ_X, of the exciton energy ω_X represents the phenomenological ZPL linewidth, which accounts for the radiative decay of the exciton. Similarly, γ_C corresponds to the cavity losses, due to photons escaping from the cavity.

The coupling term g in the JC model originates from the interaction between the optical transition dipole moment of the QD exciton and the quantised electric field of the cavity mode. The transition dipole moment is defined as

$$\boldsymbol{\mu} = \langle X | \, \mathbf{d} \, | 0 \rangle \, , \tag{2.2.3}$$

where $\mathbf{d}$ is the dipole operator. This transition dipole moment depends crucially on the overlap between electron and hole wave functions. The cavity confines a single quantised mode of the electromagnetic field described by the operator

$$\mathbf{E}(\mathbf{r}) = E_0 \mathbf{u}(\mathbf{r})(a + a^\dagger), \tag{2.2.4}$$

where $E_0 = \sqrt{\omega_C / 2\epsilon_0 V}$ represents the vacuum field amplitude with V being the effective mode volume. Here, $\mathbf{u}(\mathbf{r})$ denotes the normalised spatial mode profile (e.g. a standing wave pattern in a Fabry-Pérot cavity). The Hermitian form $(a + a^\dagger)$ emerges naturally from the canonical quantisation of the field. The light-matter interaction Hamiltonian

$$H_{\text{int}} = -\mathbf{d} \cdot \mathbf{E} \tag{2.2.5}$$

couples the exciton dipole moment to the cavity field. Expanding the dipole operator in the excitonic basis yields

$$\mathbf{d} = \boldsymbol{\mu} \, | X \rangle \langle 0 | + \boldsymbol{\mu}^* \, | 0 \rangle \langle X | \, , \tag{2.2.6}$$

where the permanent dipole terms are omitted since they do not contribute to optical transitions. Substitution into the interaction Hamiltonian Eq. (2.2.5) leads to four interaction terms: $-(\boldsymbol{\mu} \cdot \mathbf{u} E_0) \, | X \rangle \langle 0 | \, a$ and $-(\boldsymbol{\mu}^* \cdot \mathbf{u}^* E_0) \, | 0 \rangle \langle X | \, a^\dagger$ describing energy-conserving processes (photon emission with exciton recombination and photon absorption with exciton creation), along with $-(\boldsymbol{\mu} \cdot \mathbf{u}^* E_0) \, | X \rangle \langle 0 | \, a^\dagger$ and $-(\boldsymbol{\mu}^* \cdot \mathbf{u} E_0) \, | 0 \rangle \langle X | \, a$ representing non-energy-conserving counter-rotating terms. The rotating wave approximation (RWA) provides a simplification by keeping only the energy-conserving terms. In the interaction picture, the energy-conserving terms evolve as $e^{\pm i(\omega_X - \omega_C)t}$ (slow oscillations), while the counter-rotating terms

oscillate rapidly as $e^{\pm i(\omega_X+\omega_C)t}$. When the coupling strength g satisfies

$$g \ll \Omega_X, \Omega_C, \tag{2.2.7}$$

where Ω is the real component, these counter-rotating terms average to zero on the system's characteristic timescale $\sim 1/g$ and can be neglected. This approximation yields the simplified interaction Hamiltonian

$$H_{\text{int}} \approx g(a^\dagger \left|0\right\rangle \left\langle X\right| + a \left|X\right\rangle \left\langle 0\right|), \tag{2.2.8}$$

which is equivalent to the interaction term in Eq. (2.2.1) and where the coupling strength

$$g = \boldsymbol{\mu} \cdot \mathbf{u} E_0 \propto \frac{\mu}{\sqrt{V}} \tag{2.2.9}$$

depends on the transition dipole moment, vacuum field amplitude, and mode overlap. The coupling strength g fundamentally reflects the strength of the overlap between the exciton's transition dipole moment and the cavity's vacuum electric field, while the RWA's validity requires the coupling to be much smaller than the system's natural frequencies. Beyond this regime, such as in ultrastrong coupling situations, one must consider the full quantum Rabi model that retains the counter-rotating terms. As outlined in the previous section, for a single-particle treatment (first rung of the JC ladder), the exciton and cavity operators can be expressed in the $\{\left|X\right\rangle, \left|C\right\rangle\}$ basis, which expressed in matrix form, the Hamiltonian Eq. (2.2.1), is given by

$$H = \begin{pmatrix} \omega_X & g \\ g & \omega_C \end{pmatrix}. \tag{2.2.10}$$

When a pulsed excitation is applied to the system, the linear optical polarisation $\mathrm{P_L}(t)$, determined from Eq. (2.1.13), for the JC model is given by (see Appendix B for the full derivation)

$$\mathrm{P}_{jk}(t) = \left\langle j\right| e^{-iHt} \left|k\right\rangle, \tag{2.2.11}$$

where k represents the excitation channel and j is the measurement channel. Eq. (2.2.11), which accounts for all possible combinations of excitation and mea-

surement channels, expressed in matrix form is

$$\hat{\mathrm{P}}(t) = \begin{pmatrix} \mathrm{P_{XX}}(t) & \mathrm{P_{XC}}(t) \\ \mathrm{P_{CX}}(t) & \mathrm{P_{CC}}(t) \end{pmatrix} = \hat{Y}^{-1} \begin{pmatrix} e^{-i\omega_1 t} & 0 \\ 0 & e^{-i\omega_2 t} \end{pmatrix} \hat{Y}, \tag{2.2.12}$$

where e^{-iHt} has been evaluated by diagonalising the JC Hamiltonian matrix, given in Eq. (2.2.10), with the help of the eigenvector matrices $\hat{Y}$ and $\hat{Y}^{-1}$ defined as

$$\hat{Y} = \begin{pmatrix} \alpha & -\beta \\ \beta & \alpha \end{pmatrix}, \tag{2.2.13}$$

where

$$\alpha = \frac{\Delta}{\sqrt{\Delta^2 + g^2}}, \tag{2.2.14}$$

$$\beta = \frac{g}{\sqrt{\Delta^2 + g^2}}, \tag{2.2.15}$$

and $\Delta = \sqrt{\delta^2 + g^2} - \delta$ with $\delta = \frac{1}{2}(\omega_X - \omega_C)$ being half of the detuning. The eigenenergies $\omega_{1,2}$ are given by

$$\omega_{1,2} = \frac{\omega_X + \omega_C}{2} \mp \sqrt{g^2 + \delta^2}, \tag{2.2.16}$$

which are complex in general and can therefore be written as $\omega_{1,2} = \Omega_{1,2} - i\gamma_{1,2}$. Here, $\Omega_{1,2}$ are the real eigenenergies and $\gamma_{1,2}$ are the linewidths. Physically, the exciton-cavity coupling parameter g is mixing the exciton and cavity photon modes, resulting in upper (2) and lower (1) polariton states.

2.2.1 Weak and strong coupling regimes

In this section, the influence of the term $\mp\sqrt{g^2 + \delta^2}$ within Eq. (2.2.16) is investigated to identify the weak and strong coupling regimes. Firstly, consider the case of zero detuning for simplicity ($\Omega_X = \Omega_C$), Eq. (2.2.16) can then be written as

$$\omega_{1,2} = \Omega_C - \frac{i}{2}(\gamma_X + \gamma_C) \mp \frac{1}{2}\sqrt{4g^2 - (\gamma_X - \gamma_C)^2}. \tag{2.2.17}$$

Focusing on the square root term, if $g < \frac{1}{2}|\gamma_X - \gamma_C|$, then the splitting in $\omega_{1,2}$ is purely imaginary. As a result, the real parts of the eigenenergies, $\Omega_{1,2}$, are degenerate, which defines the weak coupling regime. In contrast, if $g > \frac{1}{2}|\gamma_X - \gamma_C|$, the square root becomes real, leading to a real energy splitting. Therefore, the real eigenenergies $\Omega_{1,2}$ are non-degenerate, characterising the strong coupling regime.

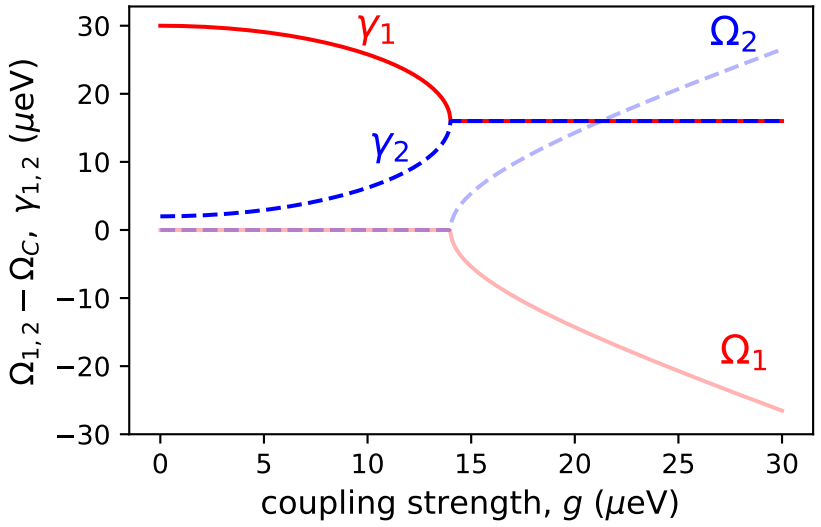

Figure 2.1: Real and imaginary components of the upper (2) and lower (1) polariton eigenenergies for the case of zero detuning ($\Omega_X = \Omega_C$) with $\gamma_X = 2\,\mu$eV and $\gamma_C = 30\,\mu$eV.

Fig. 2.1 shows the effect of increasing the exciton–cavity coupling strength g on the real and imaginary parts of the eigenvalues of the JC Hamiltonian. These correspond to the energies $\Omega_{1,2}$ and linewidths $\gamma_{1,2}$ of the polariton states. At low g, there is no clear energy splitting, and the system remains in the weak coupling regime. In this regime, although enhanced spontaneous emission — known as the Purcell effect [53] — can occur due to the presence of the lossy cavity, it is not visible in the eigenvalues of this diagonalised Hamiltonian. Instead, the imaginary parts $\gamma_{1,2}$ simply reflect the mixing of the exciton and cavity linewidths γ_X and γ_C, and there is only one distinct eigenenergy. Physically, in the weak coupling regime the emission spectrum consists of a single broadened peak (at or near the cavity resonance) with a decay rate faster than the bare exciton lifetime, the enhancement factor being given by the Purcell factor $F_P \propto Q/V$, where Q is the

cavity quality factor and V the mode volume. This is a purely irreversible process without coherent Rabi oscillations.

As g increases further, the eigenstates begin to hybridise more significantly, and at a specific value of g, there is an exceptional point resulting in the formation of two branches, known as polariton branches. This marks the onset of the strong coupling regime. The value at which this occurs is observed to be $g \approx 14\,\mu\text{eV}$ for the parameters used here, but is dependent on the broadening parameters $\gamma_{X,C}$. In strong coupling, the emission spectrum shows two well-resolved peaks (upper and lower polaritons) whose splitting follows the well-known avoided crossing as a function of exciton–cavity detuning. In the time domain, this corresponds to a reversible exchange of energy between the exciton and cavity mode at the Rabi frequency.

The difference between the polariton eigenenergies is known as the Rabi splitting, which for $g \gg \delta$ is simply given by

$$\Delta\Omega = \Omega_2 - \Omega_1 \approx 2g, \tag{2.2.18}$$

and is often referred to as the nominal Rabi splitting. There is a timescale associated with the coherent exchange of energy between the polariton states, called the characteristic polariton timescale, τ_{JC}, and is defined as

$$\tau_{\text{JC}} = \frac{2\pi}{\Delta\Omega}, \tag{2.2.19}$$

in general. This is the period of the Rabi oscillations, and in the specific case of zero detuning, $\tau_{\text{JC}} \approx \pi/g$.

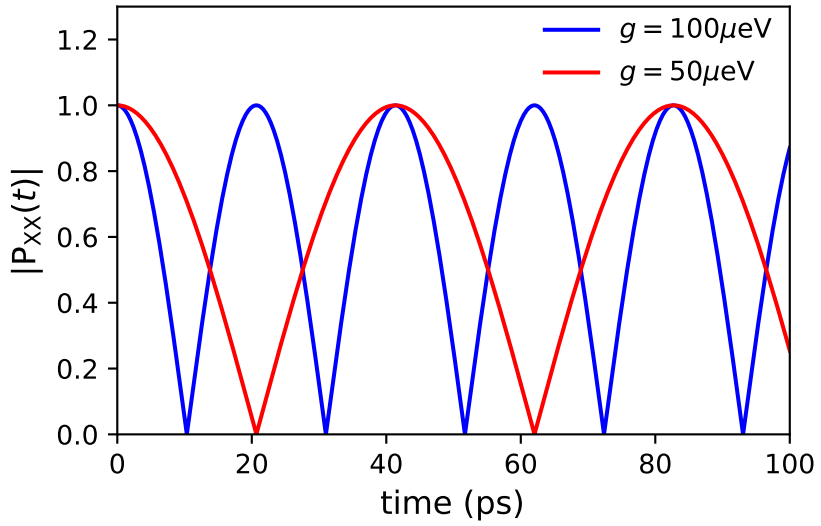

Figure 2.2: The absolute value of the linear polarisation, $|\mathrm{P_{XX}}(t)|$, in the JC model in the strong-coupling regime, according to Eq.(2.2.12). The calculations are performed for zero detuning ($\Omega_X = \Omega_C$) and no added damping ($\gamma_{X,C} = 0$) for two exciton-cavity coupling strengths, $g = 50\,\mu$eV (red) and $100\,\mu$eV (blue).

Fig. 2.2 shows the linear polarisation for excitation and measurement in the excitonic channel $|\mathrm{P_{XX}}(t)|$. The oscillations show the coherent exchange of energy between the exciton and cavity, with the frequency determined by the Rabi splitting given by Eq. (2.2.18), related to the timescale Eq. (2.2.19). The larger exciton–cavity coupling strength of $100\,\mu$eV shows an oscillation frequency twice that of the lower, $g = 50\,\mu$eV coupling, as expected. Notably, there is no gradual loss of coherence, since there are no phonons and no phenomelogical dampings ($\gamma_{X,C}$) added.

Experimentally, some controllable parameters in the JC model are: g, which can be increased by reducing the cavity mode volume and improving the spatial and spectral overlap between the exciton and the cavity mode. γ_C, which depends on the cavity Q-factor and can be lowered via improved fabrication or mirror reflectivity; γ_X, which is set by the intrinsic exciton lifetime, and can be reduced at low temperatures or in high-quality QDs. The detuning, $\Delta = \Omega_X - \Omega_C$, can be tuned via temperature, electric field (quantum confined stark effect), or mechanical strain since these mostly affect the exciton transition energy and not the cavity.

Transitioning from weak to strong coupling requires increasing g and/or reducing γ_X and γ_C. The onset of strong coupling is confirmed experimentally by the observation of a resolvable Rabi splitting in the spectrum or coherent Rabi oscillations in the time domain, in contrast to the single broadened peak characteristic of weak coupling.

Using the polarisation, given by Eq.(2.2.12), the absorption spectra can be found by taking the real component of the Fourier transform (FT) of $\hat{\mathrm{P}}(t)$, see Appendix C for details. Considering only excitation and measurement in the exciton mode, i.e. $\mathrm{P_{XX}}(t)$, the absorption in the exciton mode under exciton feeding is given by

$$\mathrm{A_{XX}}(\omega) = \mathrm{Re}\left\{\frac{i\alpha^2}{\omega-\omega_1} + \frac{i\beta^2}{\omega-\omega_2}\right\}, \tag{2.2.20}$$

which is just two Lorentzian broadened lines, corresponding to the polariton states.

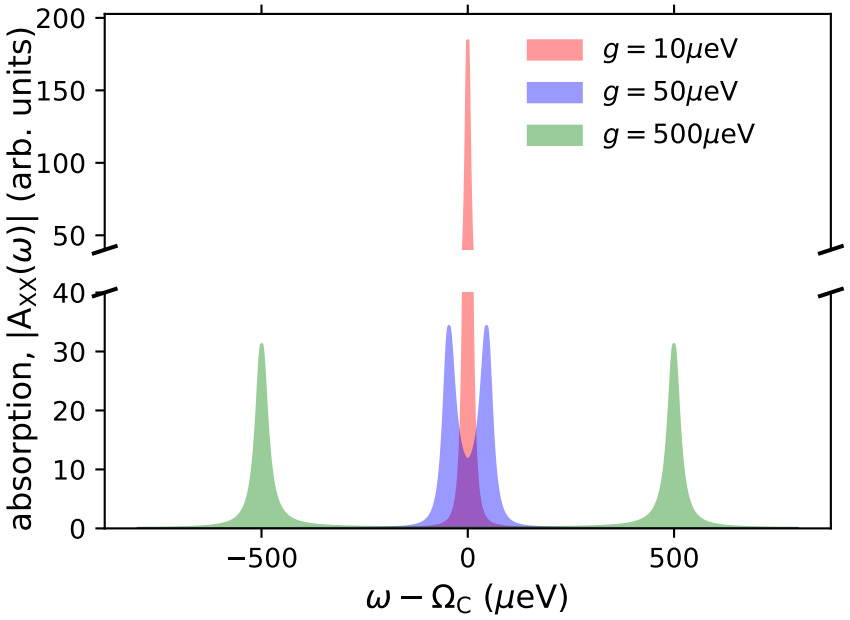

Figure 2.3: Absorption spectra, $\mathrm{A_{XX}}(\omega)$, for zero detuning between the exciton and cavity modes ($\Omega_X = \Omega_C$) for three different exciton-cavity coupling strengths, $g = 10$, 50 and 500 μeV. The phenomenological dampings used for a finite ZPL width are $\gamma_X = 2\,\mu$eV and $\gamma_C = 30\,\mu$eV.

Fig. 2.3 shows the absorption spectra $|\mathrm{A_{XX}}(\omega)|$ for three different coupling strengths

g. For low g ($10\,\mu$eV), there is only one distinct Lorentzian profile, as expected, due to the degeneracy of the real eigenenergies in the weak coupling regime. Physically, this is reasonable, since it shows the absorption is occurring at an energy of $\omega = \Omega_C = \Omega_X$ in the case of zero detuning, meaning that light is being absorbed at the transition frequency of the exciton, as one would expect for no/weak coupling to the cavity mode. For the spectra corresponding to larger g, there are clearly two distinct peaks which is a signature of the strong coupling regime. These peaks are located at the real eigenenergies of the polariton states $\Omega_{1,2}$ and have linewidths $\gamma_{1,2}$, where the separation between the peaks is approximately given by the Rabi splitting $2g$. Furthermore, the linewidths of the Lorentzian profiles appear to be the same, as shown in Fig. 2.1, consistent with Eq.2.2.17. To summarise, in the strong-coupling regime, the exciton and cavity photon form a hybridised quasiparticle called a polariton. Polaritons have two distinct eigenenergies, referred to as the upper polariton (UP) and lower polariton (LP) branches. Physically, this means that energy is coherently exchanged between the exciton and the photon, leading to the joint absorption and emission of light.

The Jaynes-Cummings model will be used later as part of a model that includes the presence of the phonon environment in QD-cavity or multi-QD systems.

2.3 Independent boson (IB) model

The next step is to examine the independent boson model, an exactly solvable model that successfully explains phonon-induced dephasing in QDs [54]. We consider a polaron, which is formed when a single QD couples to bulk acoustic phonons [13]. The coherence of an exciton in a QD is fundamentally limited by its interaction with phonons in the surrounding lattice. This interaction arises because lattice vibrations modify the crystal's periodic potential, leading to shifts in the electronic band edges. For acoustic phonons, the dominant coupling mechanism is the deformation potential. The relevant lattice quantity is the local volumetric strain associated with lattice displacement $\mathbf{u}$, given by $\nabla \cdot \mathbf{u}$. This strain field in-

duces energy shifts in the conduction and valence bands given by $\Delta E_c = D_c \nabla \cdot \mathbf{u}$ and $\Delta E_v = D_v \nabla \cdot \mathbf{u}$, respectively, where D_c and D_v are the deformation potentials. The total shift for the exciton energy is then $\Delta E_X = \Delta E_c - \Delta E_v$, where the negative sign accounts for the fact that a given strain has opposite effects on electrons and holes. This coupling mechanism is highly selective and the deformation potential interaction primarily involves LA phonons. Transverse acoustic (TA) phonons are neglected as their shear strain ($\nabla \cdot \mathbf{u} = 0$) results in negligible coupling via this mechanism. Optical phonons are also disregarded, as they are not thermally populated at the low operating temperatures considered. In GaAs QDs, optical phonon modes have high energies ($\sim 36\,\text{meV}$) which corresponds to around room temperature. Having established the deformation-induced energy shifts, the interaction Hamiltonian term for an exciton can be expressed as

$$H_{\text{X}-\text{ph}} = D_c(\nabla \cdot \mathbf{u}(\mathbf{r}_\text{e})) - D_v(\nabla \cdot \mathbf{u}(\mathbf{r}_\text{h}))\,, \tag{2.3.1}$$

where $\mathbf{u}(\mathbf{r})$ is the phonon displacement field at position $\mathbf{r}$. The displacement field for LA phonons is quantised as

$$\mathbf{u}(\mathbf{r}) = \sum_{\mathbf{q}} \sqrt{\frac{1}{2\rho_m \Omega \omega_q}} (b_{\mathbf{q}} + b^\dagger_{-\mathbf{q}}) \hat{\mathbf{q}} e^{i\mathbf{q}\cdot\mathbf{r}}\,, \tag{2.3.2}$$

where $b^\dagger_{\mathbf{q}}$ is the bosonic creation operator of a bulk phonon mode with the momentum $\mathbf{q}$ and frequency ω_q (denoting $q = |\mathbf{q}|$). $\hat{\mathbf{q}}$ is the unit vector along $\mathbf{q}$ and $\omega_q = v_s q$ is the phonon energy, assuming a linear dispersion. The linear dispersion assumption is valid as the LA branch is well approximated by a straight line near $q = 0$ (long wavelength limit). Deviations from this approximation occur near the Brillouin zone edges, but those higher energy phonons contribute negligibly at the low temperatures considered here. ρ_m is the material mass density, v_s is the sound velocity in the material and Ω is the sample volume. The functional form of Eq. (2.3.2) remains the same across materials, provided deformation potential coupling dominates and linear dispersion holds, though parameters like ρ_m and v_s vary. The model in this thesis uses realistic InGaAs QD parameters, which can be

found in Table 2.1. Taking the divergence $\nabla \cdot \mathbf{u}$ gives:

$$\nabla \cdot \mathbf{u}(\mathbf{r}) = i \sum_{\mathbf{q}} \sqrt{\frac{q^2}{2\rho_m \Omega \omega_q}} \left(b_{\mathbf{q}} + b^\dagger_{-\mathbf{q}} \right) e^{i\mathbf{q}\cdot\mathbf{r}}. \tag{2.3.3}$$

Projecting onto the exciton wavefunction $\Psi_X(\mathbf{r}_e, \mathbf{r}_h)$, the interaction Hamiltonian is:

$$H_{\text{X-ph}} = \int d\mathbf{r}_e \int d\mathbf{r}_h \, |\Psi_X(\mathbf{r}_e, \mathbf{r}_h)|^2 \left[D_c(\nabla \cdot \mathbf{u}(\mathbf{r}_e)) - D_v(\nabla \cdot \mathbf{u}(\mathbf{r}_h)) \right]. \tag{2.3.4}$$

Substituting $\nabla \cdot \mathbf{u}$ into the interaction Hamiltonian, we are able to write it as

$$H_{\text{X-ph}} = \sum_{\mathbf{q}} (\lambda_{\mathbf{q}} b_{\mathbf{q}} + \lambda^*_{\mathbf{q}} b^\dagger_{-\mathbf{q}}) d^\dagger d \,, \tag{2.3.5}$$

where $d^\dagger d = |X\rangle \langle X|$ is the projector onto the exciton state, reflecting the fact that the phonons only couple to the system when the exciton is present. The coupling element $\lambda_{\mathbf{q}}$ is

$$\lambda_{\mathbf{q}} = i \sqrt{\frac{q^2}{2\rho_m \Omega \omega_q}} \mathcal{D}(\mathbf{q}) \,, \tag{2.3.6}$$

and $\mathcal{D}(\mathbf{q})$ is the exciton-phonon form factor, given by

$$\mathcal{D}(\mathbf{q}) = \int d\mathbf{r}_e \int d\mathbf{r}_h |\Psi_X(\mathbf{r}_e, \mathbf{r}_h)|^2 \left(D_c e^{i\mathbf{q}\cdot\mathbf{r}_e} - D_v e^{i\mathbf{q}\cdot\mathbf{r}_h} \right). \tag{2.3.7}$$

Using the linear dispersion of LA phonons and neglecting the factor i, since only $|\lambda_{\mathbf{q}}|^2$ matters physically, we find for the exciton-phonon coupling element

$$\lambda_{\mathbf{q}} = \frac{\sqrt{q}\mathcal{D}(\mathbf{q})}{\sqrt{2\rho_m \Omega v_s}}. \tag{2.3.8}$$

The coupling term Eq. (2.3.8) enables computation of the spectral density, which characterises the bath's influence. The phonon spectral density is defined as $J(\omega) = \sum_{\mathbf{q}} |\lambda_{\mathbf{q}}|^2 \delta(\omega - \omega_q)$, which is effectively the exciton-phonon coupling strength weighted by the phonon density of states (the derivation is provided in Appendix H). From Appendix H, it is worth noting that for LA phonons the density of states contributes an ω^2 term, and the exciton-phonon coupling $|\lambda_{\mathbf{q}}|^2$ contributes ω, which

results in the phonon spectral density having a super-ohmic form of ω^3. This super-ohmic form means low-frequency phonons couple much more weakly to the exciton and results in the dominant interactions coming from higher energy phonons, up to a cut-off value set by the finite QD size. This super-ohmic spectral density creates a structured environment where a specific, narrow range of phonon modes around the cut-off frequency dominates the interaction with the exciton. In fact, the structured environment introduces finite bath correlation times, leading to memory effects and non-Markovian dynamics. A flat spectral density corresponds to a bath having no correlation time, i.e. it "forgets" instantly, so the system only displays Markovian dynamics. While deformation potential coupling to LA phonons yields a super-ohmic (ω^3) form, other mechanisms such as piezoelectric coupling can produce ohmic (ω) behaviour.

Having established the microscopic interaction between the QD exciton and LA phonons, we now turn to the IB model, which describes this system with the following Hamiltonian:

$$H = H_{\text{ph}} + (\omega_X + V)d^\dagger d, \tag{2.3.9}$$

where as before, $d^\dagger(d)$ is the exciton creation (annihilation) operator, and ω_X is the exciton energy. The energy of the phonon continuum is given by

$$H_{\text{ph}} = \sum_{\mathbf{q}} \omega_q b^\dagger_{\mathbf{q}} b_{\mathbf{q}}, \tag{2.3.10}$$

and the exciton-phonon coupling by

$$V = \sum_{\mathbf{q}} \lambda_{\mathbf{q}} (b_{\mathbf{q}} + b^\dagger_{-\mathbf{q}}), \tag{2.3.11}$$

as shown in Eq. (2.3.5). The coupling of the exciton with the phonon mode $\mathbf{q}$ is given by the matrix element $\lambda_{\mathbf{q}}$, which depends on the material parameters and exciton wave function (details of the specific form given in Appendix H). While the IB model effectively accounts for a major source of non-Markovian pure dephasing [37], it does not capture the broadening of the ZPL, a limitation arising from the

linear system-bath coupling.

Applying the formalism of open quantum systems [55], the exciton can be considered as the system and the phonons as the environment. The Hilbert space $\mathcal{H}$ of the combined system and environment is given by the tensor product ($\otimes$) of the excitonic Hilbert space $\mathcal{H}^{(\mathrm{X})}$ and phonon Hilbert space $\mathcal{H}^{(\mathrm{ph})}$,

$$\mathcal{H} = \mathcal{H}^{(\mathrm{X})} \otimes \mathcal{H}^{(\mathrm{ph})}. \tag{2.3.12}$$

Likewise, the density matrix of the combined system, which is used to find the polarisation, is given by the tensor product between the density matrices of the excitonic system and phonon environment,

$$\rho(t) = \rho_{\mathrm{X}}(t) \otimes \rho_{\mathrm{ph}}(t). \tag{2.3.13}$$

The density matrix before any excitation, $\rho(-\infty)$, is the density matrix of the fully unexcited system,

$$\rho(-\infty) = |0\rangle \langle 0| \otimes \rho_{\mathrm{ph}}, \tag{2.3.14}$$

consisting of the absolute ground state of the exciton and the phonon environment in thermal equilibrium, described by the density matrix

$$\rho_{\mathrm{ph}} = \frac{e^{-\beta H_{\mathrm{ph}}}}{\mathrm{Tr}\{e^{-\beta H_{\mathrm{ph}}}\}_{\mathrm{ph}}}, \tag{2.3.15}$$

where $\beta = \frac{1}{k_B T}$ with T being the temperature and k_B is the Boltzmann constant. The subscript ph on the trace refers to the trace being taken over all phonon states.

As previously mentioned in the Sec.2.2, a pulsed excitation is applied at $t = 0$ to get a non-trivial polarisation. However, the pulsed excitation Eq. (2.1.9) containing $\tilde{c}^\dagger(\tilde{c})$ must be $d^\dagger(d)$, the exciton creation (destruction) operator, since the cavity does not exist in this model:

$$\mathcal{V} = \mu(d^\dagger + d). \tag{2.3.16}$$

The following time-evolution of the density matrix is once again given by the Schrödinger representations time evolution, as in Eq.(2.1.12). Then, an expression for the linear optical polarisation is obtained by substituting the relevant quantities into Eq.(2.1.13) (see Appendix B for full derivation), giving

$$\mathrm{P_{XX}}(t) = e^{-i\omega_{\mathrm{X}}t}\langle U(t)\rangle_{\mathrm{ph}}, \tag{2.3.17}$$

where $\langle ...\rangle_{\mathrm{ph}}$ is the expectation value taken over all phonon states in thermal equilibrium and $U(t) = e^{iH_0t}e^{-iHt}$ is the time-evolution operator in the interaction representation. The subscript denoting exciton channel excitation and measurement is dropped for the rest of this section, since it is the only possible choice. The time-evolution operator has the form (see Appendix E for derivation)

$$\langle U(t)\rangle = \left\langle \mathcal{T}\Big[\exp\Big(-i\int_0^t dt_1 \tilde{V}(t_1)\Big)\Big]\right\rangle, \tag{2.3.18}$$

where $\mathcal{T}$ denotes the time ordering operator and $\langle ...\rangle$ denotes the expectation value taken over all phonon states, dropping the subscript ph. The tilde denotes the interaction representation of V (see Appendix A.3 for details on the interaction representation), which is given by

$$\tilde{V}(t) = e^{iH_{\mathrm{ph}}t}Ve^{-iH_{\mathrm{ph}}t} = \sum_{\mathbf{q}} \lambda^*_{\mathbf{q}} b_{\mathbf{q}} e^{-i\omega_q t} + \lambda_{\mathbf{q}} b^\dagger_{-\mathbf{q}} e^{i\omega_q t}, \tag{2.3.19}$$

where the Baker-Hausdorff lemma has been used (see Appendix D) to find the explicit time dependence and noting also that $\lambda_q = \lambda^*_{-q}$. Then, by using linked cluster expansion [37, 46, 54], Eq. (2.3.18) can be expressed compactly in terms of the cumulant $K(t)$,

$$\langle U(t)\rangle = \left\langle \mathcal{T}\Big[\exp\Big(-i\int_0^t dt_1 \tilde{V}(t_1)\Big)\Big]\right\rangle = e^{K(t)}, \tag{2.3.20}$$

where the cumulant is given by

$$K(t) = -\frac{1}{2}\int_0^t dt_1 \int_0^t dt_2 \langle \mathcal{T}\tilde{V}(t_1)\tilde{V}(t_2)\rangle, \tag{2.3.21}$$

as detailed in Appendix F. Eq. (2.3.20) can be substituted into the linear polarisation, Eq. (2.3.17), giving

$$\mathrm{P}(t) = e^{-i\omega_X t} e^{K(t)}. \tag{2.3.22}$$

This approach is particularly powerful, as it allows for an elegant and exact resummation of contributions from all orders of the perturbation generated from expanding the time evolution operator. This is possible due to the system-bath interaction, given by Eq. (2.3.11), which is linear in the phonon operators and diagonal in the exciton operators. This linearity allows for the use of Wick's theorem to reduce all higher-order phonon correlations to second-order correlations. Unlike models with non-linear system-bath couplings (which require truncation or approximations), the IB model allows the exact form of $K(t)$ to be computed, and thus, the polarisation is known exactly. However, the IB model does not capture ZPL broadening due to the linear coupling, for example, in Ref.37 the quadratic coupling to phonons leads to ZPL broadening. Also, in Ref.[56], using one-dimensional (1D) phonons, the same coupling leads to a finite ZPL width due to the specifics of the phonon spectral density.

The expectation value in the cumulant $K(t)$, where $\tilde{V}(t)$ is defined in Eq.(2.3.19), is evaluated in Appendix G as

$$K(t) = \sum_{\mathbf{q}} |\lambda_{\mathbf{q}}|^2 \left(\frac{N(\omega_q)}{\omega_q^2} [e^{i\omega_q t} - 1] + \frac{N(\omega_q) + 1}{\omega_q^2} [e^{-i\omega_q t} - 1] + \frac{it}{\omega_q} \right), \tag{2.3.23}$$

where $N(\omega)$ is the Bose-distribution function, given by

$$N(\omega) = 1/\left[e^{\beta\omega} - 1\right], \tag{2.3.24}$$

for phonons of energy ω, and noting that it is also a function of the temperature, contained within β. The summation over $\mathbf{q}$ can be converted to an integration in the following way,

$$\sum_{\mathbf{q}} \rightarrow \frac{\Omega}{(2\pi)^3} \int d^3\mathbf{q} = \frac{\Omega}{(2\pi)^3} \int_0^\infty q^2 dq \int_0^\pi sin\theta d\theta \int_0^{2\pi} d\phi, \tag{2.3.25}$$

then, integrating over angles gives

$$\sum_{\mathbf{q}} \to \frac{\Omega}{(2\pi)^3} \cdot 4\pi \int_0^\infty q^2 dq = \frac{\Omega}{2\pi^2} \int_0^\infty q^2 dq. \tag{2.3.26}$$

Now, using the linear dispersion relation $\omega = v_s q$ (where $q = |\mathbf{q}|$), so $q = \omega/v_s$ and $dq = d\omega/v_s$, we find

$$\sum_{\mathbf{q}} \to \frac{\Omega}{2\pi^2 v_s^3} \int_0^\infty \omega^2 d\omega, \tag{2.3.27}$$

Note also that $|\lambda_{\mathbf{q}}|^2$ can be expressed in terms of the spectral density $J(\omega) = \sum_{\mathbf{q}} |\lambda_{\mathbf{q}}|^2 \delta(\omega - \omega_q)$. The spectral density describes the strength of the exciton-phonon coupling as a function of the phonon frequency ω, weighted by the density of phonon states at that frequency, and is given explicitly by

$$J(\omega) = \frac{\omega^3 (D_c - D_v)^2}{4\pi^2 \rho_m v_s^5} e^{\frac{-\omega^2}{\omega_0^2}} \tag{2.3.28}$$

for spherical (isotropic) QDs (see Appendix H for derivation). Eq. (2.3.28) assumes a factorisable form of the exciton wave function, $\Psi_X(\mathbf{r}_e, \mathbf{r}_h) = \psi_e(\mathbf{r}_e)\psi_h(\mathbf{r}_h)$, where $\psi_{e(h)}(\mathbf{r})$ is the confined electron (hole) ground state wave function. Also chosen is spherically symmetric parabolic confinement potentials which give Gaussian wave functions. This Gaussian form results in the Gaussian factor in the spectral density, and thus ω_0 is inversely proportional to the Gaussian length. Where ω_0 is related to the time scale of the phonon system, given by

$$\omega_0 = \frac{\sqrt{2} v_s}{l}. \tag{2.3.29}$$

l is the electron/hole confinement length, taken to be equal for simplicity. In short, some assumptions made in deriving the spectral density are, (i) the phonon parameters in the QD are not significantly different from those in the surrounding material, (ii) the acoustic phonons follow a linear dispersion of $\omega_q = v_s|q|$, and (iii) there is a spherically symmetric parabolic confinement potential resulting in Gaussian wave functions. Using the spectral density, is possible to rewrite

Eq.(2.3.23) as

$$K(t) = \int_0^\infty d\omega\, J(\omega) \left(\frac{N(\omega)}{\omega^2}[e^{i\omega t} - 1] + \frac{N(\omega)+1}{\omega^2}[e^{-i\omega t} - 1] + \frac{it}{\omega} \right). \tag{2.3.30}$$

In the long-time limit, Eq.(2.3.30) simplifies to

$$K_\infty(t) = -i\Omega_\mathrm{p} t - S, \tag{2.3.31}$$

where Ω_p is the polaron shift, and is defined as

$$\Omega_\mathrm{p} = -\int_0^\infty d\omega \frac{J(\omega)}{\omega}. \tag{2.3.32}$$

Physically, the polaron shift represents a renormalization of the excitonic energy level due to the formation of a phonon cloud surrounding the quantum dot, which arises from the exciton–phonon interaction. This shift reflects the reorganisation of the lattice upon exciton creation, effectively dressing the exciton and forming a quasiparticle known as a polaron. The polaron shift is a temperature-independent effect. The next term in Eq. (2.3.31), S, is an effective Huang–Rhys factor which depends on the temperature and quantifies the coupling strength between the exciton and the phonon bath. The Huang–Rhys factor, in the context of a single vibrational mode, is given by $S_\mathrm{HR} = \frac{|\lambda_q|^2}{\omega_q^2}$. It is a dimensionless measure of the strength of the electron-phonon coupling. It quantifies the number of phonons emitted during a transition and the associated reorganisation energy. For a continuum of phonon modes, the Huang–Rhys factor generalises to the integral form

$$S_\mathrm{HR} = \int_0^\infty d\omega\, \frac{J(\omega)}{\omega^2}, \tag{2.3.33}$$

which determines the ZPL weight e^{-S} at zero temperature. In the IB model at finite temperature, the relevant quantity controlling the long-time value of the polarisation incorporates the phonon populations, yielding

$$S = \int_0^\infty d\omega \frac{J(\omega)}{\omega^2}(2N(\omega) + 1). \tag{2.3.34}$$

This temperature-dependent generalisation can be regarded as an effective Huang–Rhys factor, since it plays the same role in renormalising the ZPL but also incorporates thermal fluctuations in addition to zero-point contributions.

Using Eqs.(2.3.30)-(2.3.32) and Eq. (2.3.34), the cumulant $K(t)$ can be separated into the long-time asymptotic behaviour $K_\infty(t)$, which forms the ZPL in frequency space and a rapid initial decay $K_{\mathrm{BB}}(t)$ which results in the phonon broadband in frequency space, given by

$$K_{\mathrm{BB}}(t) = \int_0^\infty d\omega \frac{J(\omega)}{\omega^2}\Big(N(\omega)e^{i\omega t} + [N(\omega)+1]e^{-i\omega t}\Big). \tag{2.3.35}$$

Thus, the full cumulant is a sum of the two,

$$K(t) = K_{\mathrm{BB}}(t) + K_\infty(t). \tag{2.3.36}$$

The polarisation, given in Eq.(2.3.22), is then re-expressed as

$$\mathrm{P}(t) = e^{-i\omega_X t} e^{K_\infty(t)} e^{K_{\mathrm{BB}}(t)} \tag{2.3.37}$$

The Huang-Rhys factor S and the broadband contribution $K_{\mathrm{BB}}(t)$ must be numerically integrated, allowing for the polarisation Eq.(2.3.37) to be calculated.

Throughout this thesis, the properties of InGaAs QDs are used [37, 46], which are listed in Table 2.1. The rest of the parameters, such as confinement lengths, phonon bath temperature and coupling strengths, will be provided in the figure captions.

Table 2.1: Physical parameters of QD material (InGaAs)

Parameter	Value	Units
Deformation potential difference $(D_c - D_v)$	-6.5	eV
Mass density (ρ_m)	5.65	g/cm^3
Speed of sound(v_s)	4.6	km s^{-1}

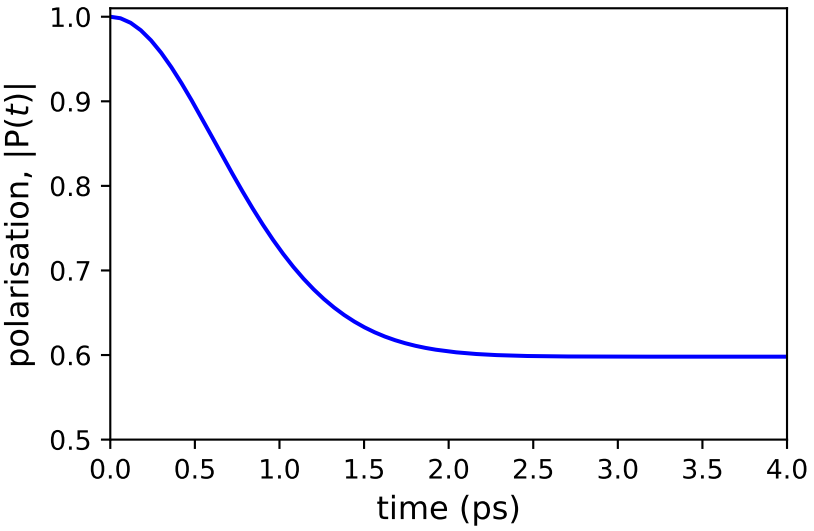

Figure 2.4: The absolute value of the independent boson model linear polarisation $|\mathrm{P}(t)|$ for $T = 50\,\mathrm{K}$ according to Eq.(2.3.37). The calculation was performed using the QD parameters in Table 2.1 and using an isotropic QD model with Gaussian confinement length $l = 3.3\,\mathrm{nm}$.

Fig. 2.4 shows the absolute value of the linear optical polarisation in the IB model for $T = 50\,\mathrm{K}$ and isotropic QDs with confinement length $l = 3.3\,\mathrm{nm}$. No phenomenological damping was used, i.e. $\gamma_X = 0$, so that the exciton energy ω_X is real. There is a rapid initial decay due to $K_{\mathrm{BB}}(t)$, where it is observed that the initial decay occurs within roughly $2\,\mathrm{ps}$ at $T = 50\,\mathrm{K}$.

The cumulant in the IB model, Eq. (2.3.36), describes the effects of the phonon bath on the system, and has been separated into different frequency components of the bath (leading to early and long time effects). The broadband component $K_{\mathrm{BB}}(t)$ is mostly referring to the contribution from high-energy phonon modes, reflecting the rapid adjustment of high-frequency phonons to the new exciton state at $t = 0$, following the pulsed excitation of the QD. These high-frequency modes quickly interact with the system at early times, causing a rapid non-Markovian decay in the polarisation i.e. quickly disturbing the coherence between the excitonic state and ground state. This initial decay arises because the phonons induce memory effects over short timescales, known as the memory time, during which the system retains information about its earlier states rather than "forgetting" them immediately, as in Markovian evolution.

Once the polaron is formed, the phonon bath stabilises because the phonons couple only diagonally to the system, meaning they shift the energy of the excited state without inducing transitions. Consequently, after the initial decay, the polarisation stabilises to a reduced but constant value, proportional to e^{-S} (the ZPL weight), with no further reduction at long times in the IB model. To introduce long-time ZPL broadening, one would need some off-diagonal coupling to induce transitions between system states which is not present in the IB model, or introduce higher-order phonon-phonon interactions, e.g. cubic interactions in [38].

It is intuitive that temperature plays an important role, since K_{BB} depends on the phonon populations, determined via $N(\omega)$, which increases with increasing temperature. The increasing temperature means that more phonon modes are thermally populated, increasing the effective coupling strength to phonons and speeding up the initial loss of coherence. The broadband contribution can be found by taking the full linear polarisation Eq. (2.3.37) and subtracting the asymptotic behaviour $\mathrm{P}_\infty(t)$, $\mathrm{P}_{\mathrm{BB}}(t) = \mathrm{P}(t) - \mathrm{P}_\infty(t)$, leaving only the early-time broadband contribution. Fig. 2.5 shows the broadband contribution to the linear polarisation

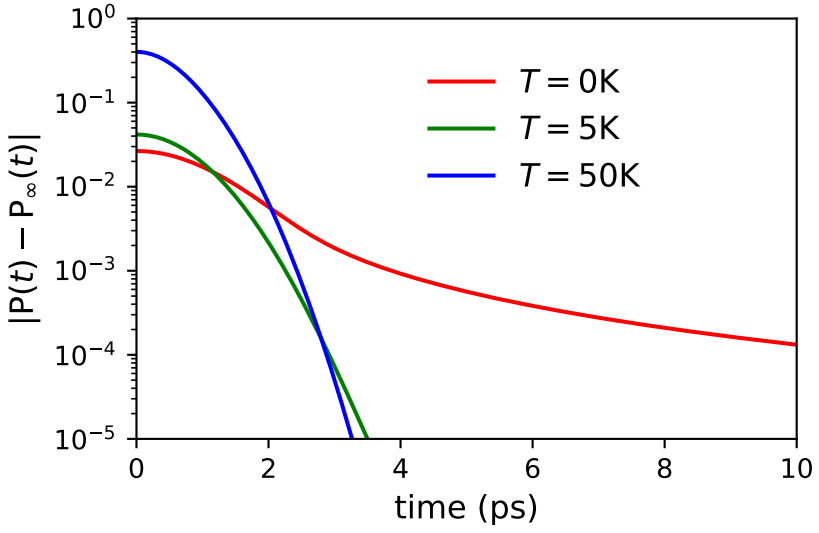

Figure 2.5: The absolute value of the broadband contribution to the independent boson model linear polarisation $|\mathrm{P}(t) - \mathrm{P}_\infty(t)|$ for $T = 0$, 5, 50 K. The calculation was performed using the QD parameters in Table 2.1 and using an isotropic QD with confinement length $l = 3.3\,\mathrm{nm}$

for three temperatures, $T = 0$, 5 and 50 K. At $T = 0$,K, the phonon bath is in the

ground state with no thermally active phonons. When the exciton is first created, the lattice is immediately pushed out of its equilibrium position, creating lattice vibrations (polaron formation). The excitonic state becomes entangled with the phonons created by the excitation causing the loss of coherence. In the finite temperature case, the phonon bath is already thermally populated and introduces further decoherence. The exciton-induced lattice displacement interacts with these active modes, producing additional phase fluctuations in the exciton's coherence during the initial polaron formation. This accelerates the early-time dephasing relative to the $T = 0\,\mathrm{K}$ case.

2.3.1 Phonon memory time

It is useful to define the characteristic timescale associated with this system τ_{IB}, defined as

$$\tau_{\mathrm{IB}} \approx \frac{2\pi}{\omega_0} = \frac{\sqrt{2}\pi l}{v_s}, \tag{2.3.38}$$

where ω_0 is given in Eq. (2.3.29). This quantity provides an approximate timescale for the phonon memory time. Physically, τ_{IB} corresponds to the time required for lattice atoms to return to their equilibrium positions once the exciton has recombined (or similarly, the formation time of the phonon cloud following exciton creation). For the system parameters used in this section, τ_{IB} is approximately 3.2 ps, and as shown in Fig. 2.5, this approximation is reasonable for temperatures exceeding 5 K. A more precise characterisation of the phonon memory time could be obtained by identifying the time at which the K_{BB} term decays below a given threshold, such as 10^{-3}. This approach more closely aligns with how memory times (or correlation times) are defined in non-Markovian methods.

At this point the absorption spectra can be considered, which is obtained by taking the real component of the FT of the linear polarisation, given in Eq. (2.3.37). Taking the FT of the initial rapid decay would result in spectrally broad absorption features, giving the phonon broadband. However, the ZPL does not have a finite linewidth in the IB model, therefore, one can add a phenomenological damping γ_X, resulting in complex exciton energy $\omega_{\mathrm{X}} = \Omega_X - i\gamma_X$. The result is that an artificial

ZPL linewidth is introduced in the absorption spectra, though not intrinsic to the IB model.

It is possible to find the ZPL by neglecting the broadband contribution from $K_{\mathrm{BB}}(t)$ in Eq. (2.3.37), allowing an analytical solution,

$$\mathrm{A}_{\mathrm{ZPL}}(\omega) = \frac{e^{-S}\gamma_X}{(\omega - \bar{\Omega}_X)^2 + \gamma_X^2}, \tag{2.3.39}$$

where the complex frequency ω_X has been separated into real (Ω_X) and imaginary (γ_X) components, and defining $\bar{\Omega}_X = \Omega_X + \Omega_{\mathrm{p}}$. Thus, $\bar{\Omega}_X$ has the meaning of the ZPL position in frequency space shifted by Ω_{p} from the bare exciton energy Ω_X, hence the name polaron shift. Eq. (2.3.39) is simply a Lorentzian broadened line centred on the real energy $\bar{\Omega}_{\mathrm{X}}$. By neglecting the phonon contributions entirely, the absorption spectra of the ZPL is given by

$$\mathrm{A}(\omega) = \frac{\gamma_X}{(\omega - \Omega_X)^2 + \gamma_X^2}. \tag{2.3.40}$$

By comparing Eq. (2.3.39) with Eq. (2.3.40), it can be seen that the effects of phonon interaction with the exicton are to (i) suppress the ZPL weight by a factor of e^{-S}, (ii) displace the ZPL from the bare exciton energy by the polaron shift Ω_{p}. There are further effects associated with the $e^{K_{\mathrm{BB}}}$ term we neglected in the absorption spectra. The long-time asymptotic behaviour of Eq.(2.3.37) can be subtracted from the full expression, as performed in Fig. 2.5, leaving only the rapid initial decay of the polarisation. Then numerically taking the real part of its FT, the phonon broadband can be found, which is then added to the analytic ZPL result from Eq.(2.3.39) to produce the full absorption spectra of the IB model.

Fig. 2.6 shows the absorption spectra of the independent boson (IB) model at $T = 5, \mathrm{K}$ (left) and $T = 50, \mathrm{K}$ (right). The central peak corresponds to the zero-phonon line (ZPL), as described by Eq. (2.3.39). It represents the direct optical transition between the ground state and the first excited exciton state, shifted by the polaron shift due to exciton–phonon coupling. The influence of phonons is evident even at

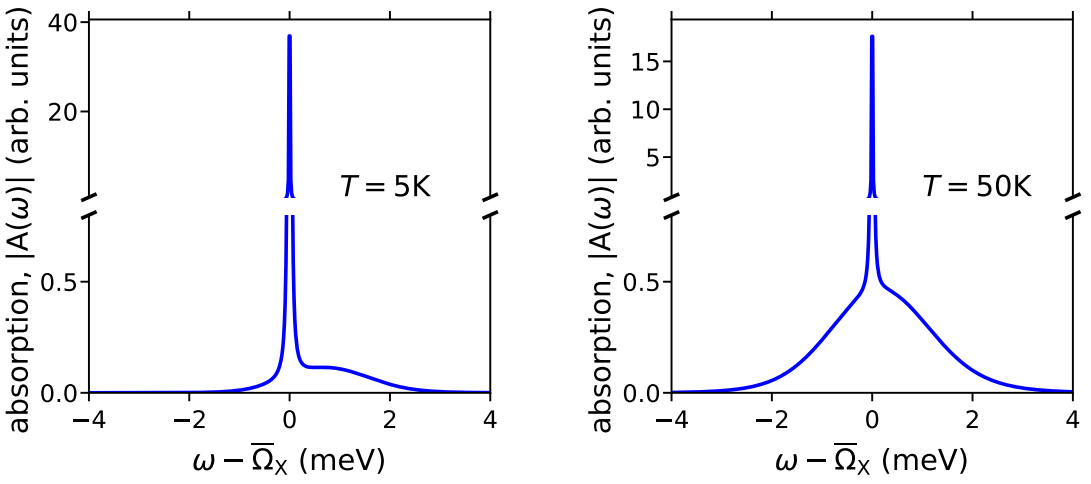

Figure 2.6: Left: Absorption spectra $A(\omega)$ for $T = 5$ K. Right: Absorption spectra for $T = 50\,\mathrm{K}$. The calculation was performed using the QD parameters in Table 2.1 and using an isotropic QD with confinement length $l = 3.3\,\mathrm{nm}$.

$T = 5\,\mathrm{K}$, where it is clear that absorption occurs at frequencies above the ZPL. This corresponds to phonon emission processes, i.e. the exciton absorbs a photon of higher energy than the bare transition energy, and the excess energy is released by emitting one or more phonons. At $T = 50\,\mathrm{K}$ (right), the spectrum becomes more symmetric. This is due to an increased phonon population at higher temperatures, enabling phonon absorption processes, i.e. photons with less energy than the bare exciton transition can still excite the system if the missing energy is provided by absorbing phonons from the environment. These features reflect phonon-assisted transitions, where the exciton can absorb light at off-resonant energies due to energy exchange with the phonon bath. As a result, the absorption spectrum broadens and develops sidebands around the ZPL, with the shape becoming more symmetric at higher temperatures due to the balance between phonon emission and absorption.

2.4 Summary

In this chapter, we used the JC model to investigate the linear polarisation and absorption spectra in a QD-cavity system. We saw that in the strong-coupling regime, the coherent exchange of energy between the QD and cavity results in the

formation of a polariton with an upper and lower branch. The energy splitting between the branches is known as the Rabi splitting, determined via the exciton-cavity coupling strength. The transfer of energy between these branches results in Rabi oscillations seen in the quantum dynamics. Then, the QD exciton-phonon interactions described by the IB model were studied. This introduced techniques on how to incorporate the influence of phonons on the system. Also, the effect that phonons have on the coherences was observed, in particular the non-Markovian dynamics which is characterised by the rapid initial decay in the linear polarisation. This rapid initial decay is a fingerprint of the polaron formation. We also saw that the IB model, which only has diagonal QD-phonon coupling, does not introduce any long-time decay of the linear polarisation. Importantly, both the JC and IB models have exact solutions, but the combination of these techniques presents a challenge. The IB model allowed us to understand the loss of coherence in a single QD system coupled to a phonon bath, but more complex architectures, such as quantum logic gates, require coupling between multiple QDs. When two QDs are directly coupled, their states hybridise, and the system behaves as a single, extended quantum emitter. In this regime, maintaining coherence between the hybridised states becomes essential, for example in the implementation of two-qubit gates [8, 9]. In the following chapter, an approach is developed to extend beyond the IB model, allowing us to study multi-qubit systems and decoherence. Through this, a method to preserve coherence in these coupled qubit systems is described and illustrated.

Chapter 3

Path-Integral based approach: Combining the JC and IB models

3.1 Introduction

The decoherence and phenomena such as energy relaxation dynamics of open quantum systems is characterised by the interaction between the system and its surrounding environment (bath). In the simplest case, the system-environment coupling is weak and it can be assumed that the environment lacks memory, i.e. Markovian, and remains uncorrelated with the system. This assumption allows the use of Born and Markov approximations [55, 57, 58] resulting in a time-local equation of motion. This is valid because the environments effect on the system occurs on a much larger timescale than the correlation time of the environment. However, many quantum systems deviate from this idealised case, and memory effects play a critical role and render the Born-Markov approximation invalid. In such non-Markovian regimes, the system's evolution depends on its past interactions, leading to complex phenomena [13, 18, 22, 30]. Accurately capturing these non-Markovian effects is essential but comes with significant computational challenges, often limiting the scope of treatable systems and coupling regimes.

The typical approaches to solving the dynamics in non-Markovian open quantum systems can broadly be divided into perturbative and non-perturbative methods. With perturbative treatments typically being limited to specific parameter regimes, e.g. strong QD-cavity coupling and weak electron-phonon interactions [17]. Or, via the polaron transformation combined with a perturbation theory [24, 59]. However, for stronger exciton-phonon coupling, phonons play a more significant role that requires non-perturbative techniques [60].

In particular, Feynman's path integral formulation is a non-perturbative technique which is very well suited for system-bath dynamics as it avoids dealing with the large Hilbert space of the bath by targeting the system's reduced density matrix (RDM). The formulation takes into account the effects of a harmonic bath on the system dynamics through the well known Feynman-Vernon influence functional [61], valid for any system-bath coupling strength. In practice, the issue is that the influence functional is nonlocal in time, meaning that the coordinates of a path at any particular time point are connected to coordinates at all other time points, leading to full entanglement. This is discussed in more detail in Chapter 5. As a consequence, as the number of correlations grows with each time step, there is an exponential scaling with propagation time, restricting the dynamics to only short times. However, as there is a finite length to the nolocal interactions contained in the influence functional, known as the memory time. An example of this memory time was observed in the previous section, where the phonon memory time was τ_{IB} in the IB model. This finite memory time led to the development of the iterative quasi-adiabatic propagator path integral (i-QuAPI) approach [62–67], resulting in a linear scaling with the number of propagations (time steps). This linear scaling is due to the fact that the influence functional is not growing in size as time progresses and is of a fixed size, i.e. fixed number of correlations. To clarify, the number of correlations within the memory time depends on how small the time step is. If there is a small time step, there will be more steps within the memory time, and thus, more correlations. The i-QuAPI approach is a tensor-multiplication scheme based on the combined use of Trotter's decomposition and

the Feynman-Vernon influence functional. Due to the finite memory time, it can be used to evaluate the dynamics of the reduced density matrix for an arbitrary time length, not limited to short times. The amount of correlations (and thus the number of time steps) contained within the influence functional determines the accuracy of the calculation, however, the computational cost grows exponentially with the number of correlations. The memory storage requirements can quickly become too large and in some systems convergence is not achievable. To address this, filtering techniques [68–70], modified truncation schemes [71], path segment merging (MACGIC-iQuAPI) [72], and in some regimes blip decomposition [73, 74] have been developed to offer improvements to the storage requirements or extend the applicability to longer memory times. However, there is still great difficulty in accurately modelling systems where memory effects from the environment are significant, such as energy transfer processes with long coherence times (e.g., photosynthetic complexes) or multi-qubit decoherence in structured environments [45, 75].

More recently, the development of approaches utilising modern tensor network (TN) techniques have provided exceptional reductions in memory requirements, such as the Time-Evolving Matrix Product Operator (TEMPO) algorithm [32] (more recently packaged as OQuPY [76]). Or the ACE algorithm [77], another TN approach which further reduces requirements by concentrating only on the most relevant degrees of freedom of the bath. An enhanced TEMPO algorithm has also been developed to include an off-diagonal system bath coupling to the Hamiltonian, leading to multi-time correlations [78].

Another path-integral based, numerically exact tensor multiplication scheme is the Trotter decomposition with linked cluster expansion technique [43], developed in parallel with the techniques mentioned. This technique has been used in several cases, such as the four-wave mixing (FWM) polarisation in QD-cavity systems [44], the linear polarisation in multi-qubit systems [45], and the population dynamics in Förster coupled QDs [79]. However, being a tensor multiplication scheme, it also

suffers from the exponential scaling with number of correlations included in the finite memory time. An optimisation scheme to reduce the storage requirements is developed in the Chapter 5.

In this chapter, the Trotter decomposition with linked cluster expansion technique is described for a pair of spatially separated two-level systems (TLSs) inside a microcavity and interacting with a common environment. The spatial separation combined with the common environment introduces non-trivial modifications to the technique described in [43].

3.2 System, excitation and the linear polarisation

As an example, we consider the decoherence of electronically decoupled qubits separated by a distance d and interacting with a shared bath. The coupling of the qubits is taken as either direct through Förster-like coupling [75, 80–82], or indirectly via cavity-mediation [83–85]. As a qubit and bath realisation, we use semiconductor QDs interacting with a bath of 3D acoustic phonons, widely studied in the literature [13, 33, 37, 42, 46]. The system Hamiltonian can be written as a

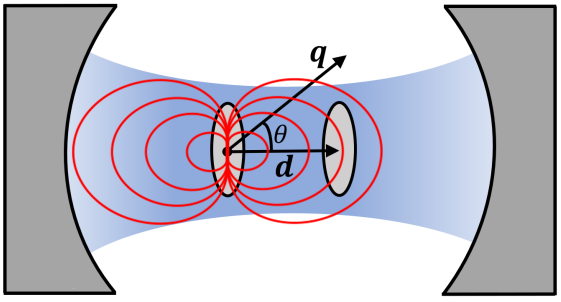

Figure 3.1: Schematic of the system with a pair of dipole-coupled qubits separated by a distance vector **d**, coupled to an optical cavity, and interacting with three-dimensional acoustic phonons described by a wave vector **q** and angle θ.

sum of two exactly solvable parts,

$$H = H_0 + H_{\mathrm{IB}}\,, \tag{3.2.1}$$

where H_0 describes the coupling between the qubits and the cavity, and H_{IB} is a generalised IB model Hamiltonian describing the coupling of the qubits to the shared environment. For the system of two remote QDs coupled to each other and to an optical cavity (as illustrated in Fig. 3.1), H_0 takes the form (using $\hbar = 1$)

$$\begin{aligned} H_0 = \Omega_1 d_1^\dagger d_1 + \Omega_2 d_2^\dagger d_2 + \Omega_C a^\dagger a + g(d_1^\dagger d_2 + d_2^\dagger d_1) \\ + g_1(d_1^\dagger a + a^\dagger d_1) + g_2(d_2^\dagger a + a^\dagger d_2)\,, \end{aligned} \tag{3.2.2}$$

where $d_j^\dagger$ is the fermionic exciton creation operator in QD j ($j = 1, 2$), $a^\dagger$ is the cavity photon creation operator, Ω_j (Ω_C) is the exciton (cavity photon) frequency, and g and g_j are the coupling strengths between the QD excitons, and the exciton in QD j and the cavity photon, respectively. The IB model Hamiltonian describes the interaction of the QD excitons with a shared acoustic-phonon bath,

$$H_{\mathrm{IB}} = H_{\mathrm{ph}} + d_1^\dagger d_1 V_1 + d_2^\dagger d_2 V_2\,, \tag{3.2.3}$$

where

$$H_{\mathrm{ph}} = \sum_{\mathbf{q}} \omega_q b_{\mathbf{q}}^\dagger b_{\mathbf{q}} \quad \text{and} \quad V_j = \sum_{\mathbf{q}} \lambda_{\mathbf{q},j}(b_{\mathbf{q}} + b_{-\mathbf{q}}^\dagger) \tag{3.2.4}$$

are, respectively, the free phonon bath Hamiltonian and the QD coupling to the bath, and $b_{\mathbf{q}}^\dagger$ is the bosonic creation operator of a bulk phonon mode with the momentum $\mathbf{q}$ and frequency ω_q (denoting $q = |\mathbf{q}|$). The coupling of the exciton in QD j to the phonon mode $\mathbf{q}$ is given by the matrix element $\lambda_{\mathbf{q},j}$, which depends on the material parameters, exciton wave function, and position of the QD. Their explicit form for isotropic and anisotropic QDs is provided in Appendix H. For identical QD qubits separated by a distance vector $\mathbf{d}$, the matrix elements satisfy the relation

$$\lambda_{\mathbf{q},2} = e^{i\mathbf{q}\cdot\mathbf{d}} \lambda_{\mathbf{q},1}\,. \tag{3.2.5}$$

In the following, we focus on the linear polarisation, allowing us to study the coherence of the system as a function of the distance between the qubits. The linear polarisation of qubit j is defined as $\mathrm{P}_{jk}(t) = \mathrm{Tr}\{\rho(t) d_j\}$, where $\rho(t)$ is the full density matrix, as discussed in Chapter 2. We assume that starting from the

system ground state the qubit with index k is instantaneously excited at time $t = 0$. As has been derived in Appendix B.1, the linear polarisation can be written as

$$\mathrm{P}_{jk}(t) = \langle\langle j| U(t) |k\rangle\rangle_{\mathrm{ph}} , \tag{3.2.6}$$

where $U(t) = e^{iH_{\mathrm{ph}}t}e^{-iHt}$ is the evolution operator and $\langle ...\rangle_{\mathrm{ph}}$ denotes the expectation value over all phonon degrees of freedom in thermal equilibrium. Here and below we use the following basis states

$$|j\rangle = d_j^\dagger |0\rangle \quad \text{and} \quad |C\rangle = a^\dagger |0\rangle , \tag{3.2.7}$$

where $|0\rangle$ represents the vacuum state of the QD-cavity subsystem, and $j = 1, 2$.

Taking advantage of the two exactly solvable parts of the Hamiltonian, given in Eq. (3.2.1), we apply the method of Trotter's decomposition with linked cluster expansion [43], summarised in the following section, that allows us to take into account the effect of the phonon environment *exactly*.

3.3 Trotter's decomposition with linked cluster expansion

The method of Trotter's decomposition with linked cluster expansion was developed in [43], providing an exact calculation of the linear polarisation of a single QD simultaneously coupled to a cavity and a phonon bath. Here, it is further developed and applied to the more general case of cavity-mediated coupling between the QDs (with the coupling constants g_1 and g_2) and their direct dipolar coupling (with the coupling constant g), as described by Eq. (3.2.2). It is worth noting that linked cluster expansion is also commonly called cumulant expansion in some other works.

3.3.1 Trotter's decomposition

We commence by splitting the time interval $[0, t]$, where t is the observation time, into N equal steps of duration $\Delta t = t/N = t_n - t_{n-1}$, where the time $t_n = n\Delta t$ represents the time after the n-th step. Trotter's theorem is then used to separate the time evolution of the two non-commuting operators, H_0 and H_{IB}. For sufficiently small Δt, we can assume independent evolution of the two exactly solvable components within each time step. In fact, applying Trotter's decomposition theorem, the time evolution operator $U(t)$ can be written as

$$U(t) = \lim_{N\to\infty} e^{iH_{\mathrm{ph}}t}(e^{-iH_{\mathrm{IB}}t/N}e^{-iH_0 t/N})^N . \tag{3.3.1}$$

Eq.(3.3.1) can be further expressed as $U(t) = \lim_{N\to\infty} U_N(t)$, with

$$\begin{aligned} U_N(t) = {} & e^{iH_{\mathrm{ph}}t}e^{iH_{IB}(t-t_{N-1})}e^{-iH_{\mathrm{ph}}t_{N-1}}e^{-iH_0(t-t_{N-1})} \\ & \times e^{iH_{\mathrm{ph}}t_{N-1}}e^{iH_{IB}(t_{N-1}-t_{N-2})}e^{-iH_{\mathrm{ph}}t_{N-2}}e^{-iH_0(t_{N-1}-t_{N-2})}... \\ & \times e^{iH_{\mathrm{ph}}t_n}e^{iH_{IB}(t_n-t_{n-1})}e^{-iH_{\mathrm{ph}}t_{n-1}}e^{-iH_0(t_n-t_{n-1})}... \\ & \times e^{iH_{\mathrm{ph}}t_1}e^{iH_{IB}t_1}e^{-iH_0 t_1}. \end{aligned} \tag{3.3.2}$$

Eq.(3.3.2) can be written in this way because H_{ph} and H_0 commute, therefore we are able to introduce $e^{-iH_{\mathrm{ph}}t_{n-1}}$ and $e^{iH_{\mathrm{ph}}t_{n-1}}$ on either side of each $e^{-iH_0(t_n-t_{n-1})}$ term. We now introduce two matrices to compactly represent Eq.(3.3.2), $\hat{M}$ and $\hat{W}$, which describe the dynamics due to H_0 and H_{IB}, respectively, each being analytically solvable. Using these operators, the QD-QD and QD-cavity dynamics over a single time step, without phonons, is described by

$$\hat{M}(t_n - t_{n-1}) = \hat{M}(\Delta t) = e^{-iH_0\Delta t} \tag{3.3.3}$$

and the exciton-phonon dynamics is given by

$$\hat{W}(t_n, t_{n-1}) = e^{iH_{\mathrm{ph}}t_n}e^{-iH_{\mathrm{IB}}\Delta t}e^{-iH_{\mathrm{ph}}t_{n-1}} . \tag{3.3.4}$$

Then, one can write the time evolution operator Eq. (3.3.1) as

$$U(t) = \mathcal{T} \prod_{n=1}^{N} \hat{W}(t_n, t_{n-1}) \hat{M}(t_n - t_{n-1}) \,, \tag{3.3.5}$$

where $\mathcal{T}$ is the time-ordering operator. $\hat{W}$ and $\hat{M}$ are both 3×3 matrices in the $|1\rangle$, $|2\rangle$, $|C\rangle$ basis, and due to the diagonal form of the exciton-phonon interaction, $\hat{W}$ is diagonal. Its diagonal matrix elements can be written as

$$W_{i_n}(t_n, t_{n-1}) = \mathcal{T} \exp\left\{ -i \int_{t_{n-1}}^{t_n} \tilde{V}_{i_n}(\tau) d\tau \right\}, \tag{3.3.6}$$

as shown in Appendix E, with

$$\tilde{V}_{i_n}(\tau) = \xi_{i_n} \tilde{V}_1(\tau) + \eta_{i_n} \tilde{V}_2(\tau) \tag{3.3.7}$$

for τ within the time interval $t_{n-1} \leqslant \tau \leqslant t_n$. Here ξ_i and η_i are the components of the vectors

$$\vec{\xi} = \begin{pmatrix} 1 \\ 0 \\ 0 \end{pmatrix} \quad \text{and} \quad \vec{\eta} = \begin{pmatrix} 0 \\ 1 \\ 0 \end{pmatrix} , \tag{3.3.8}$$

respectively, and $\tilde{V}_j(\tau) = e^{iH_{\text{ph}}\tau} V_j e^{-iH_{\text{ph}}\tau}$ is the exciton-phonon coupling in the interaction representation, with $\tilde{V}_j$ defined in Eq. (3.2.4). The explicit time dependence of $V_j(\tau)$ is found via the Baker-Hausdorff lemma, detailed in Appendix D and results in

$$\tilde{V}_j(\tau) = \sum_{\mathbf{q}} \lambda^*_{\mathbf{q},j} b_{\mathbf{q}} e^{-i\omega_q \tau} + \lambda_{\mathbf{q},j} b^\dagger_{-\mathbf{q}} e^{i\omega_q \tau}. \tag{3.3.9}$$

We use the indices i_n to indicate which state the system is in at a given time step n, being either $|1\rangle$, $|2\rangle$, or $|C\rangle$, with i_n taking the values 1, 2, or C, respectively. The elements of the vectors $\vec{\xi}$ and $\vec{\eta}$ take care of the choice for which exciton is coupled to phonons at time step n. For example, if the system is in the first QD exciton state at time step n, then $i_n = 1$, and the exciton-phonon interaction V_1 occurs.

To find the polarisation, we use Eq. (3.3.5) to substitute $U(t)$ in Eq. (3.2.6), and write the matrix products explicitly, yielding

$$\mathrm{P}_{jk}(t) = \sum_{i_{N-1}=1,2,C} \cdots \sum_{i_1=1,2,C} M_{i_N i_{N-1}} \dots M_{i_1 i_0} \times \langle W_{i_N}(t, t_{N-1}) \dots W_{i_1}(t_1, 0) \rangle_{\mathrm{ph}} \,, \tag{3.3.10}$$

where $i_0 = k$ and $i_N = j$ denote the excitation channel k at $t = 0$ and measurement channel j at the final time step $t_N = t$, and $M_{i_n i_m} = [\hat{M}(\Delta t)]_{i_n i_m}$. The W_{i_n} operators include the phonon contributions, therefore we separate this product from the rest of the expression in order to take the expectation value and apply the linked cluster theorem [37, 46, 54].

3.3.2 Linked cluster expansion

To calculate the expectation value of the products of the exciton-phonon interaction operators in Eq. (3.3.10), we apply the linked cluster theorem. It allows us to write this expectation value as an exponential with a double sum over all possible second-order cumulants (as in the IB model) in the exponent [43, 44, 54],

$$\langle W_{i_N}(t, t_{N-1}) \dots W_{i_1}(t_1, 0) \rangle_{\mathrm{ph}} = \exp\left(\sum_{n=1}^{N} \sum_{m=1}^{N} \mathcal{K}_{i_n i_m}(|n-m|) \right) \tag{3.3.11}$$

Each cumulant in Eq. (3.3.11) is given by

$$\mathcal{K}_{i_n i_m}(s) = -\frac{1}{2} \int_{t_{n-1}}^{t_n} d\tau_1 \int_{t_{m-1}}^{t_m} d\tau_2 \langle \mathcal{T} \tilde{V}_{i_n}(\tau_1) \tilde{V}_{i_m}(\tau_2) \rangle_{\mathrm{ph}}, \tag{3.3.12}$$

where $s = |n-m|$. Using Eq. (3.3.7), this cumulant can be expressed as (dropping the tilde notation on V_j which denotes the interaction representation for brevity)

$$\mathcal{K}_{i_n i_m}(s) = -\frac{1}{2} \int_{t_{n-1}}^{t_n} d\tau_1 \int_{t_{m-1}}^{t_m} d\tau_2 \left\langle \mathcal{T} \left[\xi_{i_n} V_1(\tau_1) + \eta_{i_n} V_2(\tau_1) \right] \left[\xi_{i_m} V_1(\tau_2) + \eta_{i_m} V_2(\tau_2) \right] \right\rangle_{\mathrm{ph}} . \tag{3.3.13}$$

Expanding the integrand yields time ordered pair products $\mathcal{T}V_j(\tau_1)V_{j'}(\tau_2)$, so it is natural to introduce phonon autocorrelation functions,

$$D_{jj'}(\tau_1-\tau_2) = \langle \mathcal{T}V_j(\tau_1)V_{j'}(\tau_2)\rangle_{\rm ph} = \sum_{\mathbf{q}} \lambda_{\mathbf{q},j}\lambda^*_{\mathbf{q},j'} \left[(N(\omega_q)+1)e^{-i\omega_q|\tau_1-\tau_2|} + N(\omega_q)e^{i\omega_q|\tau_1-\tau_2|}\right], \tag{3.3.14}$$

with $N(\omega)$ is the Bose-distribution function defined in Eq.2.3.24, and the explicit time dependence of the phonon operators, given by $b_{\mathbf{q}}(t) = b_{\mathbf{q}}e^{-i\omega_q t}$ (see Appendix D for details on the time dependence), has been used to derive Eq. (3.3.14) (see also Appendix G for more details). Introducing the phonon spectral density,

$$J_{jj'}(\omega) = \sum_{\mathbf{q}} \lambda_{\mathbf{q},j}\lambda^*_{\mathbf{q},j'}\delta(\omega-\omega_q)\,, \tag{3.3.15}$$

the phonon autocorrelation function takes the form

$$D_{jj'}(t) = \int_0^\infty d\omega\; J_{jj'}(\omega)D(\omega,t)\,, \tag{3.3.16}$$

where

$$D(\omega,t) = [N(\omega)+1]e^{-i\omega|t|} + N(\omega)e^{i\omega|t|}\,. \tag{3.3.17}$$

is the standard phonon propagator. Specific forms of the coupling matrix elements $\lambda_{\mathbf{q},j}$ and the corresponding spectral functions $J_{jj'}(\omega)$ for isotropic and anisotropic QDs are derived in Appendix H.

Now, using Eq. (3.3.14) and introducing cumulant elements

$$K_{jj'}(s) = -\frac{1}{2}\int_{t_{n-1}}^{t_n} d\tau_1 \int_{t_{m-1}}^{t_m} d\tau_2 D_{jj'}(\tau_1-\tau_2), \tag{3.3.18}$$

the cumulants Eq. (3.3.12) can be written as

$$\mathcal{K}_{i_n i_m}(s) = \xi_{i_n}\xi_{i_m}K_{11}(s) + \eta_{i_n}\eta_{i_m}K_{22}(s) + (\xi_{i_n}\eta_{i_m} + \eta_{i_n}\xi_{i_m})K_{12}(s)\,, \tag{3.3.19}$$

using $K_{21}(s) = K_{12}(s)$, due to the symmetry of the spectral function, $J_{jj'}(\omega) = J_{j'j}(\omega)$. This follows from the isotropic phonon dispersion ω_q and the

general property of the matrix elements, $\lambda_{-\mathbf{q},j} = \lambda^*_{\mathbf{q},j}$. $\mathcal{K}_{i_n i_m}$ is simply a general cumulant element which takes into account all possible cases.

A convenient way to compute the cumulant elements Eq. (3.3.18) is by defining the cumulant function

$$C_{jj'}(t) \;=\; -\frac{1}{2}\int_0^t d\tau_1 \int_0^t d\tau_2 \; D_{jj'}(\tau_1 - \tau_2)\,, \tag{3.3.20}$$

which assumes the system remains in the same states across the time evolution $[0, t]$. With this, Fig. 3.2 shows how Eq. (3.3.20) can be expressed as linear com-

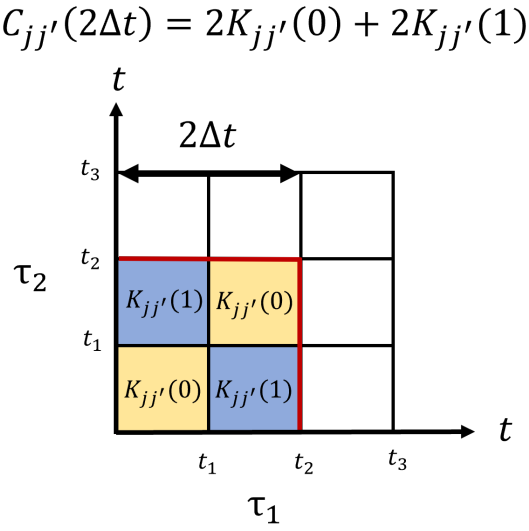

Figure 3.2: A portion of the time grid up to $t = 2\Delta t$. $C_{jj'}(2\Delta t)$ is composed of two contributions, $K_{jj'}(s = 0)$ and $K_{jj'}(s = 1)$.

binations of individual cumulant elements $K_{jj'}(s)$. Therefore, if we wish, for example, to compute $K_{11}(1)$, using Fig. 3.2 as reference, it is clear that $K_{11}(1) = \frac{1}{2}(C_{11}(2\Delta t) - 2K_{11}(0))$. Also using the fact that $K_{jj'}(s)$ depends on the difference $|n - m|$ only, and not on both time steps t_n and t_m individually every possible cumulant element across any time step can be computed. To summarise, all cumulant elements are described by the following:

$$K_{jj'}(0) = C_{jj'}(\Delta t)\,. \tag{3.3.21}$$

The remaining $s > 0$ cumulant elements are found recursively via

$$K_{jj'}(s) = \frac{1}{2}\left[C_{jj'}\big((s+1)\Delta t\big) - (s+1)K_{jj'}(0) - 2\sum_{h=1}^{s-1}(s+1-h)K_{jj'}(h)\right]. \quad (3.3.22)$$

One further note is that the cumulant elements $K_{12}(s)$ require contributions from $K_{12}(s=0)$, meaning that at time steps $n = m$, the system excitation is in both quantum dots. This is physically not the case, however is mathematically introduced for consistency.

The linear polarisation Eq. (3.3.10) then takes the final form

$$\mathrm{P}_{jk}(t) = \sum_{i_{N-1}=1,2,C} \cdots \sum_{i_1=1,2,C} M_{i_N i_{N-1}} \ldots M_{i_1 i_0} \exp\left(\sum_{n=1}^{N}\sum_{m=1}^{N} \mathcal{K}_{i_n i_m}(s)\right). \quad (3.3.23)$$

A particular realisation of the system evolution is indicated by the indices $i_{N-1}, \ldots, i_2, i_1$. However, to obtain the full quantum dynamics of the system, all possible realisations are to be summed over, meaning a summation over all of these indices, which is done in Eq. (3.3.23). This is equivalent to the idea of path-integral approach. For a finite bath memory time, it is sufficient to consider only a portion of the grid at least up to the memory time, which is referred to as the number of neighbours L, defined as the maximum value of $|n-m|$ taken into account in the calculation.

3.3.3 Nearest-neighbours (NN) approach

The simplest case is that of $L = 1$ ($s = |n-m| \leqslant 1$), which provides the most basic starting point of the more general L-neighbour approach. In this NN regime, the full cumulant summed over all time steps in Eq. (3.3.23) is approximated by only taking into account the self interaction and NN interaction as shown in Fig. 3.3. From Eqs. (3.3.8) and (3.3.19) we have in general

$$\mathcal{K}_{i_n i_m}(s) = \begin{cases} \xi_{i_n}^2 K_{11}(s) + \eta_{i_n}^2 K_{22}(s) & i_n = i_m \\ (\xi_{i_n}\eta_{i_m} + \eta_{i_n}\xi_{i_m})K_{12}(s) & i_n \neq i_m, \end{cases} \quad (3.3.24)$$

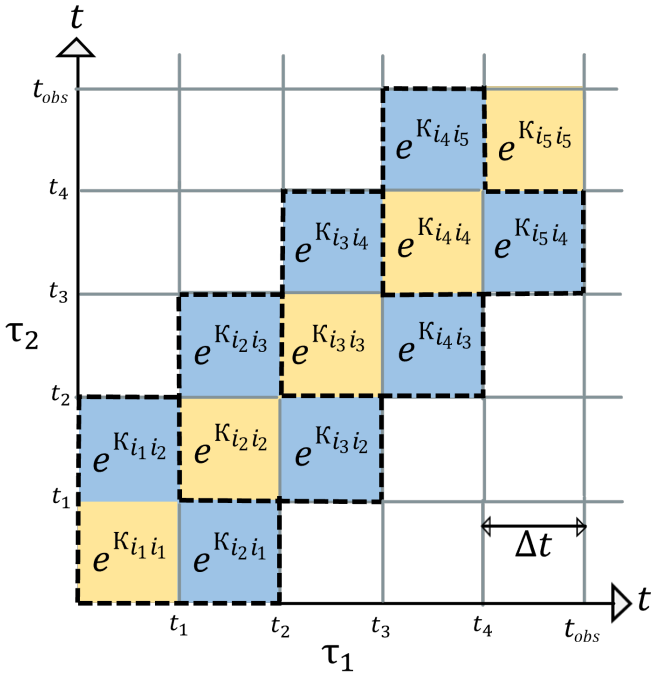

Figure 3.3: A portion of the time grid used in the nearest-neighbour approach, showing the self interaction (main diagonal, yellow squares) and NN interactions (blue squares).

and summing over all time steps while maintaining $|n-m| \leqslant 1$, the full cumulant in Eq. (3.3.23) is reduced to

$$\begin{aligned}\sum_{n=1}^{N}\sum_{m=1}^{N}\mathcal{K}_{i_n i_m}(s) \approx \sum_{n=1}^{N}&\left(\xi_{i_n}\xi_{i_n}K_{11}(0)+\eta_{i_n}\eta_{i_n}K_{22}(0)\right)\\ &+2\sum_{n=1}^{N-1}\Big[\xi_{i_{n+1}}\xi_{i_n}K_{11}(1)+\eta_{i_{n+1}}\eta_{i_n}K_{22}(1)\\ &\qquad+(\xi_{i_{n+1}}\eta_{i_n}+\eta_{i_{n+1}}\xi_{i_n})K_{12}(1)\Big]\end{aligned} \tag{3.3.25}$$

Substituting Eq. (3.3.25) back into Eq. (3.3.23), relabelling and combining the cumulant elements with the $M_{i_{n+1}i_n}$ factors, we obtain

$$\mathrm{P}_{jk}(t) = e^{\xi_j^2 K_{11}(0)+\eta_j^2 K_{22}(0)} \sum_{i_{N-1}=1,2,C} \cdots \sum_{i_1=1,2,C} G_{j\,i_{N-1}} \ldots G_{i_2 i_1} M_{i_1 k}\,, \tag{3.3.26}$$

where the matrix

$$G_{i_n i_{n-1}} = M_{i_n i_{n-1}} e^{\mathcal{K}_{i_{n-1}i_{n-1}}(0)+2\mathcal{K}_{i_n i_{n-1}}(1)}\,, \tag{3.3.27}$$

written explicitly in terms of the cumulant elements $K_{jj'}(s)$, takes the form

$$G_{i_n i_{n-1}} = M_{i_n i_{n-1}} \exp\Big\{\xi_{i_{n-1}}\xi_{i_{n-1}}K_{11}(0) + \eta_{i_{n-1}}\eta_{i_{n-1}}K_{22}(0) + 2\xi_{i_n}\xi_{i_{n-1}}K_{11}(1) + 2\eta_{i_n}\eta_{i_{n-1}}K_{22}(1) + 2(\xi_{i_n}\eta_{i_{n-1}} + \eta_{i_n}\xi_{i_{n-1}})K_{12}(1)\Big\}. \tag{3.3.28}$$

The matrix $G_{i_n i_{n-1}}$ contains products of elements which contribute to the memory kernel and generates the L-shaped regions in Fig. 3.3, highlighted by thick dashed lines. Then Eq. (3.3.26) can be compactly written in a 3×3 matrix form in the $|1\rangle$, $|2\rangle$, $|C\rangle$ basis as

$$\hat{P}(t) = \begin{pmatrix} \mathrm{P}_{11} & \mathrm{P}_{12} & \mathrm{P}_{1C} \\ \mathrm{P}_{21} & \mathrm{P}_{22} & \mathrm{P}_{2C} \\ \mathrm{P}_{C1} & \mathrm{P}_{C2} & \mathrm{P}_{CC} \end{pmatrix} = \begin{pmatrix} e^{K_{11}(0)} & 0 & 0 \\ 0 & e^{K_{22}(0)} & 0 \\ 0 & 0 & 1 \end{pmatrix} \hat{G}^{N-1}\hat{M}\,, \tag{3.3.29}$$

where $\hat{G}$ is given by

$$\hat{G} = \begin{pmatrix} M_{11}e^{K_{11}(0)+2K_{11}(1)} & M_{12}e^{K_{22}(0)+2K_{12}(1)} & M_{1C} \\ M_{21}e^{K_{11}(0)+2K_{12}(1)} & M_{22}e^{K_{22}(0)+2K_{12}(1)} & M_{2C} \\ M_{C1}e^{K_{11}(0)} & M_{C2}e^{K_{22}(0)} & M_{CC} \end{pmatrix}, \tag{3.3.30}$$

and $\hat{M}$ is defined in Eq.3.3.3. In Eq. (3.3.29), the effect of successively applying $\hat{G}$ is to propagate the system forward in time with each application. With reference to the example in Fig. 3.3, that would be generated by $N = 5$ time steps, and therefore $\hat{G}$ is applied successively 4 times to propagate the system, with the single cumulant element contribution at the end of the propagation appearing as an exponential factor outside of the summation in Eq. (3.3.26) and the diagonal matrix in Eq. (3.3.29).

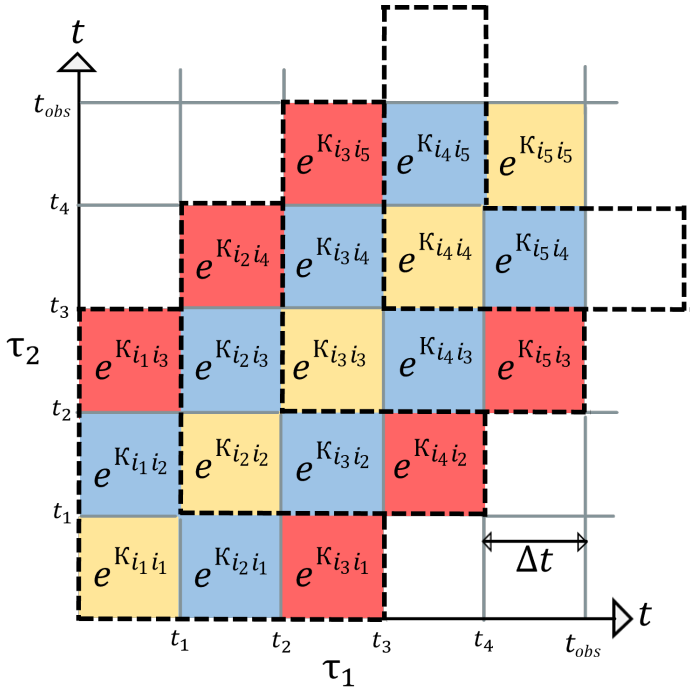

Figure 3.4: A portion of the time grid showing the cumulant elements involved in a calculation up to an observation time t_{obs} including $s = 2$ at most. This contains only the self interaction (yellow squares), the nearest (blue squares) and next-nearest neighbour interactions (red squares).

3.3.4 The L-neighbour (LN) approach

The LN approach is used to describe the temporal correlations between all considered steps within the memory kernel, rather than only the $L = 1$ case in the NN regime. The cumulant elements $K_{jj'}(s)$, with $s = |n - m|$ increasing up to its maximum value, L, are found recursively from Eq.(3.3.22).

We first define a quantity $F^{(n)}_{i_L \ldots i_1}$ which is generated via the recursive relation

$$F^{(n+1)}_{i_L \ldots i_1} = \sum_{l=1,2,C} \mathcal{G}_{i_L \ldots i_1 l} F^{(n)}_{i_{L-1} \ldots i_1 l}\,, \tag{3.3.31}$$

using $F^{(1)}_{i_L \ldots i_1} = M_{i_1 k}$ as the initial value, where k is the excitation mode and $\hat{M}$ describes the evolution without phonon interactions, given by Eq. (3.3.3). This is because after excitation in channel k at $t = 0$, one further time step introduces index i_1, and beyond this the phonon interactions through $\mathcal{G}$ must be taken into

account.

The tensor $\mathcal{G}$ is known as a propagator and is given by

$$\mathcal{G}_{i_L \ldots i_1 l} = M_{i_1 l} e^{\mathcal{K}_{ll}(0)+2\mathcal{K}_{i_1 l}(1)+2\mathcal{K}_{i_2 l}(2)+\cdots+2\mathcal{K}_{i_L l}(L)} . \tag{3.3.32}$$

It can be written explicitly in terms of $K_{jj'}(s)$ as

$$\begin{aligned} \mathcal{G}_{i_L \ldots i_1 l} &= M_{i_1 l} \exp\{\xi_l \xi_l K_{11}(0) + \eta_l \eta_l K_{22}(0) \\ &\quad + 2\xi_{i_1}\xi_l K_{11}(1) + 2\eta_{i_1}\eta_l K_{22}(1) + 2(\xi_{i_1}\eta_l + \eta_{i_1}\xi_l)K_{12}(1) \\ &\quad + \ldots \\ &\quad + 2\xi_{i_L}\xi_l K_{11}(L) + 2\eta_{i_L}\eta_l K_{22}(L) + 2(\xi_{i_L}\eta_l + \eta_{i_L}\xi_l)K_{12}(L)\}, \end{aligned} \tag{3.3.33}$$

with each element of the tensor corresponding to a particular realisation of the system. The matrix $\hat{G}$ given by Eq. (3.3.30) is the simplest, $L = 1$ form of the more general influence tensor $\mathcal{G}$ containing the information required to propagate the system by a single time step. It includes the path segments connecting the current time interval with the L nearest intervals and to itself which are shown by the L shaped dashed black outlines in Fig. 3.4. The linear polarisation is then given by

$$\mathrm{P}_{jk}(t) = e^{\xi_j^2 K_{11}(0)+\eta_j^2 K_{22}(0)} F^{(N)}_{C\ldots Cj} , \tag{3.3.34}$$

where j is the measurement mode. The indices being placed in the cavity (C) state have the result of removing the excess contributions from the $\mathcal{G}$ tensor falling outside of the observation time t_{obs} (see Fig. 3.4), as being in the cavity state reduces the cumulant at the required times steps to zero. Equation (3.3.34) provides an asymptotically exact solution for the linear polarisation. This method can be generalised to other elements of the density matrix, such as the FWM polarisations [44] and the populations [79].

3.3.5 Independent phonon baths

The case of independent phonon baths can be considered as a simplification to the previous system, where the relevant modifications to the system Hamiltonian are applied to the H_{IB} term,

$$H_{\mathrm{IB}} = H_{\mathrm{ph},1} + H_{\mathrm{ph},2} + d_1^\dagger d_1 V_1 + d_2^\dagger d_2 V_2 \,, \tag{3.3.35}$$

which now describes the interaction of each exciton with its own independent phonon bath as well as the phonon energies, given by

$$V_1 = \sum_{\mathbf{q}} \lambda_{\mathbf{q},1}(b_{\mathbf{q},1} + b_{-\mathbf{q},1}^\dagger) \,, \quad V_2 = \sum_{\mathbf{q}} \lambda_{\mathbf{q},2}(b_{\mathbf{q},2} + b_{-\mathbf{q},2}^\dagger) \,, \tag{3.3.36}$$

and

$$H_{\mathrm{ph},1} = \sum_{\mathbf{q}} \omega_{q,1} b_{\mathbf{q},1}^\dagger b_{\mathbf{q},1} \,, \quad H_{\mathrm{ph},2} = \sum_{\mathbf{q}} \omega_{q,2} b_{\mathbf{q},2}^\dagger b_{\mathbf{q},2} \,, \tag{3.3.37}$$

respectively. Initially this may seem like a complication due to the extra terms, however the cumulant $\mathcal{K}_{i_n i_m}$ in Eq. (3.3.13) is non-vanishing only when $i_n = i_m$, i.e. the phonon autocorrelation functions for the cross terms vanish,

$$\langle \mathcal{T} \tilde{V}_1(\tau_1) \tilde{V}_2(\tau_2) \rangle = \langle \mathcal{T} \tilde{V}_2(\tau_1) \tilde{V}_1(\tau_2) \rangle = 0 \,. \tag{3.3.38}$$

This is because the phonon creation (annihilation) operators $b_{\mathbf{q},1}^\dagger$ ($b_{\mathbf{q},1}$) within V_1 commute with those ($b_{\mathbf{q},2}^\dagger$ and $b_{\mathbf{q},2}$) in V_2. The result is that the cumulant contains only $K_{jj'}$ terms for $j = j'$, giving

$$\mathcal{K}_{i_n i_m}(s) = \begin{cases} \xi_{i_n}^2 K_{11}(s) + \eta_{i_n}^2 K_{22}(s) & i_n = i_m \\ 0 & i_n \neq i_m \,. \end{cases} \tag{3.3.39}$$

The relevant modification of the final expression for the linear polarisation is within the $\mathcal{G}$ tensor given by Eq. (3.3.33), which now takes an explicit form

$$\begin{aligned} \mathcal{G}_{i_L \ldots i_1 l} \;=\; & M_{i_1 l} \exp\{\xi_{i_l}\xi_{i_l} K_{11}(0) + \eta_{i_l}\eta_{i_l} K_{22}(0) + 2\xi_{i_1}\xi_{i_l} K_{11}(1) + 2\eta_{i_1}\eta_{i_l} K_{22}(1) + \ldots \\ & \cdots + 2\xi_{i_L}\xi_{i_l} K_{11}(L) + 2\eta_{i_L}\eta_{i_l} K_{22}(L)\} \,, \end{aligned} \tag{3.3.40}$$

and is clearly different from and simpler than Eq. (3.3.33). The linear polarisation in this case is calculated using exactly the same Eq. (3.3.31) and Eq. (3.3.34) but with the modified propagator Eq. (3.3.40).

3.4 Summary

This chapter has detailed how the path-integral approach can be used to combine the JC and IB models leading to tensor-multiplication schemes. Focusing on a particular path-integral approach, the Trotter decomposition with linked cluster expansion technique [43], the necessary generalisations for multi-QD systems have been made. This provides an asymptotically exact calculation for the linear polarisation when the QDs are coupled to the same phonon bath, or interacting with independent baths. The propagator $\mathcal{G}$, a key tensor in this technique, is the highest-rank tensor and encapsulates all possible evolutionary paths of the system over a finite memory time. The number of time points within this memory time is denoted as the number of neighbours, L. Notably, increasing L enhances the accuracy of the results but comes at the cost of exponentially increasing storage demands, as it requires tracking a correspondingly larger number of possible paths. This approach is the basis for all calculations provided in the following chapter.

Chapter 4

Control of decoherence

4.1 Introduction

This chapter demonstrates a reduction, or even a complete elimination, of the ZPL dephasing in a system of two QD qubits coupled to each other directly or via an optical cavity and interacting with a bath of acoustic phonons. We show that, while the interaction of the hybridised qubits with a shared environment usually causes dephasing of qubit states, the coherent properties of the bath can help to reduce this decoherence. To do this, we use the Trotter's decomposition with linked cluster expansion technique described in the previous chapter, providing an asymptotically exact solution for the dynamics of spatially separated QD systems. The full calculations are compared with Fermi's golden rule (FGR), showing a remarkable agreement. Although there is a purely diagonal electron-phonon coupling, which typically produces no ZPL broadening, the full calculation reveals ZPL broadening understood in terms phonon-assisted transitions between the hybridised qubit states of the coupled QD system. It is shown that the ZPL broadening is reduced at specific inter-dot distances in a system of two QD qubits, which are coupled either directly or via an optical cavity and interact with a 3D bath of acoustic phonons. This suppression results from the collective coupling of

the QD qubits to shared phonon modes [49], enabled by the coherent properties of the bath. In particular, when the QD separation is an integer multiple of the phonon wavelength, provided it is within the phonon coherence length, there is a reduction in the decoherence. A near-vanishing dephasing rate, which can be referred to as a 1D regime, can be achieved by utilising strong QD-QD, or QD-cavity coupling strengths, paired with QD anisotropy. We quantify the QD separations at which the 1D-like regime persists before transitioning to the expected 3D behaviour.

For illustration, two cases are considered: *Case A*, where the qubits are directly coupled with strength g but do not interact with the cavity ($g_1 = g_2 = 0$); and *Case B*, where the qubits have no direct coupling ($g = 0$) but interact indirectly through the cavity, mediated by g_1 and g_2. To elucidate the effect of the shared environment on system coherence and its dependence on the inter-qubit distance $d = |\mathbf{d}|$, we assume that the coupling constants g_1, g_2, and g are distance independent. In a realistic system, *Case A* would typically exhibit a distance-dependent interaction between the QDs, such as dipolar Förster or tunnel coupling. However, we adopt a distance-independent coupling here as a simplified model to aid in understanding the more complex scenario in *Case B*. In *Case B*, the cavity mediates the interaction between the QDs, providing a more practical way to maintain strong coupling independent of their separation. We also choose without loss of generality that the first QD is instantaneously excited (e.g. by an ultrashort optical pulse), creating an excitonic polarisation with $\mathrm{P}_{jk}(0) = \delta_{jk}\delta_{k1}$.

4.2 Directly coupled QD qubits

4.2.1 Linear polarisation and dephasing rates

In *Case A*, the time evolution of $\mathrm{P}_{11}(t)$ for a system of two dipolar-coupled ($g = 0.5\,\mathrm{meV}$) identical isotropic QDs of confinement length $l = 5.6\,\mathrm{nm}$ separated by the center-to-center distance $d = 5\,\mathrm{nm}$, is shown in Fig. 4.1(a) by a blue dotted line, exhibiting decay and oscillations.

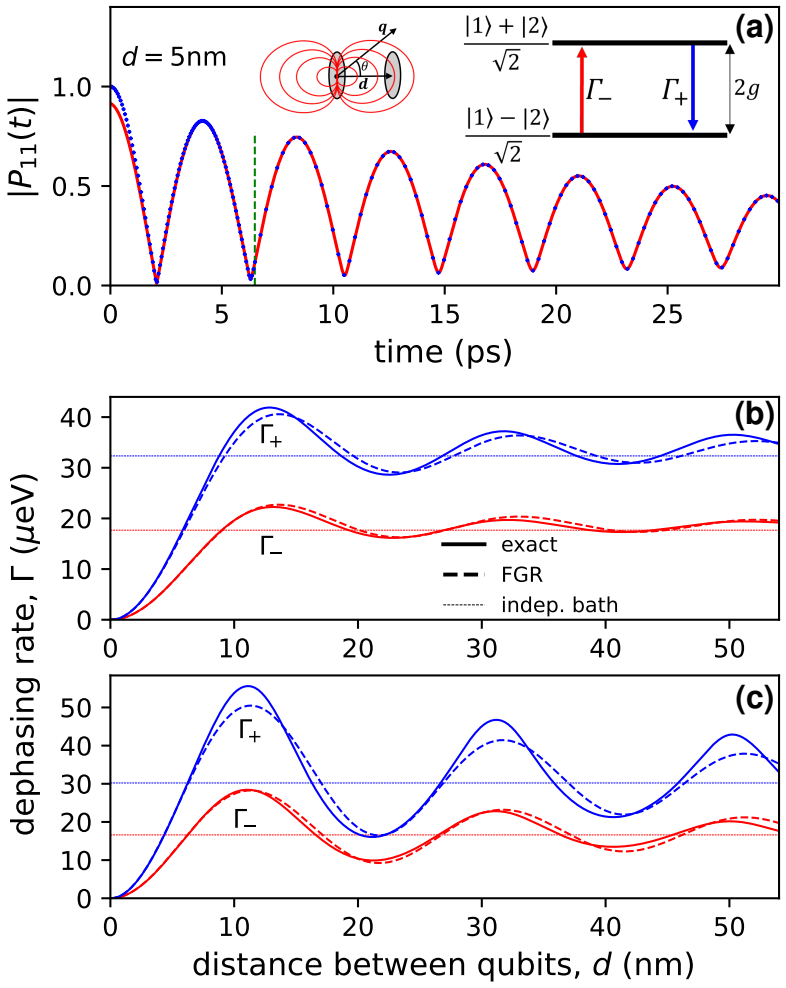

Figure 4.1: (a) Linear optical polarisation $P_{11}(t)$ (blue dots) and its complex bi-exponential fit (red lines) for dipolar coupled ($g = 0.5\,\text{meV}$) anisotropic QD qubits (left inset) at zero detuning in a 3D bath, separated by the distance $d = 5\,\text{nm}$, with excitation and measurement in QD 1. Right inset: energy level diagram for the hybridised qubit states, with real phonon-assisted transitions (red and blue arrows). (b,c) Dephasing rates $\Gamma_\pm$ of the hybridised states $|\pm\rangle$ as a function of d, calculated exactly (solid lines) and via FGR (dashed lines) for (b) isotropic QDs with a confinement length of $l = 5.6\,\text{nm}$ and (c) anisotropic QDs with $l = 7.5\,\text{nm}$ across and $l_\perp = 2.5\,\text{nm}$ along the separation (see Appendix H.1 and Appendix H.2 for details of isotropic and anisotropic QD models, respectively). The rates for independent phonon baths are shown by thin dashed lines. All calculations were performed using $L = 50$ neighbours. The phonon bath is at $T = 20\,\text{K}$ and the rest of the QD parameters can be found in Table 2.1.

The behaviour in Fig. 4.1(a) is qualitatively explained by the energy level diagram in the right inset, showing hybridised states $|\pm\rangle = (|1\rangle \pm |2\rangle)/\sqrt{2}$ of the two-qubit coupled system at zero detuning ($\Omega_1 = \Omega_2$), where $|1\rangle$ and $|2\rangle$ are the individual QD excited states. The energy levels are separated by the Rabi splitting $2g$ de-

termining the beat frequency in $|\mathrm{P}_{11}(t)|$ which physically expresses the quantum information exchange between the qubits. The temporal decay of the linear polarisation expresses the decoherence in this two-qubit system as a consequence of the interaction of the qubits with the bath. For these QD qubits, the decoherence is due to phonon-assisted transitions between the hybridised states.

With this picture in mind, we have applied to the long-time dynamics of $\mathrm{P}_{11}(t)$ a biexponential fit of the form

$$\mathrm{P}_{11}^{\mathrm{fit}}(t) = \sum_j C_j e^{-i\omega_j t}\,, \tag{4.2.1}$$

extracting the complex amplitudes C_j, energies Re ω_j, and dephasing rates $\Gamma_j = -\,\mathrm{Im}\;\omega_j$ of the phonon-dressed hybridised states. The fit, applied after the phonon-memory cut-off (introduced in Appendix I by analysing the cumulant functions and shown in Fig. 4.1(a) by the vertical dashed green line), demonstrates a remarkable agreement with the full calculation with a relative error below 10^{-10}. At earlier times the deviation is due to the formation of a polaron cloud around the optically excited QD, which is responsible for non-Markovian dephasing and the BB [13, 43, 44]. The dephasing rates Γ_j extracted from the fit as functions of the QD separation d are shown by solid lines in Fig. 4.1(b) for isotropic and in Fig. 4.1(c) for anisotropic QDs. They are the dephasing rates of the states $|\pm\rangle$, denoted by $\Gamma_\pm$, and can be understood as being due to phonon-assisted transitions between the states. At short distances we observe a dramatic increase of the dephasing rates from zero at zero distance (which cannot be practically realised due to the finite extension of the QDs), followed by an oscillatory behavior at larger distances. Importantly, the minima of these dephasing rates are lower than the independent baths rates (thin horizontal lines) due to collective coupling of the QD qubits to the same phonon modes, provided that the distance between the QDs is less than the phonon coherence length.

4.2.2 Phonon-assisted transitions between hybridised qubit states

To understand the dependence on the distance between the qubits, we introduce the fermionic operators

$$p_{\pm}^{\dagger} = D_{\mp} d_1^{\dagger} \pm D_{\pm} d_2^{\dagger}\,, \tag{4.2.2}$$

creating excitations of the hybridised QD qubit states

$$|\pm\rangle = D_{\mp}|1\rangle \pm D_{\pm}|2\rangle\,, \tag{4.2.3}$$

where

$$D_{\pm} = \sqrt{(1 \pm \Delta/R)/2}\,, \tag{4.2.4}$$

with

$$\Delta = \Omega_2 - \Omega_1 \quad \text{and} \quad R = \sqrt{\Delta^2 + 4g^2} \tag{4.2.5}$$

being, respectively, the detuning and the Rabi splitting. In the absence of the bath, these operators diagonalise the system Hamiltonian Eq. (3.2.2) (in the absence of the cavity) exactly:

$$H_0 = \Omega_+ p_+^{\dagger} p_+ + \Omega_- p_-^{\dagger} p_-\,, \tag{4.2.6}$$

where

$$\Omega_{\pm} = \frac{\Omega_1 + \Omega_2 \pm R}{2} \tag{4.2.7}$$

are the energies of the hybridised states $|\pm\rangle$.

Now applying this canonical transformation to the total Hamiltonian Eq. (3.2.1) we obtain

$$H = (\Omega_+ + V_+) p_+^{\dagger} p_+ + (\Omega_- + V_-) p_-^{\dagger} p_- + V(p_+^{\dagger} p_- + p_-^{\dagger} p_+) + H_{\rm ph}\,, \tag{4.2.8}$$

where $V_{\pm} = D_{\mp}^2 V_1 + D_{\pm}^2 V_2$ and $V = D_+ D_- (V_1 - V_2)$. The major outcome of this transformation is that the formerly diagonal interaction with the bath $H_{\rm IB}$, given by Eq. (3.2.3), now develops the off-diagonal elements $V(p_+^{\dagger} p_- + p_-^{\dagger} p_+)$ which

enable phonon-assisted transitions between the hybridised qubit states, $|+\rangle \leftrightarrow |-\rangle$. Specifically, $p_+^\dagger p_-$ facilitates a transition from $|-\rangle$ to $|+\rangle$ (e.g., phonon absorption) and $p_-^\dagger p_+$ facilitates a transition from $|+\rangle$ to $|-\rangle$ (e.g., phonon emission). Using the bath interactions explicitly from from Eq. (3.2.4), V can be expressed as:

$$V = D_+D_-(V_1 - V_2) = D_+D_- \sum_{\mathbf{q}} (\lambda_{\mathbf{q},1} - \lambda_{\mathbf{q},2})(b_{\mathbf{q}} + b_{-\mathbf{q}}^\dagger) \tag{4.2.9}$$

To evaluate the transition rates between initial and final states, corresponding to the hybridised states, we employ FGR, which for a perturbation H' is given by:

$$\Gamma = 2\pi \sum_{i,f} |\langle f| H' |i\rangle|^2 \delta(E_f - E_i). \tag{4.2.10}$$

$$H' = V(p_+^\dagger p_- + p_-^\dagger p_+) = D_+D_- \sum_{\mathbf{q}'} (\lambda_{\mathbf{q}',1} - \lambda_{\mathbf{q}',2})(b_{\mathbf{q}'} + b_{-\mathbf{q}'}^\dagger)(p_+^\dagger p_- + p_-^\dagger p_+). \tag{4.2.11}$$

The initial and final states involve both the hybridised qubit states $|\pm\rangle$, given by Eq. (4.2.3) and the phonon bath states. Considering only the case of phonon absorption, where the system transitions from the lower state $|-\rangle$ to the upper state $|+\rangle$, we define the initial state $|i\rangle = |-, n_{\mathbf{q}}\rangle$ and final state $|f\rangle = |+, n_{\mathbf{q}} - 1\rangle$, where $n_{\mathbf{q}}$ is the definite number of phonons in mode $\mathbf{q}$. All other phonon modes are in fixed number states, not affecting this single-mode transition.

The relevant term for absorption in Eq. (4.2.11) is $Vp_+^\dagger p_-$:

$$Vp_+^\dagger p_- = D_+D_- \sum_{\mathbf{q}} (\lambda_{\mathbf{q},1} - \lambda_{\mathbf{q},2})(b_{\mathbf{q}} + b_{-\mathbf{q}}^\dagger) p_+^\dagger p_-, \tag{4.2.12}$$

thus, the matrix element in Eq. (4.2.10) is given by:

$$\langle f| Vp_+^\dagger p_- |i\rangle = D_+D_- \sum_{\mathbf{q}'} (\lambda_{\mathbf{q}',1} - \lambda_{\mathbf{q}',2}) \langle +, n_{\mathbf{q}} - 1| (b_{\mathbf{q}'} + b_{-\mathbf{q}'}^\dagger) p_+^\dagger p_- |-, n_{\mathbf{q}}\rangle . \tag{4.2.13}$$

Noting that $p_+^\dagger p_- |-\rangle = |+\rangle$, and $b_{-\mathbf{q}}^\dagger$ raises the phonon number, which is not desired for absorption, and also the phonon destruction operator has the following

effect: $b_{\mathbf{q}}|n_{\mathbf{q}}\rangle = \sqrt{n_{\mathbf{q}}}|n_{\mathbf{q}}-1\rangle$. Thus,

$$D_+D_-\sum_{\mathbf{q}'}(\lambda_{\mathbf{q}',1}-\lambda_{\mathbf{q}',2})\langle +,n_{\mathbf{q}}-1|\, b_{\mathbf{q}'}p_+^\dagger p_-\,|-,n_{\mathbf{q}}\rangle = D_+D_-(\lambda_{\mathbf{q},1}-\lambda_{\mathbf{q},2})\sqrt{n_{\mathbf{q}}}, \tag{4.2.14}$$

since the summation over $\mathbf{q}'$ gives only a nonzero result when $\mathbf{q}'=\mathbf{q}$. Furthermore, the summation $\sum_{i,f}$ in Eq. (4.2.10) only occurs between a single initial and final hybridised state, as there are only two hybridised states. By considering only single-phonon interactions, the energy conservation requires $\omega_q = E_+ - E_-$, and noting that the energy difference $E_+ - E_-$ is the Rabi splitting, as defined in Eq.4.2.5, the transition rate for phonon absorption is given by:

$$\Gamma_{-,n_{\mathbf{q}}} = 2\pi n_{\mathbf{q}}|D_+D_-(\lambda_{\mathbf{q},1}-\lambda_{\mathbf{q},2})|^2\delta(\omega_q - R). \tag{4.2.15}$$

However, we must properly introduce the thermal average by summing over all possible initial phonon numbers, weighted by their thermal probabilities:

$$\Gamma_{-,\mathbf{q}} = \sum_{n_{\mathbf{q}}=0}^{\infty} P(n_{\mathbf{q}})\Gamma_{-,n_{\mathbf{q}}}, \tag{4.2.16}$$

where $P(n_{\mathbf{q}})$ is the thermal probability of having $n_{\mathbf{q}}$ phonons in mode $\mathbf{q}$: $P(n_{\mathbf{q}}) = \frac{e^{-\beta\omega_q n_{\mathbf{q}}}}{Z}$, with $Z = \sum_{n=0}^{\infty} e^{-\beta\hbar\omega_q n} = \frac{1}{1-e^{-\beta\hbar\omega_q}}$ being the partition function. For each mode $\mathbf{q}$, the thermal average gives:

$$\Gamma_{-,\mathbf{q}} = 2\pi|D_+D_-(\lambda_{\mathbf{q},1}-\lambda_{\mathbf{q},2})|^2\delta(\omega_q - R)\sum_{n_{\mathbf{q}}=0}^{\infty} P(n_{\mathbf{q}})n_{\mathbf{q}}\,. \tag{4.2.17}$$

Since $\sum_{n_{\mathbf{q}}=0}^{\infty} P(n_{\mathbf{q}})n_{\mathbf{q}} = N(\omega_q)$, we find

$$\Gamma_{-,\mathbf{q}} = 2\pi N(\omega_q)|D_+D_-(\lambda_{\mathbf{q},1}-\lambda_{\mathbf{q},2})|^2\delta(\omega_q - R). \tag{4.2.18}$$

A further sum over $\mathbf{q}$ appears because any mode $\mathbf{q}$ that satisfies the energy conservation condition $\omega_q = R$ can contribute to the transition. Therefore, the total

transition rate sums over all possible modes, giving

$$\Gamma_- = \sum_{\mathbf{q}} \Gamma_{-,\mathbf{q}} = 2\pi \sum_{\mathbf{q}} N(\omega_q) |D_+ D_-(\lambda_{\mathbf{q},1} - \lambda_{\mathbf{q},2})|^2 \delta(\omega_q - R). \tag{4.2.19}$$

The same procedure can be applied for the case of phonon emission, which gives:

$$\Gamma_+ = 2\pi \sum_{\mathbf{q}} (N(\omega_q) + 1) |D_+ D_-(\lambda_{\mathbf{q},1} - \lambda_{\mathbf{q},2})|^2 \delta(\omega_q - R). \tag{4.2.20}$$

This leads us to the transition rates [43, 46]:

$$\Gamma_- = N(R)\,\Gamma_{\rm ph}\,, \quad \Gamma_+ = (N(R)+1)\,\Gamma_{\rm ph}\,, \tag{4.2.21}$$

which we call the dephasing rates of the lower and upper hybridised states, respectively. Here, $\Gamma_{\rm ph}$ is given by:

$$\Gamma_{\rm ph} = \pi \sum_{\mathbf{q}} \left| D_+ D_- \left(\lambda_{\mathbf{q},1} - \lambda_{\mathbf{q},2}\right)\right|^2 \delta(v_s q - R)\,, \tag{4.2.22}$$

which uses the linear phonon dispersion $\omega_q = v_s q$. A factor of $1/2$ has further been added to account for the fact that FGR calculates the rate of real transitions changing the population, which is double the corresponding dephasing rate seen in the polarisation. The rate $\Gamma_{\rm ph}$ is evaluated in Appendix J.1, providing for an isotropic model of the QDs the explicit analytical result:

$$\Gamma_{\rm ph} = \Gamma_0 \left(1 - \frac{\sin(Rd/v_s)}{Rd/v_s}\right)\,, \tag{4.2.23}$$

where $\Gamma_0 = D_+^2 D_-^2 R^3 (D_c - D_v)^2/(2\pi\rho_m v_s^5) e^{-l^2R^2/v_s^2}$. The corresponding FGR calculation for an anisotropic model of the QDs is provided in Appendix J.1.2.

The FGR dephasing rates Eq. (4.2.23) are shown in Fig. 4.1(b) as dashed lines, reproducing the main features of the exact calculation, but showing discrepancies (within 5%) due to multi-phonon processes not present in FGR. The single-phonon transitions dominate at short distances as it is clear from the excellent agreement

between the two results.

When higher-order phonon interactions are considered (e.g. cubic interactions in Ref.38), there is a finite phonon coherence time, and thus a finite coherence length. While our model does not take into account anything leading to finite coherence lengths, we can distinguish two regimes: 1) The dot separation is less than the phonon coherence length, and thus the QDs can experience the same coherent phonon field and the collective coupling to the bath leads to the oscillations in our plots. 2) The independent bath calculation is similar to when the QD separation is larger than the coherence length, in which case the QDs do not interact with the same phonon field. Thus, the initial quadratic growth with distance, the oscillations, and the reduction of $\Gamma_\pm$ at certain distances, seen in Fig. 4.1(b), are all caused by the coherent properties of the phonon bath. According to Eq. (4.2.8), the phonon-assisted coupling between the hybridised qubit states is given by $V_1 - V_2$ which is proportional to $1 - e^{i\mathbf{q}\cdot\mathbf{d}}$ for identical QDs (see Eq. (3.2.5)) and is vanishing at $\mathbf{q}\cdot\mathbf{d} = 2\pi n$, where n is an integer. This does not lead to a vanishing dephasing though, apart from $d = 0$, owing to the 3D nature of the phonon momentum $\mathbf{q}$ of the bath modes. However, as we show in Appendix J.1, in a 1D model of phonons with the same dispersion and same coupling, the dephasing rate Eq. (4.2.23) would modify to just

$$\Gamma_{\text{ph}} = \Gamma_0 \left(\frac{v_s}{Rl}\right)^2 \sin^2\left(\frac{Rd}{2v_s}\right) , \tag{4.2.24}$$

strictly vanishing at $Rd/v_s = 2\pi n$ for all n.

4.2.3 Physical interpretation of decoherence reduction

To understand the vanishing dephasing rate phenomenon in 1D, let us take the two-qubit state just before the event of phonon emission or absorption as a superposition $\alpha|1\rangle + \beta|2\rangle$ with some complex amplitudes α and β. Since the qubits are in a hybridised state, they coherently emit or absorb the same phonon. This changes their phases (which is the source of pure dephasing) by φ_1 and φ_2, respectively, so that the two-qubit wave function becomes $\alpha e^{i\varphi_1}|1\rangle + \beta e^{i\varphi_2}|2\rangle$, with $\varphi_2 - \varphi_1 = \pm qd$, according to Eq. (3.2.5) and energy conservation requiring $R = v_s q$. However, if

the separation d between the qubits is such that the phase difference is a multiple of 2π, i.e. $Rd/v_s = 2\pi n$ for an integer n, the resulting wave function only acquires a common phase factor $e^{i\varphi_1}$, which is not changing the state since there is no relative phase difference between qubit states. In other words, in order for the transition to occur between the initial and final states [e.g. between $|+\rangle$ and $|-\rangle$, see the inset in Fig. 4.1(a)], which would result in a phonon-induced dephasing, a change of the two-qubit state is required, meaning that the interaction with a phonon must induce a relative phase shift, i.e. $Rd/v_s \neq 2\pi n$.

Early papers revealed similar oscillatory behavior of the transition rates with distance in systems of spatially separated tunnel coupled QDs [49, 86]. However, these are calculated approximately and are based on off-diagonal coupling between electronic states within the same QD, which is known to lead to long-time decoherence [37]. Ref.87 showed spatial correlations strongly influenced the quantum coherent transfer of excitations between biomolecular chromophores, however the model is using distance-independent dipolar coupling and does not reveal oscillations in the dephasing rates. When considering more realistic couplings which decrease rapidly with distance, e.g. Förster coupled QDs in [82], or the tunnel coupling in [88], the oscillations disappear. There are also further studies which look at the distance dependence of exciton and spin QD qubits that reveal no oscillations with distance [89]. This is the motivation for introducing a cavity, so that long-distance strong coupling can be maintained.

Note that in the case of e.g. nanowire-based QDs [56] or QDs in carbon nanotubes [90, 91], the phonon dispersion and coupling are altered when the dimensionality is reduced from a bulk system. Several branches of phonon modes arise due to the reduced dimensionality and phonon quantisation which are not present in 3D systems. This leads to changes in the phonon dispersion and coupling matrix elements, and ultimately, the phonon spectral density $J_{jj'}(\omega)$. As a result, there is a finite zero-phonon linewidth which is not observed in QDs coupled to bulk phonons, where the linewidth remains zero in the ideal case. Here, the ideal

case corresponds to the condition $qd = 2\pi n$, for which no broadening of the ZPL is observed, due to the phonon interactions not facilitating a change of state, making the system effectively equivalent to the independent boson model [54] in which there is no ZPL broadening.

4.2.4 Anisotropic QD qubits

For 3D phonons and isotropic QDs, the dephasing is absent only at $d = 0$ and according to Eq. (4.2.23) and Fig. 4.1(b) has minima around $Rd/v_s = 2\pi n + \pi/2$ ($n = 1, 2, \dots$). The $\pi/2$ phase shift compared to the 1D case and non-vanishing dephasing at the minima are due to phonons of energy R that are absorbed or emitted at different angles θ to the QD separation vector $\mathbf{d}$ (Fig. 3.1), resulting in a variation of their phase difference $\varphi_2 - \varphi_1$ between the QDs. However, the reduction of decoherence is enhanced in anisotropic QDs, playing the role of directional phonon emitters or absorbers [92]. In fact, in oblate QDs separated along their short axis (Fig. 4.1(c)), directional coupling of phonons along the short axis effectively makes the system 1D under certain conditions.

Notably, in earlier studies, e.g. Ref.49 and Ref.86, the influence of the 3D bath is not obvious because the models are using a very strong anisotropy. Consequently, the studies are in a 1D-like regime, with little insight into the transition between 1D and 3D regimes. A follow-up work of Ref.49 discussed the loss of the 1D-regime by changing the effective mass in their system [93], which is reducing the confinement length in the in-plane parabolic confining potentials for electrons. Similarly, models with spherical QDs or weaker anisotropy yield finite dephasing rates across all separations, as seen from our calculation in Fig. 4.1, reflecting the influence of the 3D bath.

The dephasing rates for anisotropic QDs, calculated via FGR in Appendix J.1.2

have a compact analytical expression

$$\Gamma_{\rm ph} = \frac{D_+^2 D_-^2 (D_c - D_v)^2}{2\pi\rho_m v_s^5} R^3 e^{-q^2 l_\perp^2} \left[F\left(0, q\sqrt{l_\perp^2 - l^2}\right) - F\left(\frac{d}{2\sqrt{l_\perp^2 - l^2}}, q\sqrt{l_\perp^2 - l^2}\right)\right], \tag{4.2.25}$$

which is expressed in terms of the Faddeeva function. The properties of the Faddeeva function can be found in Appendix H.3. Eq.4.2.25 reproduces the main features of the exact calculation (with a relative difference below 7%), as seen in Fig. 4.1(c). In this case $l \gg l_\perp$, where l and $l_\perp$ are, respectively, the in-plane and perpendicular (along $\mathbf{d}$) exciton localisation lengths, so that for $d \ll 2l^2 q$, where $q = R/v_s$, the dephasing rates vanish at $qd = 2\pi n$, as it is clear from Eq. (H.30) in Appendix H.3. If additionally $ql \gg 1$, meaning that the relevant phonon wavelength is small enough to create a directional emission, the FGR dephasing rates reduce to Eq. (4.2.24). Under these conditions, the 3D system behaves as a 1D system, however, as the dot separation is increased, the 3D nature gradually returns. Furthermore, the 1D regime can be extended by increasing the anisotropy or increasing the energy R of the dominant phonon modes which couple to the system. In fact, the analogy with pure 1D phonons becomes striking for stronger coupled

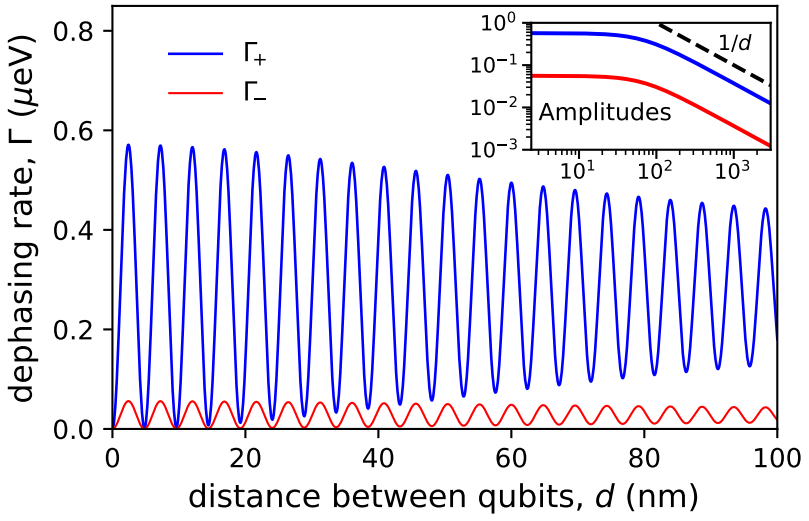

Figure 4.2: As Fig. 4.1(c) but for $g = 2\,\text{meV}$ and FGR only (solid lines). Inset: Amplitude of the oscillations in the dephasing rates versus distance.

QDs ($g = 2\,\text{meV}$) as shown in Fig. 4.2, where the shorter phonon wavelength involved in transitions provides fast oscillations versus d, allowing for minima at

short distances with near-vanishing dephasing. With such coupling strengths, the aforementioned condition $ql \gg 1$ is met, having a value $ql = 10$. The scaling of the oscillation amplitude with distance, given in the inset, demonstrates the quasi-1D behaviour (shown by constant amplitude) for $d \ll 2l^2q \approx 148\,\mathrm{nm}$. This is consistent with the first few minima in the main plot having visually very small dephasing rates before gradually returning to the 3D regime as the dot separation increases. For this directional emission of phonons, the phonon Rayleigh length, given by $d_R = l^2q/2 \approx 37\,\mathrm{nm}$, estimates how far the phonons can propagate as a focused beam, maintaining 1D-like behavior. Beyond this distance, the system gradually transitions back to 3D. For 1D behavior to persist, the condition on the qubit separation then becomes $d \ll 4d_R$, where d_R serves as a reasonable upper limit for ensuring the system remains in the 1D regime.

4.3 Cavity-mediated coupled QD qubits

In *Case B*, considering QDs indirectly coupled via a cavity, the dephasing is also controlled by collective coupling to the shared bath, though in a more complex scenario. For zero detuning ($\Omega_1 = \Omega_2 = \Omega_C$) and equal QD-cavity couplings ($g_1 = g_2 = \bar{g}$) with no direct coupling ($g = 0$), the resulting three coupled states, $|+,\pm\rangle = (|1\rangle + |2\rangle)/2 \pm |C\rangle/\sqrt{2}$ and $|-\rangle = (|1\rangle - |2\rangle)/\sqrt{2}$ require a triexponential fit of $\mathrm{P}_{11}(t)$ to extract the dephasing rates $\Gamma_j = -\,\mathrm{Im}\,\omega_j$, which are shown in Fig. 4.3 across a range of distances, see Appendix K for details of the fit.

We observe oscillations versus distance d, different from those of directly coupled QDs (Fig. 4.1) since there are two periods contributing to the dephasing rates $\Gamma_{+,\pm}$ of the states $|+,\pm\rangle$. This is due to the involvement of transitions at two distinct frequencies, as seen in the right inset, with one twice the other (the general case of a non-zero detuning with three different frequencies involved is considered in Appendix J.2). Since the dephasing rate Γ_- of the state $|-\rangle$ involves transitions to the two other levels with equal Rabi splitting and thus the interacting phonons have almost the same energy, only one period is observed in the oscillations of

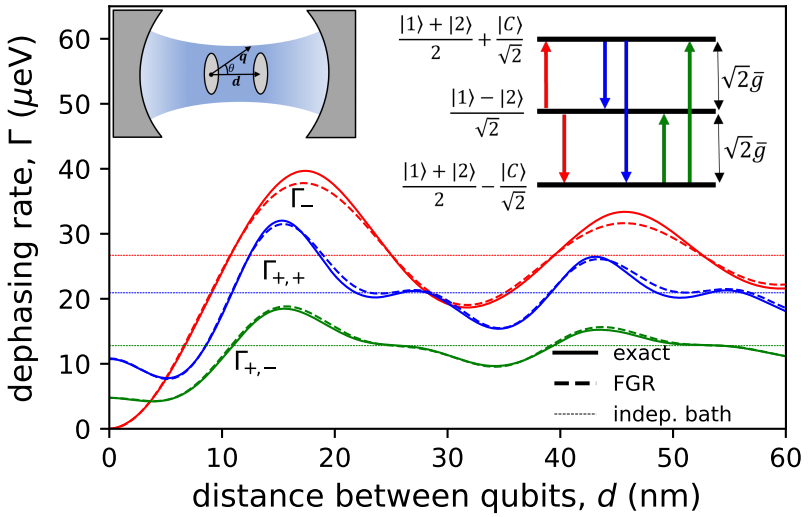

Figure 4.3: Dephasing rates $\Gamma_{+,\pm}$ and Γ_{-} of the hybridised states as a function of d. Calculated exactly (solid lines) and via FGR (dashed lines) for cavity-mediated coupled anisotropic qubits in a 3D bath (left inset) with interaction strength $g_1 = g_2 = \bar{g} = 0.5\,\mathrm{meV}$, no direct coupling ($g = 0$) and zero detuning. The dephasing rates for independent phonon baths are shown by thin dashed lines. Right inset: Energy level diagram for the hybridised qubit-cavity states $|+,\pm\rangle = (|1\rangle + |2\rangle)/2 \pm |C\rangle/\sqrt{2}$ and $|-\rangle = (|1\rangle - |2\rangle)/\sqrt{2}$, with real phonon-assisted transitions (red, blue and green arrows). The calculation was performed using $L = 36$ neighbours. The phonon bath is at $T = 20\,\mathrm{K}$ and the other parameters are as in Fig. 4.1(c).

Γ_{-}, analogous to *Case A*, with vanishing dephasing rate at $d = 0$. In general, $\Gamma_{+,+}$ (consisting of two downwards transitions) will always be greater than $\Gamma_{+,-}$ (two upwards transitions), simply because of spontaneous phonon emission. Furthermore, whether Γ_{-} or $\Gamma_{+,+}$ is the largest on average depends on the coupling strength chosen. If the Rabi splitting ($\sqrt{2}\bar{g}$) for the transitions contributing to Γ_{-} is closer to the peak in the phonon spectral density than the energy ($2\sqrt{2}\bar{g}$) of the distant-level transitions included in $\Gamma_{+,-}$, then Γ_{-} is the largest dephasing rate.

Due to the nature of the hybridised QD-cavity states, the exciton-phonon matrix elements contributing to FGR are now proportional to $V_1 \pm V_2$, with $+$ $(-)$ corresponding to the transitions between distant (neighbouring) levels, see Appendix J.2 for details. Since transitions between distant levels contribute to $\Gamma_{+,\pm}$ and thus involve $V_1 + V_2$, there is a non-vanishing contribution even at $d = 0$. This is because the states involved in such transitions both have a cavity contribution,

and as cavity does not couple to phonons, the reduction of the dephasing rate to zero is not observed. However, these transition have typically lower impact on decoherence due to the larger phonon energy involved, as discussed in more detail in Appendix J.2.

4.4 Summary

This chapter has used the asymptotically exact solution developed in the previous chapter to study the linear optical response of a system of two coupled qubits interacting with a shared bath, using semiconductor quantum dots coupled to 3D acoustic phonons as illustration. From this, the dephasing rates across a range of distances are extracted and studied. Although only diagonal exciton-phonon coupling is considered, which typically produces no ZPL broadening, the full calculation reveals ZPL broadening understood in terms phonon-assisted transitions between the hybridised qubit states. A reduction of the ZPL dephasing is demonstrated by controlling the distance between the qubits in relation to the wavelength of the interacting bath modes, showing a remarkable agreement with FGR calculations. This effect is due to all qubits coupling to the same phonon mode, a consequence of the coherent properties of the bath. It is shown that for a 1D bath, decoherence can be eliminated entirely, a case which can also be approached for anisotropic qubits in a 3D bath. We considered a system with a cavity such that the cavity mediates the interaction between the QDs, providing a practical way to achieve coupling which is maintained for large qubit separations.

Chapter 5

Optimisation of path-integral tensor-multiplication schemes in open quantum systems

5.1 Introduction

Path-integral techniques are a powerful tool used in open quantum systems to provide an exact solution for the non-Markovian dynamics, as seen in the last chapter. However, the exponential tensor scaling with the number of neighbours within the memory time of these techniques limits the applicability when dealing with systems of long memory times. This is because as the memory time increases, more neighbours must be added to maintain accuracy, however, this may not be achievable due to storage and computational limitations. To clarify, as the memory time increases, the number of correlations, or equivalently the number of time steps contained within the memory kernel must be increased to maintain accuracy. If there are too few correlations considered, the dynamics will not be well resolved, leading to a lack of accuracy.

In this chapter, an optimisation scheme is developed which reduces the tensor sizes by remapping them to matrices and utilising singular value decomposition (SVD) to filter out contributions, reducing storage requirements and computational time. More specifically, the time steps considered in the memory time (neighbours) are split across two separate matrices. This approach dramatically reduces both computational time and memory usage of the traditional tensor-multiplication schemes. For reference, to achieve the new level of accuracy using the original method detailed in Chapter 3, it would require over 50 million GB of RAM. Additionally, the approach in this chapter enables the usage of an extrapolation scheme which approximates the exact ($L \to \infty$) long-time dynamics. Furthermore, in cases where calculations are already well converged using the original tensor-multiplication scheme, the optimisation provides substantial time savings, often improving computational time by up to two orders of magnitude. As a demonstration, we apply it to the Trotter decomposition with linked cluster expansion technique presented in Chapter 3, and use it to investigate a quantum dot micro-cavity system at larger coupling strengths than previously achieved. Secondly, we also show the necessity of the optimisation when the memory time is very long—specifically in spatially extended systems coupled to a common environment, such as the coupled qubit systems studied in Chapter 4. Physically, the long memory times are due to the shared bath, where phonons may travel between the QDs and the larger the dot separation, the larger the memory time.

This optimisation, which remaps and splits the tensor into *two* matrices, is a simple and natural stepping stone to a more sophisticated and advanced version of optimisation which has now been developed at the time of writing this thesis. The new version represents the tensor as an arbitrary number of matrices (limited by memory), where each matrix can contain a similar number of neighbours as the optimisation described in this chapter, providing a significant increase in the maximum number of neighbours achievable. It should be noted, however, that the downside of this technique compared to other modern approaches is that it scales poorly with system size, i.e. the number of reduced density matrix elements.

5.2 Systems and Hamiltonians

Presently, this optimisation, as well as the developed Trotter's decomposition with linked cluster expansion technique, can be applied to systems consisting of any number of TLSs that are directly coupled and interact with an environment, either a shared one or independent environments. Additionally, they may interact with an arbitrary number of microcavities.

The general form of Hamiltonian that is treatable is

$$H = H_0 + H_{IB} + H_B, \tag{5.2.1}$$

where H_0 describes both the coupling between the TLSs and the TLS-cavity couplings, and is given by

$$H_0 = \sum_{ij} H_{ij} d_i^\dagger d_j + \sum_k \Omega_{C,k} a_k^\dagger a_k + \sum_{jk} g_{jk} \left(d_j^\dagger a_k + a_k^\dagger d_j \right), \tag{5.2.2}$$

where H_{ij} are the matrix elements of the coupled TLSs, with the diagonal elements (H_{jj}) corresponding to the excitation energy of the TLS at site j, while the off-diagonal elements (H_{ij}, for $i \neq j$) describe the direct coupling between TLSs at sites i and j. The operator $d_j^\dagger$ creates an excitation in the two-level system at site j, and a photon in a cavity mode k has energy $\Omega_{C,k}$ and is created by the operator $a_k^\dagger$. Finally, the TLS at site j is coupled to a cavity mode k with strength g_{jk}. In general, there can be multiple baths of 3D bosons, described by

$$H_{\mathrm{B}} = \sum_l \sum_{\mathbf{q}} \omega_{q,l} b_{\mathbf{q},l}^\dagger b_{\mathbf{q},l}, \tag{5.2.3}$$

where $b_{\mathbf{q},l}^\dagger$ creates an excitation in the bath l with wave vector $\mathbf{q}$. The TLS-bath interaction is given by H_{int}:

$$H_{\mathrm{int}} = \sum_j d_j^\dagger d_j \sum_l \sum_{\mathbf{q}} \lambda_{\mathbf{q},jl} (b_{\mathbf{q},l} + b_{-\mathbf{q},l}^\dagger), \tag{5.2.4}$$

where $\lambda_{\mathbf{q},jl}$ describes the interaction strength of the TLS at site j with bath mode $\mathbf{q}$ in bath l. Eq. (5.2.4) can be used to describe the scenario where multiple TLSs are coupled to the same bath, or coupled to their own independent baths. The diagonal TLS-bath coupling is needed for an exact calculation using linked cluster expansion, however recently it was also shown that the path-integral based approaches can also be efficiently used for non-diagonal coupling [78].

This general spin-boson model can be reduced to describe many physical systems by choosing the number of TLSs and turning on/off specific coupling terms, such as energy transport in biological systems [94, 95], qubits in microwave resonators [96, 97], quantum dots interacting with a micromechanical resonator [98], and spin-qubit systems [99].

The specific implementation of the TLSs considered in this chapter are semiconductor QDs which are coupled to an environment modeled as a bath of acoustic phonons, consistent with the earlier chapters. Although the general Hamiltonian detailed above describes the range of problems this optimisation can treat, we reduce the Hamiltonian to two cases for illustration. *Case C*: A QD-cavity system coupled to a bath of acoustic phonons detailed in [43], and *Case B* (previously studied in Chapter 4): a QD-QD-cavity system coupled to the same phonon bath. For ease of reference, the Hamiltonians for each case are provided here. The Hamiltonian in *Case C* is:

$$H = H_0 + H_{\mathrm{IB}}\,, \tag{5.2.5}$$

where H_0 describes the coupling between the QD and the cavity, and H_{IB} is a generalised IB model Hamiltonian describing the coupling of the QD to the environment. H_0 takes the form

$$H_0 = \Omega_X d^\dagger d + \Omega_C a^\dagger a + g(d^\dagger a + a^\dagger d)\,, \tag{5.2.6}$$

where $d^\dagger$ is the fermionic exciton creation operator in the QD, $a^\dagger$ is the cavity photon creation operator, Ω_X (Ω_C) is the exciton (cavity photon) energy, g is

the coupling strengths between the QD and cavity. The IB model Hamiltonian describes the interaction of the QD exciton with an acoustic-phonon bath,

$$H_{\mathrm{IB}} = H_{\mathrm{ph}} + d^\dagger d V \,, \tag{5.2.7}$$

where

$$H_{\mathrm{ph}} = \sum_{\mathbf{q}} \omega_q b_{\mathbf{q}}^\dagger b_{\mathbf{q}} \quad \text{and} \quad V = \sum_{\mathbf{q}} \lambda_{\mathbf{q}} (b_{\mathbf{q}} + b_{-\mathbf{q}}^\dagger) \tag{5.2.8}$$

are, respectively, the free phonon bath Hamiltonian and the QD coupling to the bath, where $b_{\mathbf{q}}^\dagger$ is the bosonic creation operator of a bulk phonon mode with the momentum $\mathbf{q}$ and frequency ω_q (denoting $q = |\mathbf{q}|$). The coupling of the exciton in the QD to the phonon mode $\mathbf{q}$ is given by the matrix element $\lambda_{\mathbf{q},j}$, which depends on the material parameters, exciton wave function, and position of the QD. Their explicit form for isotropic QDs is provided in Appendix H.

The explicit Hamiltonian for *Case B* is:

$$H = H_0 + H_{\mathrm{IB}} \,, \tag{5.2.9}$$

where H_0 describes the coupling between the qubits and the cavity, and H_{IB} is a generalised IB model Hamiltonian describing the coupling of the qubits to the shared environment. For the system of two remote QDs coupled to an optical cavity, H_0 takes the form

$$H_0 = \Omega_1 d_1^\dagger d_1 + \Omega_2 d_2^\dagger d_2 + \Omega_C a^\dagger a + g_1 (d_1^\dagger a + a^\dagger d_1) + g_2 (d_2^\dagger a + a^\dagger d_2) \,, \tag{5.2.10}$$

where $d_j^\dagger$ is the fermionic exciton creation operator in QD j ($j = 1, 2$), $a^\dagger$ is the cavity photon creation operator, Ω_j (Ω_C) is the exciton (cavity photon) energy, and g_j is the coupling strengths between the exciton in QD j and the cavity photon. The IB model Hamiltonian describes the interaction of the QD excitons with a shared acoustic-phonon bath,

$$H_{\mathrm{IB}} = H_{\mathrm{ph}} + d_1^\dagger d_1 V_1 + d_2^\dagger d_2 V_2 \,, \tag{5.2.11}$$

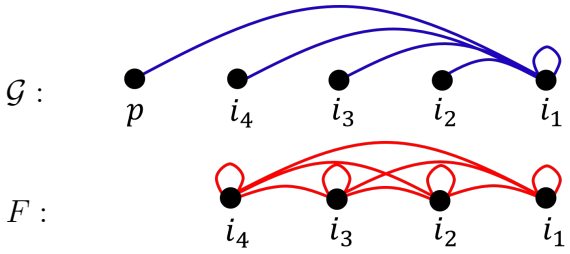

Figure 5.1: Diagrams showing the path segments contained within $\mathcal{G}$ (blue) and F (red) for $L = 4$. The propagator $\mathcal{G}$ contains path segments connecting the index i_1 to itself and to all other considered neighbours, i_n. Each link is weighted appropriately and is zero if there is no interaction, forming a memory kernel. The full influence functional F represents the information about the state of the system and contains all possible path segments.

where

$$H_{\text{ph}} = \sum_{\mathbf{q}} \omega_q b^\dagger_{\mathbf{q}} b_{\mathbf{q}} \quad \text{and} \quad V_j = \sum_{\mathbf{q}} \lambda_{\mathbf{q},j} (b_{\mathbf{q}} + b^\dagger_{-\mathbf{q}}) \,, \tag{5.2.12}$$

The coupling of the exciton in a QD at site j to the phonon mode $\mathbf{q}$ is given by the matrix element $\lambda_{\mathbf{q},j}$, which depends on the material parameters and exciton wave function, and for multiple QDs in the same phonon bath, the position of the QD. Their explicit form for isotropic QDs is provided in Appendix H. Importantly, *Case B*, which describes a pair identical coupled QDs in a shared environment separated by a distance vector $\mathbf{d}$, the matrix elements satisfy an important relation for identical QDs:

$$\lambda_{\mathbf{q},2} = e^{i\mathbf{q}\cdot\mathbf{d}} \lambda_{\mathbf{q},1} \,, \tag{5.2.13}$$

which is the source of long memory times, as discussed in Chapter 4. Physically, the long memory times are due to the shared bath, where phonons may travel between the QDs. So, the memory time can be as long as the phonon coherence time, and the larger the dot separation, the larger the memory time, which manifests itself as a delay in the bath correlation functions (see Fig. I.2 in Appendix I).

5.3 Path-integral approach

This section contains some information already provided and derived in more detail within Chapter 3, however some more insight and subtleties are provided alongside the partially repeated information.

For illustration we consider the linear polarisation as a simple quantum correlator to investigate. However any element of the density matrix, and other quantum correlators may be considered, such as the FWM polarisation [44] or populations, which has already been done in [79]. The tensor multiplication scheme used in [43–45, 79] and detailed in Chapter 3 is represented by (relabelling the indices for clarity):

$$F^{(s+1)}_{pi_L\ldots i_2} = \sum_{i_1}^{J} \mathcal{G}_{pi_L\ldots i_1} F^{(s)}_{i_L\ldots i_1}\,, \tag{5.3.1}$$

where $\mathcal{G}$ is known as the propagator and $F^{(s)}$ is the full influence functional, and Fig. 5.1 shows the path segments contained in the tensors. The role of $\mathcal{G}$ is to propagate the system forward in time, taking the tensor $F^{(s)}$ to $F^{(s+1)}$, where F contains all correlations contained within the memory time. F captures how past states influence the present dynamics, incorporating non-Markovian effects. The number of correlations, or time steps, included in the F tensor is also referred to as the number of neighbours, L, with Fig. 5.1 depicting 4 neighbours. Each index in the tensor can have J possible values, for example, in a QD-QD-cavity system, *Case B*, $J = 0, 1, 2$, where 1 or 2 corresponds to the excitonic channel in QD 1 or 2, respectively, and 0 represents the cavity channel. At any time step n within the memory kernel, the excitation can transfer between these components, meaning that i_n evolves dynamically as the system oscillates between QD 1, QD 2, and the cavity. In Fig. 5.1, $\mathcal{G}$ shows a specific case of two-time correlations. This is a consequence of the assumption that the system-bath coupling is bilinear, in which case all higher-order correlation functions can be expressed in terms of the two-time correlations and $\mathcal{G}$ is given by

$$\mathcal{G}_{p\ldots i_1} = M_{i_2 i_1} e^{\mathcal{K}_{i_1 i_1}(0)+2\mathcal{K}_{i_2 i_1}(1)+2\mathcal{K}_{i_3 i_1}(2)+\cdots+2\mathcal{K}_{pi_1}(L)}, \tag{5.3.2}$$

where $\hat{M}$ is defined in Eq. (3.3.3), and $\mathcal{K}$ denotes a cumulant arising from the application of linked cluster expansion and defined in Eq. (3.3.19), with full details contained in Chapter 3. Note that the cumulants contain two indices, $i_n i_m$, describing the two-time correlations between two time points t_n and t_m. Finally, the

linear polarisation is given by Eq.(3.3.34), but rewritten here for convenience:

$$\mathrm{P}_{jk}(t) = e^{\mathcal{K}_{jj}(0)} F^{(N)}_{0\ldots0j}\,. \tag{5.3.3}$$

The subscripts $0\ldots0$ represent the indices can be placed into the cavity channel at the given time steps, but more generally this can be any channel uncoupled to phonons, such as the absolute ground state of the system. As the number of time steps within the memory kernel increases (increasing neighbours), the tensors in Eq. (5.3.1) grow exponentially in size. The exponential growth limits the number of correlations that can be considered, due to computational limitations. As a consequence there are problems in achieving convergence for the following scenarios: 1) When the system has long phonon memory times, 2) when there is a large number of channels J, or 3) in strong coupling regimes where the dynamics exhibit rapid oscillations.

5.4 Optimisation scheme

As a simple example, we demonstrate the optimisation scheme in *Case C*: The linear polarisation in a QD-cavity system. Already studied using a full tensor-multiplication scheme in [43], this system requires two basis states ($J = 0, 1$) such that $i_n = 0\,(1)$ indicates the system is in the cavity (exciton) state at time step n. We write the equations for a general number of neighbours, i.e. the LN approach, but the figures will use only 4 neighbours ($L = 4$) as a simpler example to ease understanding.

The core principle of the optimisation scheme focuses on mapping the tensors in Eq. (5.3.1), in particular the full influence functional F and the propagator $\mathcal{G}$, into two matrices and then performing an SVD at each time step to truncate the size by filtering out contributions below a desired threshold value. Let us consider the first time step, after excitation in channel k at $t = 0$. Since it is only the first time step, the full influence functional tensor can be populated by only $M_{i_1 k}$, and then mapped to a matrix $\mathcal{F}_{nm}$. The full influence functional is populated by only

two values of M_{i_1k}: M_{0k} or M_{1k}. This is because after excitation in channel k at $t = 0$, one further time step introduces index i_1, which has two possible paths of evolution, $i_1 = 0$ and $i_1 = 1$. Typically in other methods, such as Ref.32, there is a growth phase in the early times, where each new time step introduces a new index to the tensor, up until the full memory kernel has been formed. Beyond this point, the tensor has a fixed number of indices, however, here we begin with the full rank tensor as a placeholder for subsequent propagation. The influence functional tensor, populated with the initial dynamics and remapped into a matrix is:

$$F^{(1)}_{i_L \ldots i_1} = M_{i_1 k} = \mathcal{F}_{nm}, \tag{5.4.1}$$

Fig. 5.2 depicts the $L = 4$ influence functional F remapped to a matrix $\mathcal{F}_{nm}$. In $\mathcal{F}_{nm}$, the columns take into consideration the possible values of the indices $(i_{\frac{L}{2}} \ldots i_1)$, and the rows add $(i_L \ldots i_{\frac{L}{2}+1})$ The linear polarisation in the QD-cavity

(i_4, i_3) ↓ \ (i_2, i_1) →	00	01	10	11
00	M_{0k}	M_{1k}	M_{0k}	M_{1k}
01	M_{0k}	M_{1k}	M_{0k}	M_{1k}
10	M_{0k}	M_{1k}	M_{0k}	M_{1k}
11	M_{0k}	M_{1k}	M_{0k}	M_{1k}

Figure 5.2: The tensor $F^{(1)}_{i_4 i_3 i_2 i_1}$ mapped onto a matrix $\mathcal{F}_{nm}$, the columns correspond to the possible values of (i_2, i_1) and the rows (i_4, i_3).

system only has the possible index options $i_n = 0$ or 1, for the $L/2$ indices associated with each of the two matrices. Therefore we generate all possible index configurations by enumerating all tuples $(i_{\frac{L}{2}}, \ldots, i_1)$, where each index i_n independently takes values 0 or 1. This results in $2^{L/2}$ possible configurations to take into account. Each configuration represents a possible path of the system as it evolves over the time steps. For $L = 4$, the configurations for each pair of indices (i_2, i_1) and (i_4, i_3) are simply {00,01,10,11}. Thus, the dimensions of the mapped matrix $\mathcal{F}_{nm}$ are $n_{\max}$,$m_{\max} = 2^{L/2}$, in general. However, $\mathcal{F}_{nm}$ contains the same number of elements as the original tensor F, and therefore presently provides no memory

storage reduction. To remedy this, in order to avoid constructing large tensors in the first instance, $\mathcal{F}_{nm}$ can be analytically expressed in SVD form. In general, this is always possible to do, and is given by:

$$\mathcal{F}_{nm} = U_{n0}\,\Lambda_0\,V_{0m}, \tag{5.4.2}$$

with $U_{n0} = 1$, $\Lambda_0 = 1$ and $V_{0m} = M_{i_1 k}$. Fig. 5.3 shows the matrix $\mathcal{F}_{nm}$ in SVD form. This reduces the total number of elements from 2^L to $\approx 2^{(L/2)+1}$, having a significant impact at larger L, approximately doubling the amount of neighbours achievable. As the matrix has now been represented in SVD form, we define a column vector U which takes into account the indices $(i_L \ldots i_{\frac{L}{2}+1})$ and the row vector, V, taking into account indices $(i_{\frac{L}{2}} \ldots i_1)$.

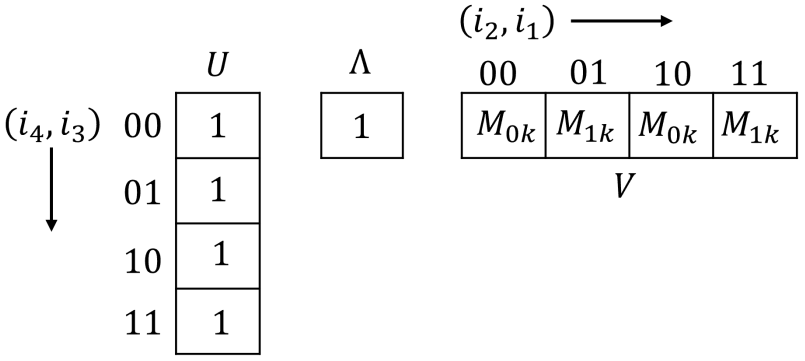

Figure 5.3: The matrix $\mathcal{F}_{nm}$ in Fig. 5.2, expressed in SVD form.

For further time steps, the exciton-phonon coupling has to be considered, which is taken in to account via the propagator $\mathcal{G}$ in Eq. (5.3.1). $\mathcal{G}$ is successively applied to propagate the system forward in time, summing over the first index, i_1, as seen in Eq. (5.3.1).

Although the propagator Eq. (5.3.2) is in the form of a tensor, the two-time correlations can be expressed as 2×2 matrices in the following way

$$\begin{aligned} Q^{(r)}_{i_{r+1}\,i_1} &= \exp\left\{2\mathcal{K}_{i_{r+1}\,i_1}(r)\right\} && \text{for } 1 < r \leq L \\ Q^{(1)}_{i_2\,i_1} &= M_{i_2 i_1} \exp\left\{\mathcal{K}_{i_1 i_1}(0)\right\} \exp\left\{2\mathcal{K}_{i_2 i_1}(1)\right\}\,, && \end{aligned} \tag{5.4.3}$$

where the superscript denotes the time step difference between any index (not

including i_1) in the memory kernel and i_1, i.e. the time step difference between the indices within each pair correlation. For example, considering the indices i_3 and i_1, the correlations are between time points t_3 and t_1 in the memory kernel, thus the Q matrix describing these correlations are given by the matrix $Q^{(2)}_{i_3 i_1}$. The recursive relation Eq. (5.3.1), can then be re-expressed as

$$F^{(s=2)}_{p\, i_L \ldots i_2} = \sum_{i_1=0,1} Q^{(L)}_{p\, i_1} Q^{(L-1)}_{i_L i_1} \ldots Q^{(2)}_{i_3 i_1} Q^{(1)}_{i_2 i_1} \mathcal{F}_{nm}. \tag{5.4.4}$$

The product of the Q matrices must be applied to the appropriate elements of $\mathcal{F}_{nm}$, with a summation over index i_1. Since each vector in Fig. 5.3 correspond to specific indices, only Q matrices which consider pair correlations between those indices should be applied to that vector. In other words, the propagator matrix Q_{i_2,i_1} is applied to the right vector, and matrices Q_{i_3,i_1} and Q_{i_4,i_1} applied to the left vector. Note that each Q matrix describes the correlations between any index in the kernel and i_1, but the left vector does not contain any information about i_1, therefore modifications must be made to account for this before the summation over i_1 can be performed. Similarly, in the left and right vectors, there is no information about the value of index p in the propagator $\mathcal{G}$. Firstly, in an attempt to perform the summation over i_1, we begin by separating $\mathcal{F}_{nm}$ into $i_1 = 0$ and $i_1 = 1$ components,

$$\begin{aligned} \mathcal{F}^{(i_1=0)}_{nm'} &= \textstyle\sum_k U_{nk}\, \Lambda_k V^{(i_1=0)}_{km'} \\ \mathcal{F}^{(i_1=1)}_{nm'} &= \textstyle\sum_k U_{nk}\, \Lambda_k V^{(i_1=1)}_{km'}\,, \end{aligned} \tag{5.4.5}$$

where $\mathcal{F}_{nm} = \mathcal{F}^{(i_1=0)}_{nm'}$ if $i_1 = 0$ and $\mathcal{F}_{nm} = \mathcal{F}^{(i_1=1)}_{nm'}$ if $i_1 = 1$, with $m'_{\max} = m_{\max}/2$. With reference to Fig. 5.3, we see that the right vector V_{km} contains information about the index i_1, which is the cause of $V_{km} = V^{(i_1=0)}_{km'}$ and $V_{km} = V^{(i_1=1)}_{km'}$ having the reduced dimensionality m'. However, the left vector U_{nk} has no dependence on i_1, and therefore has the same dimensionality in both cases for $i_1 = 0$ or 1. At this point, the product of Q matrices can be applied to U_{nk} and $V_{km'}$. The Q matrices which introduce correlations between indices contained within U_{nk}, i.e. correlations between $i_L \ldots i_{\frac{L}{2}+1}$ and i_1 will be multiplied into U_{nk}. Note that since

U contains no information about i_1, both possibilities of $i_1 = 0$ and $i_1 = 1$ must be taken into account. The Q matrices which introduce correlations between indices $i_{\frac{L}{2}} \dots i_2$ and i_1 are multiplied with $V_{km'}$. However, the propagator introduces the additional index p, and we choose to apply $Q^{(L)}_{pi_1}$ onto the $V_{km'}$ matrix. As there is no information about index p contained within either left or right vectors, both possibilities of $p = 0$ and 1 must be taken into account, similar to the lack of information about index i_1 in the vector $U(nk)$. We then obtain two new matrices,

$$\begin{aligned} \tilde{U}^{(i_1=0)}_{nk} &= Q^{(L-1)}_{i_L 0} \dots Q^{(\frac{L}{2})}_{i_{\frac{L}{2}+1} 0} U_{nk} && \text{for } i_1 = 0 \\ \tilde{U}^{(i_1=1)}_{nk} &= Q^{(L-1)}_{i_L 1} \dots Q^{(\frac{L}{2})}_{i_{\frac{L}{2}+1} 1} U_{nk} && \text{for } i_1 = 1\,. \end{aligned} \tag{5.4.6}$$

Similarly,

$$\begin{aligned} \tilde{V}^{(i_1=0,p)}_{km'} &= Q^{(L)}_{p0} Q^{(\frac{L}{2}-1)}_{i_{\frac{L}{2}} 0} \dots Q^{(1)}_{i_2 0} V^{(i_1=0)}_{km'} && \text{for } i_1 = 0 \\ \tilde{V}^{(i_1=1,p)}_{km'} &= Q^{(L)}_{p1} Q^{(\frac{L}{2}-1)}_{i_{\frac{L}{2}} 1} \dots Q^{(1)}_{i_2 1} V^{(i_1=1)}_{km'} && \text{for } i_1 = 1\,, \end{aligned} \tag{5.4.7}$$

with $p = 0$ or $p = 1$, due to the introduction of the new index p in Eq. (5.4.4), which is necessary for the forward propagation of the system in time. As an example on how to apply the Q matrices appropriately to the vector elements, consider the propagator matrix $Q^{(1)}_{i_2 i_1}$, we can then apply the matrix element $Q^{(1)}_{00}$ to elements in $V^{(i_1=0)}_{km'}$ that correspond to $i_L = 0$, and $Q^{(1)}_{01}$ to the elements corresponding to $i_L = 0$ in $V^{(i_1=1)}_{km'}$, and so on. Now, once all propagator matrices have been applied,

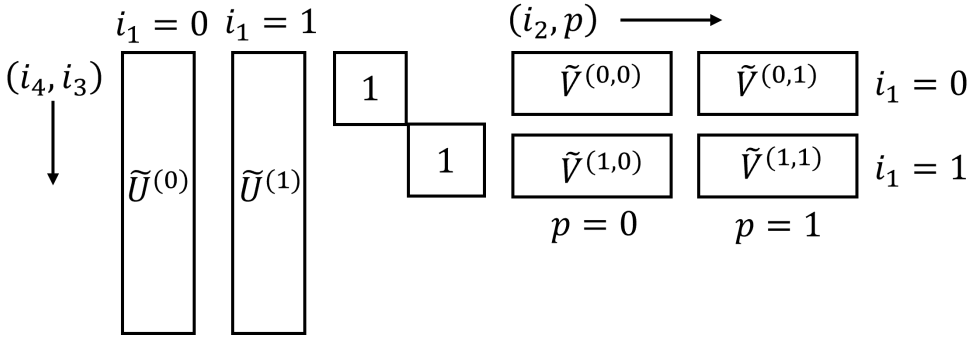

Figure 5.4: The tensor $F^{(s=2)}_{p i_L \dots i_2}$ mapped to a matrix $\tilde{\mathcal{F}}_{nm}$. The vectors from the initial time step, U_{nk} and V_{km}, have been split through applying the Q_{ii_1} matrix elements for $i_1 = 0$ and $i_1 = 1$, with V being further split through the extra index p, with $p = 0$ and $p = 1$.

let us denote $\tilde{\mathcal{F}}^{(p)}_{nm}$ representing $F^{(2)}_{p i_L \dots i_2}$ in Eq. (5.4.4) for any p as

$$\tilde{\mathcal{F}}^{(p)}_{nm} = \sum_k \left(\tilde{U}^{(0)}_{nk} \Lambda_k \tilde{V}^{(0,p)}_{km'} + \tilde{U}^{(1)}_{nk} \Lambda_k \tilde{V}^{(1,p)}_{km'} \right), \tag{5.4.8}$$

where the tilde notation denotes that the Q matrices have been applied, propagating the system forward in time for this iteration. The new propagated matrix $\tilde{\mathcal{F}}_{nm}$, now at step 2 ($s = 2$) is shown diagrammatically in Fig. 5.4. In Fig. 5.4, U and V have been split due to the summation over i_1, according to Eqs. (5.4.6) and (5.4.7), and the Q matrices in Eq. (5.4.3) have been applied, further splitting V due to the introduction of a new index p in the propagator. To calculate the

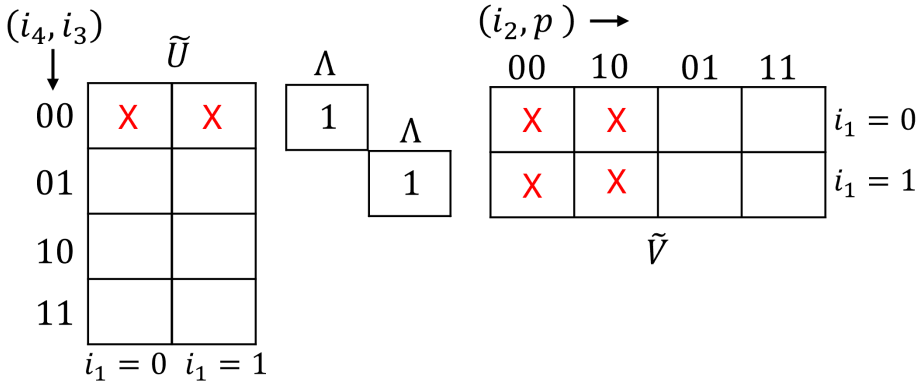

Figure 5.5: The tensor $F^{(s=2)}_{p i_L \dots i_2}$ mapped to a matrix $\tilde{\mathcal{F}}_{nm}$, as in Fig. 5.4 but here showing $\tilde{U}$ as a 4×2 matrix with the first and second columns being $\tilde{U}^{(0)}$ and $\tilde{U}^{(1)}$, respectively. The first (second) row of $\tilde{V}$ consists of $\tilde{V}^{(i_1=0,p=0)}$ and $\tilde{V}^{(i_1=0,p=1)}$ ($\tilde{V}^{(i_1=1,p=0)}$ and $\tilde{V}^{(i_1=1,p=1)}$). The red crosses indicate which matrix elements should be multiplied together in order to go from $F^{(N)}_{p i_4 i_3 i_2}$ to the specific realisation $F^{(N)}_{0\dots0j}$ required to compute the polarisation, as in Eq. (5.3.3).

polarisation, given in Eq. (5.3.3), we take the specific realisation $F_{p\dots i_3 i_2} \rightarrow F_{0\dots0j}$, where j is the measurement channel at any time step. Fig. 5.5 shows the matrices in Fig. 5.4 more explicitly, with the red crosses indicating which elements should be multiplied together for this specific realisation. This matrix multiplication is effectively summation over i_1, as required, and the measurement channel, j, is selected by choosing $i_2 = j = 0, 1$. The first (second) row of $\tilde{V}$ consists of $\tilde{V}^{(i_1=0,p=0)}$ and $\tilde{V}^{(i_1=0,p=1)}$ ($\tilde{V}^{(i_1=1,p=0)}$ and $\tilde{V}^{(i_1=1,p=1)}$). Note that this particular arrangement causes the rows in $\tilde{V}$ to be split with the possible values of i_1, and the i_1 value being constant across the corresponding column. The consequence of

this arrangement is that the configuration ordering changes, since p is now varying across columns, just as i_1 was in the initial vectors (see Fig. 5.3). Therefore, the realisation $F^{(s=2)}_{0\ldots0}$ ($F^{(s=2)}_{0\ldots01}$) is obtained through standard matrix multiplication with the elements in first row of $\tilde{U}$ with the column corresponding to the configuration $i_{\frac{L}{2}}\ldots i_2 p = \{0\ldots0\}$ ($\{0\ldots10\}$) column in $\tilde{V}$, corresponding to the cavity (exciton) observation channel.

In the recursion relation Eq. (5.4.4), $F^{(s=2)}_{p\,i_L\ldots i_2}$ must become the new $F^{(s=2)}_{i_L\ldots i_1}$ for the next time step, and we must therefore remap the indices. As an example, for $L = 4$, $(i_4, i_3) \to (i_3, i_2)$ becomes associated with $\tilde{U}$ and $(i_2, p) \to (i_1, i_4)$ associated with $\tilde{V}$. After each time step, we redefine $\tilde{U}$ ($\tilde{V}$) as U (V) without the tilde, as seen in Fig. 5.6, which also shows the new indices that are associated with the matrices. This indicates that we must again split the matrices due to the possibility of $i_1 = 0$ or $i_1 = 1$, and the subsequent application of the Q matrix elements to propagate the system must occur. In each successive time step, the indices will cycle, but once the index i_1 becomes associated with U (after $L/2$ steps), the original index ordering has been restored but on opposite matrices. That is, for $L = 4$, (i_2, i_1) is instead associated with U, and (i_4, i_3) with V. Therefore, once this occurs, it's computationally simpler to transpose all the matrices and redefine, such that $U = V^T$ and $V = U^T$, allowing us to return to repeat the same procedure outlined in this section. To summarise, after $L/2$ time steps the matrices should be transposed in order to return the indices to their original positions, i.e. $(i_{L/2}\ldots i_1)$ associated with V, we call this the start of the cycle.

It is clear that through the splitting due to $i_1 = 0$ and 1 after each time step, the size of U matrix doubles in size relative to the previous step, and through the splitting due to $p = 0$ and 1, V also doubles in size. Thus, every subsequent $\mathcal{F}$ doubles in size, however this can be optimised, reducing the sizes, by performing an SVD on the matrices. For instance, we can SVD V, as shown in Fig. 5.7, where Λ_1 which contains the significant values has a smaller size due to the threshold condition that if $|\lambda_k| < \epsilon$ then $\lambda_k = 0$, truncating the SVD matrices. The threshold

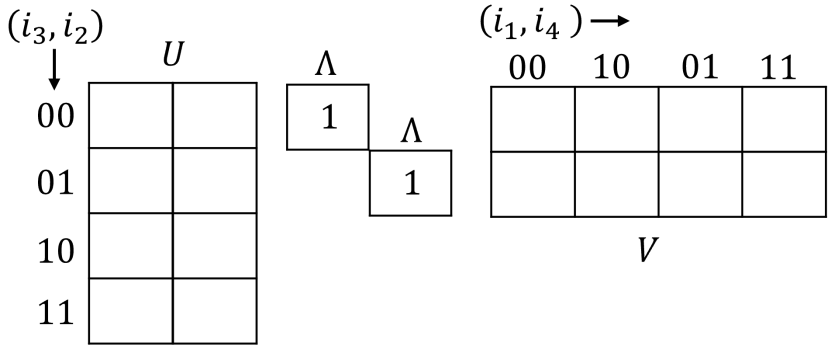

Figure 5.6: The tensor $F^{(s=2)}_{i_L \ldots i_1}$ mapped to a matrix $\mathcal{F}_{nm}$. This is the starting point of the next time step, the subsequent application of the Q matrices and splitting due to $i_1 = 0, 1$ and $p = 0, 1$ will be applied here to propagate the system.

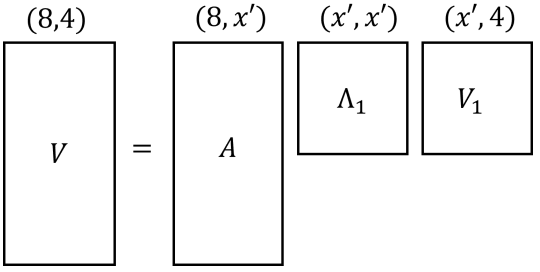

Figure 5.7: SVD applied on V after the third time step, where there are now 8 rows. There is still the 4 columns since the number of configurations for a given number of neighbours is fixed. By applying SVD with a threshold value, the truncated dimension becomes x'. V_1 is the new truncated V used for further propagation.

ϵ may be changed based on the desired accuracy of the calculation, the results in this paper use $\epsilon = \lambda_{\max} \times 10^{-8}$, where $\lambda_{\max}$ is the largest value contained in Λ_1. As seen in Fig. 5.7, considering for illustration V, which is initially a 1×4 matrix at the first time step, but has increased to an 8×4 matrix after three iterations (for $L = 4$, but would be an $8 \times 2^{L/2}$ in general). Then, if after applying the threshold only x' significant values remain, A is a $(8, x')$ matrix, Λ_1 is a (x', x') matrix and V_1 is a $(x', 4)$ matrix. Initially this appears to increase the number of required elements, however A and Λ_1 can be multiplied into U, which is a $(4, 8)$ matrix, and through just matrix multiplication, the size of U is truncated to a matrix U_1 of size $(4, x')$. Thus, the matrices of reduced dimension, V_1 and U_1 in Figs.5.7 and 5.8, respectively, are used as the new V and U for the proceeding time step. If the truncation is insufficient after one SVD, the SVD can be applied again onto U, which was initially only multiplied with the products from applying

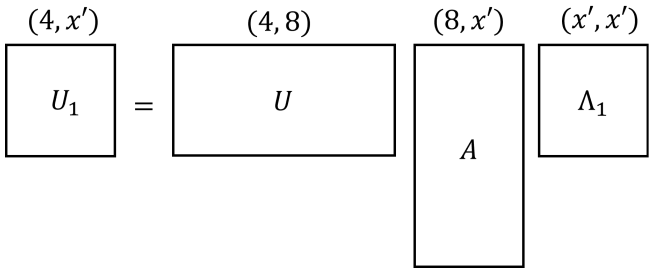

Figure 5.8: A and Λ_1, which are products from performing an SVD on V, are multiplied into U, which automatically truncates the dimensions without performing any further SVDs. U_1 is the new U used for further propagation.

SVD on V, and then multiply the products from applying SVD on U back into V. Effectively, there is an SVD sweeping back and forth to truncate the sizes. These truncated matrices are then used as the starting U and V for the following time step, with the SVD procedure applied every time step to keep the matrices from growing exponentially.

Computationally the procedure is straightforward. We start with a tensor which has a number of indices equal to the amount of time steps within the memory kernel (or neighbours), L. We then assign half the indices to a matrix U, and the other half to a matrix V, where each element corresponds to a specific path, or configuration, of the indices. Due to the exponential form of the propagator, it can be decomposed into matrices Q, defined in Eq. (5.4.3), which describe the correlations between two time points. The Q matrix elements can be multiplied into U and V, propagating the system. Then, via matrix multiplication of the desired rows and columns, a specific realisation is calculated and any physical observable can be found. The exponential scaling of the matrix sizes (doubling at each time step) is then handled by performing an SVD on the matrices to keep only contributions above a chosen threshold value.

5.4.1 Generalisation to J-dimensional density matrix vectors

More generally for a system and correlator which can be fully described by J system states, The dimensions of the mapped matrix, $n_{\max}$ and $m_{\max}$, are dependent

on the number of neighbours, L and J, i.e. $n_{\max}, m_{\max} = J^{L/2}$. In other words, there are more configurations of the indices when there are more possible system states. They are generated by enumerating all tuples $(i_{\frac{L}{2}}, \ldots, i_1)$, where each index i_k independently takes values in the finite set $\{0, 1, \ldots, J\}$. This yields $(J+1)^{\frac{L}{2}}$ distinct configurations.

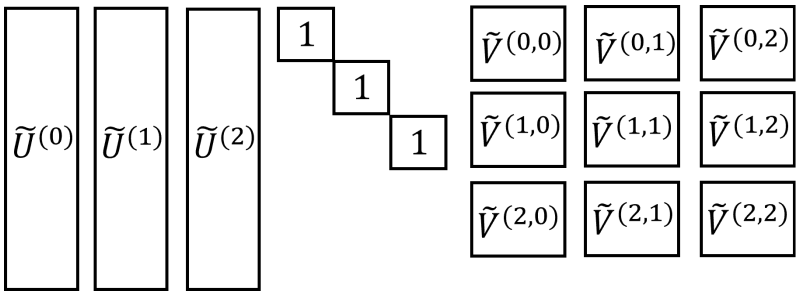

Figure 5.9: The tensor $F^{(s=2)}_{p i_L \ldots i_2}$ mapped to a matrix $\tilde{\mathcal{F}}_{nm}$ for $J = 3$, as in *Case B* for the QD-QD-cavity system, the matrices U has been duplicated three times to account for all possible values of $i_1 = 0, 1, 2$, since no knowledge of i_1 is contained within U. V has been split into three blocks corresponding to the values of i_1, as the value of i_1 is known for each element in V. However, each block of the split V is then duplicated three times due to the propagation index $p = 0, 1, 2$.

At time step s, the tensor $F^{(s)}_{i_L \ldots i_1}$ (where $i = 0, 1, \ldots J-1$) is represented by a standard matrix $\mathcal{F}_{nm}$, which is split into two matrices U and V. As before, the indices are assigned to the matrices U and V, however, due to the extra possible states of i_1, the matrix V_{km} is split into J matrices, $V_{km} \to V^{(i_1)}_{km'}$, each corresponding to a specific i_1 value. $V_{km'}$ is a J times smaller matrix than V_{km} since the i_1 values are known, as this index is associated with V. The propagation index p also has J possible values, and each $V^{(i_1)}_{km'}$ is duplicated to account for all possible p values. Similarly, U_{nk} is duplicated J times, with each corresponding to a possible i_1 value, as there is no information about index i_1 contained within U. Fig. 5.9 shows the specific case of $J = 3$, which may represent *Case B*, the linear polarisation in a QD-QD-cavity system. The Q matrices defined in Eq. (5.4.3) are applied into the matrix elements of V and U as before, and there is a summation over i_1, propagating the system from $F^{(s)}$ to $F^{(s+1)}$. We have then, for the first

application of the Q matrices

$$\begin{aligned}\tilde{U}^{(i_1)}_{nk} &= Q^{(L-1)}_{i_L i_1} \dots Q^{(L/2)}_{i_{L/2+1}\, i_1} U_{nk} \\ \tilde{V}^{(i_1,p)}_{km'} &= Q^{(L)}_{p i_1} Q^{(\frac{L}{2}-1)}_{i_{L/2} i_1} \dots Q^{(1)}_{i_2 i_1} V^{(i_1)}_{km'}.\end{aligned} \tag{5.4.9}$$

Denoting the propagated full influence functional tensor $F^{(2)}_{p i_L \dots i_2}$ as the mapped matrix $\tilde{\mathcal{F}}_{nm}$, which is given by

$$\tilde{\mathcal{F}}^{(p)}_{nm} = \sum_{i_1} \sum_{k} \tilde{U}^{(i_1)}_{nk} \Lambda_k \tilde{V}^{(i_1,p)}_{km'}, \tag{5.4.10}$$

as before, but with $i_1, p = 0, 1, \dots J-1$. For subsequent time steps the indices associated with V and U are remapped due to $F^{(s+1)}_{p i_L \dots i_2}$ becoming the new $F^{(s)}_{i_L \dots i_1}$ in the iterative procedure given by Eq. (5.3.1). As a consequence, the Q matrices which are applied onto U and V in Eq. (5.4.9), which shows the specific case for the first iteration, also change. In other words, the Q matrices which contain correlations between the indices which are contained within U and V are used.

5.5 Verification

Fig. 5.10 illustrates the accuracy of our optimisation scheme by calculating the linear optical polarisation $\mathrm{P}_{11}(t)$ of an isotropic QD coupled to a micro-cavity with coupling strength $g = 100\mu$eV. We compare the results from the original full tensor multiplication scheme [43], the optimised calculation, and the well-known TEMPO approach [32] using the same number of neighbours, $L = 26$, in each case. An SVD threshold of $\epsilon = 10^{-8}$ is used in the optimised and TEMPO calculations. The inset of Fig. 5.10 demonstrates the error between the full well-converged original calculation and the optimisation (blue) and TEMPO (green). The inset shows the close agreement between the optimised scheme and the original full tensor method confirming the validity of our approach, while the comparison with TEMPO serves as an additional point of reference. There is a large benefit to computational time, taking roughly 1300 seconds using the original approach, compared with only 30 seconds using the optimisation scheme, for the same number of neighbours. Note

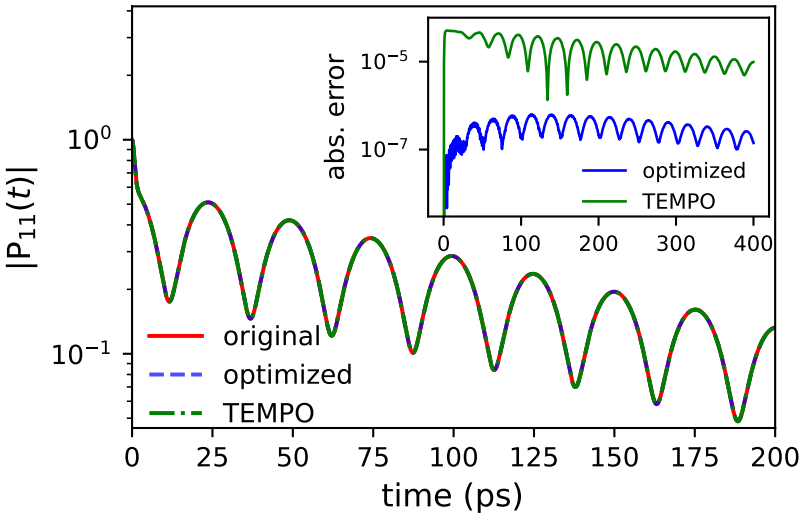

Figure 5.10: The linear optical polarisation, $|P_{11}(t)|$, for an isotropic QD of confinement length $l = 3.3\,\text{nm}$ coupled to a micro-cavity with coupling strength $g = 100\,\mu\text{eV}$ at zero detuning, with excitation and measurement in the QD. The calculation using the original tensor multiplication scheme [43] (shown in red) is compared with the optimised method (blue), and TEMPO (green). All calculations use the number of neighbours $L = 26$, with the optimised and TEMPO methods using an SVD threshold of $\epsilon = \lambda_{\text{max}} \times 10^{-8}$. Inset: Absolute error between the full calculation and the optimisation and TEMPO. The phonon bath temperature is $T = 50\,\text{K}$ and the rest of the parameters are found in Table 2.1.

that in Fig. 5.10, all calculations used the same number of neighbours for a direct comparison. However, the maximum achievable neighbours in the original full calculation for this QD-cavity system is $L = 26$ for a desktop PC of 16GB RAM, whereas the optimised case has approximately $L = 50$.

5.6 Extrapolation

As detailed in Chapter 2, the strong coupling between the exciton and cavity forms two polariton branches, and the oscillatory behaviour in Fig. 5.10 is explained by the coherent exchange of energy between the polariton states. The energy levels of the states are separated by the Rabi splitting, which determines the beat frequency in $|P_{11}(t)|$. This frequency physically represents the exchange of quantum information between the QD and the cavity. The temporal decay of the linear polarisation expresses the decoherence in this system as a consequence of the interaction of the QD with the bath. This decoherence is due to phonon-

assisted transitions between the upper ($|+\rangle$) and lower ($|-\rangle$) polariton states (see the equivalent discussion regarding the hybridised states in Chapter 4).

Using this picture, we have applied to the long-time dynamics of $P_{11}(t)$ a biexponential fit of the form

$$\mathrm{P}_{11}^{\mathrm{fit}}(t) = \sum_j C_j e^{-i\omega_j t}\,, \tag{5.6.1}$$

extracting the complex amplitudes C_j, energies Re ω_j, and dephasing rates $\Gamma_j = -\,\mathrm{Im}\;\omega_j$ of the phonon-dressed polariton states, as discussed in Sec.4.2. These extracted parameters follow a power law dependence on the number of neighbours L. Therefore, one can calculate the linear optical polarisation for a given number of neighbours, apply a fit to the long time data, extract the fit parameters and then apply a power-law fit to these parameters. The resulting parameters across the range of neighbours are used to perform a power-law extrapolation, estimating the exact value which corresponds to $L = \infty$.

As an example, consider the parameters corresponding to the dephasing rates, $\Gamma(L)$ extracted across a range of neighbours, where the convergence of $\Gamma(L)$ to the exact ($L = \infty$) value is assumed to follow a power law model, given by

$$\Gamma(L) = \Gamma(\infty) + CL^{-\beta}. \tag{5.6.2}$$

Figure 5.11 shows the $\Gamma(L)$ calculated values (blue crosses) in the QD-cavity system, with the power law model applied (red curve), and the extrapolated $\Gamma(\infty)$ is shown as a red dashed line. The value of $\Gamma(\infty)$ is estimated for the values of $\Gamma(L)$ shown in Fig. 5.11 by minimising the root mean square deviation from the power law Eq. (5.6.2) for $\beta = 2$. Fig. 5.11 also demonstrates the necessity of the extrapolation, since optimisation alone may not be well converged in some cases. However, the extra data provided by the optimisation by achieving more neighbours allows for an accurate usage of the extrapolation. In fact, in some systems with very long memory times, such as in extended quantum systems, the extrapo-

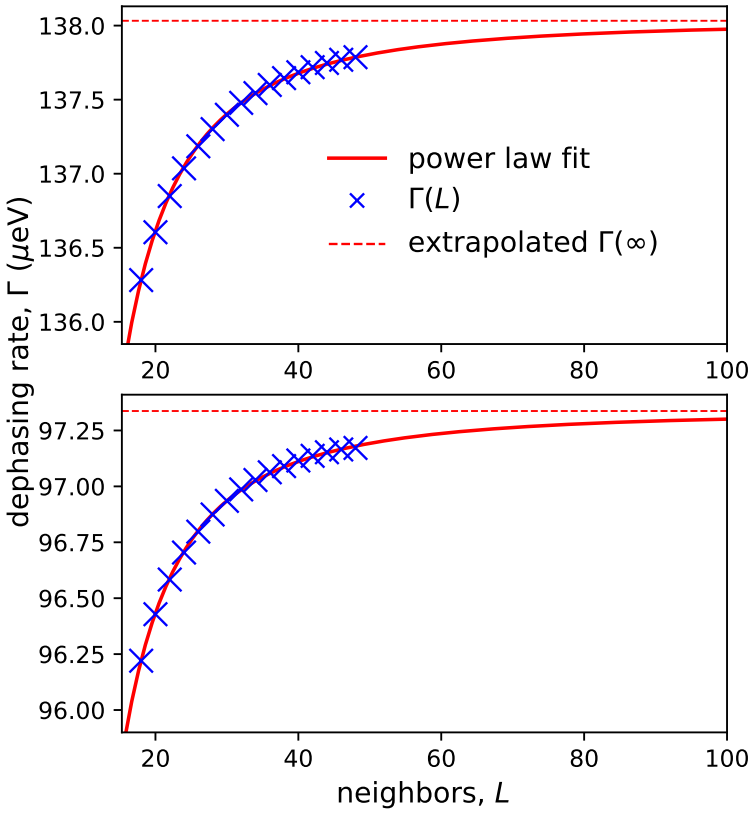

Figure 5.11: Power law fit applied to the $\Gamma_+(L)$ ($\Gamma_-(L)$) values across a range of neighbours, L, for $g = 600\,\mu$eV is shown in the upper (lower) figure. The blue crosses are the extracted $\Gamma(L)$ values, the red curve is the power law model with $\beta = 2$, and the red horizontal dashed line is the estimated value of $\Gamma(\infty)$. The rest of the parameters are as in Fig. 5.10.

lation is not possible at all with the original technique and requires the data from the optimisation scheme.

5.7 Illustrations

The optimisation and extrapolation, developed in Secs. 5.4 and 5.6 are applied first in *Case C*, the QD-cavity system. Firstly we demonstrate the agreement, comparing the original full tensor-multiplication scheme [43] to the optimised calculation using more neighbours (greater accuracy), and subsequent extrapolation in a regime with a moderate QD-cavity coupling strength. Then, we extend the calculation across a range of QD-cavity coupling strengths, going beyond what was computed in [43]. Next, we apply the optimisation and extrapolation to *Case*

B, detailed in Sec. 3.2, for a QD-QD-cavity system. In this system of spatially separated QDs, the necessity of the optimisation and extrapolation is shown when the memory times become very long.

5.7.1 Accessing stronger coupling regimes in the QD-cavity system

Fig. 5.12 shows the linear optical polarisation $\mathrm{P}_{11}(t)$ of an isotropic QD coupled to a micro-cavity with coupling strength $g = 600\mu$eV at zero detuning. The data is

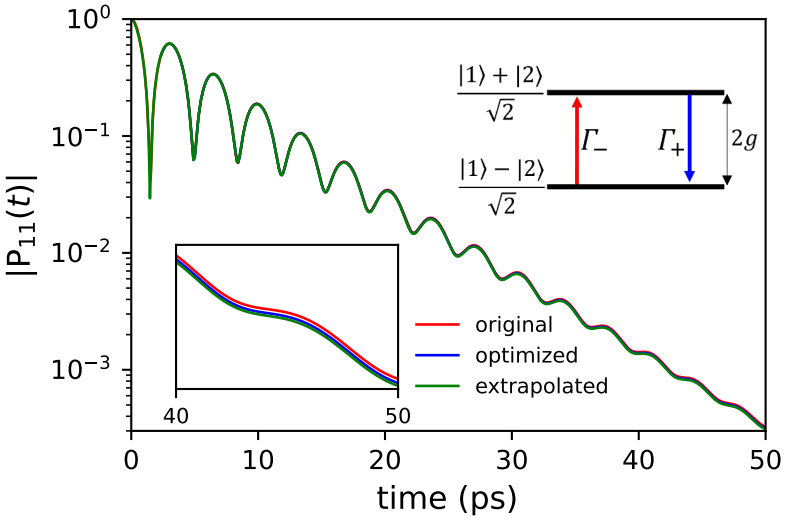

Figure 5.12: The linear optical polarisation, $|\mathrm{P}_{11}(t)|$, for an isotropic QD of confinement length $l = 3.3\,$nm coupled to a micro-cavity with coupling strength $g = 600\,\mu$eV at zero detuning, with excitation and measurement in the QD. The calculation using the original multiplication scheme is shown in red ($L = 26$), the optimised calculation in blue ($L = 48$, SVD threshold $\epsilon = \lambda_{\max} \times \epsilon = 10^{-8}$) and extrapolated calculation in green. Inset: Energy level diagram for the hybridised QD-cavity states $|+\rangle = (|1\rangle + |2\rangle)/\sqrt{2}$ and $|-\rangle = (|1\rangle - |2\rangle)/\sqrt{2}$, with real phonon-assisted transitions (red and blue arrows). The phonon bath parameters are as in Fig. 5.10.

calculated with the original tensor-multiplication scheme, the optimisation and extrapolation. There is good convergence of the original calculation at this coupling strength because the time step Δt, which decreases as the number of neighbours increases, is small enough to resolve the dynamics of the Rabi oscillations. The frequency of the Rabi oscillations at zero detuning is determined by the energy splitting of $2g$ between the polariton states (see inset of Fig. 5.12). Therefore,

as g increases, a smaller time step is required for an accurate calculation. The optimisation and extrapolation thus provides access to larger coupling strengths.

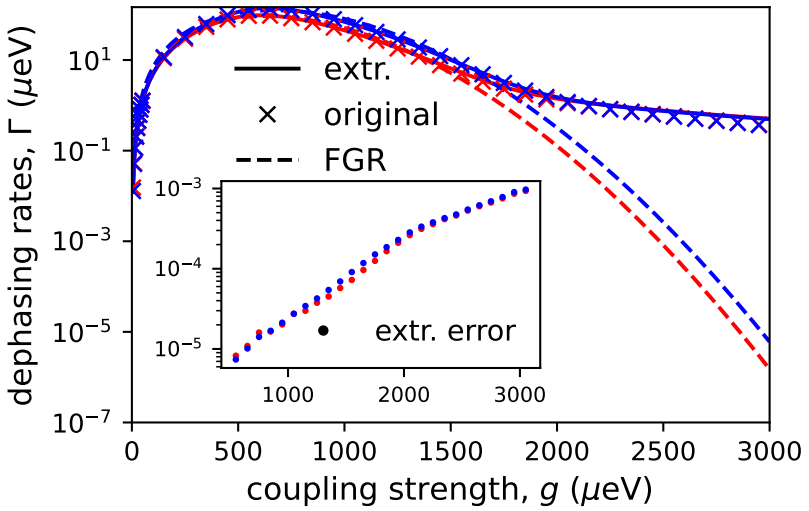

Figure 5.13: Dephasing rates $\Gamma_\pm$ of the hybridised states $|\pm\rangle$ at zero detuning as a function of the QD-cavity coupling strength g, calculated via the optimisation scheme ($L = 48$, SVD threshold $\epsilon = \lambda_{\max} \times \epsilon = 10^{-8}$) and extrapolated (solid lines), via FGR (dashed lines), and the most accurate calculation via the original tensor-multiplication scheme (crosses) for isotropic QDs with a confinement length of $l = 3.3\,\mathrm{nm}$. The inset shows the extrapolation error for both extrapolated dephasing rates. The phonon bath parameters are as in Fig. 5.10.

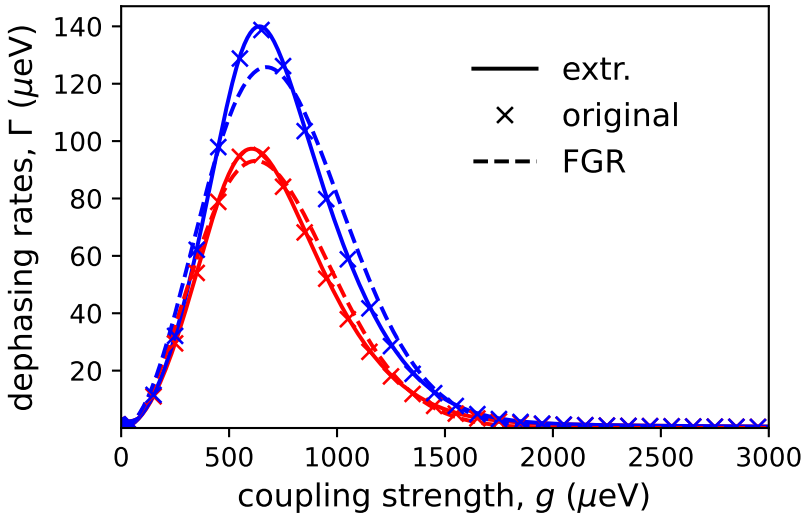

Figure 5.14: As in Fig. 5.13 but with a linear scale.

Fig. 5.13 shows the dephasing rates $\Gamma_\pm$ in the QD-cavity system as a function coupling strength g (see Fig. 5.13 for a linear scale). The optimised and extrapolated data visually align with the original calculation at smaller coupling strengths,

but show a deviation at larger values as expected. Provided that the parameters extracted via the optimisation scheme follow the power law convergence, the extrapolated values are accurate for significantly larger coupling strengths than the original approach [43]. The inset of Fig. 5.13 shows the extrapolated error for each of the extrapolated $\Gamma_{\pm}$ values, where even at $g = 3000\mu\,\mathrm{eV}$ the extrapolated error (10^{-3}) is much less than the difference between the extrapolated and original calculations (10^{-1}). It is worth noting that the discrepancy between FGR and the full calculation at large coupling strengths is likely due to not taking into account virtual transitions, which are significant compared to real transitions at such large coupling strengths [37, 46]. The virtual transitions can be added to the real transitions and taken into account via FGR by using the quadratic coupling model in [37] or a combined approach [100].

5.7.2 Necessity of the optimisation in spatially extended systems

When a spatially extended quantum system interacts with a common environment, the memory time can become very large and its quantum dynamics is difficult to capture accurately. We now use *Case B*, a system of two spatially separated QDs coupled to a microcavity and interacting with a shared phonon bath as illustration.

Fig. 5.15 shows the linear polarisation, $|\mathrm{P}_{11}(t)|$, for a pair of cavity-mediated ($g_1 = g_2 = \bar{g} = 500\,\mu\mathrm{eV}$) coupled isotropic QDs separated by $d = 5\,\mathrm{nm}$. In this case of zero detuning ($\Omega_1 = \Omega_2 = \Omega_C$) and equal QD-cavity couplings, there are three resulting hybridised states, $|+,\pm\rangle = (|1\rangle + |2\rangle)/2 \pm |C\rangle/\sqrt{2}$ and $|-\rangle = (|1\rangle - |2\rangle)/\sqrt{2}$, as depicted in the inset (see [45] and Sec.4.3). To generate the extrapolated data, a triexponential fit is applied to $\mathrm{P}_{11}(t)$ to extract the parameters of these hybridised states. Fig. 5.15 compares the original, optimised and extrapolated calculations, however, the separation of 5 nm is small and does not significantly increase the memory time (see Appendix I). Therefore, we observe a similar and sufficient convergence of the original calculation as in the QD-cavity system in the previous section. Fig. 5.16 shows the same calculation, but instead

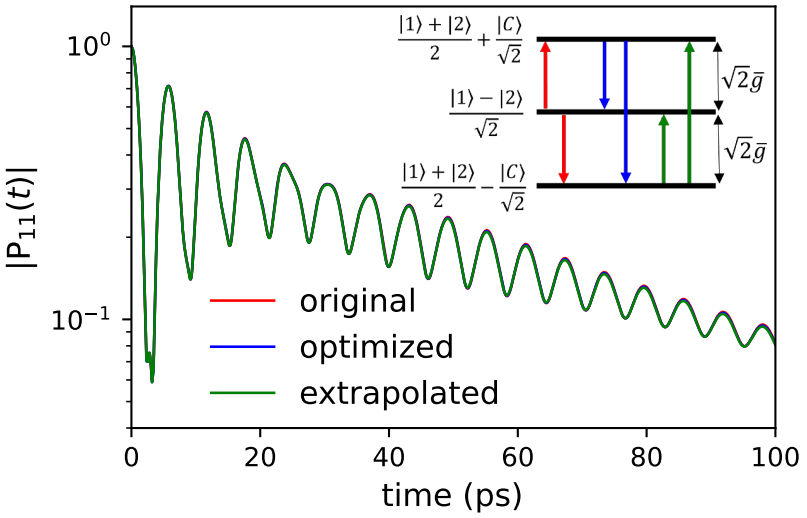

Figure 5.15: The linear polarisation, $|P_{11}(t)|$, for cavity-mediated ($g_1 = g_2 = \bar{g} = 500\,\mu$eV) isotropic QDs with confinement length $l = 3.3\,$nm at zero detuning. The QDs are separated by the distance $d = 5\,$nm, with excitation and measurement in QD 1. The calculation using the full tensor multiplication scheme is shown in red ($L = 16$), the optimised calculation in blue ($L = 30$, SVD threshold $\epsilon = \lambda_{\max} \times 10^{-8}$) and extrapolated calculation in green. Inset: Energy level diagram for the hybridised QD-cavity states $|+,\pm\rangle = (|1\rangle + |2\rangle)/2 \pm |C\rangle/\sqrt{2}$ and $|-\rangle = (|1\rangle - |2\rangle)/\sqrt{2}$, with real phonon-assisted transitions (red, blue and green arrows). The phonon bath temperature is $T = 20\,$K and rest of the phonon bath parameters are found in Table 2.1.

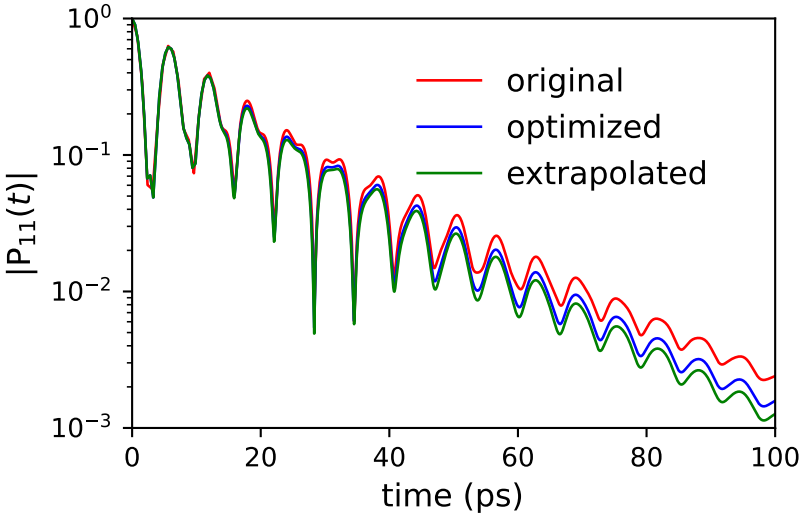

Figure 5.16: As in Fig. 5.15 but with a QD separation of $d = 45\,$nm.

with a separation of $d = 45\,$nm, which displays a clear lack of convergence using the original method. Even the calculation using the optimisation scheme is not very well converged, showing the necessity of the extrapolation. It should be noted

that the extracted parameters do not follow a power-law convergence across all L values, instead, the selected L values must be sufficiently high to enter the regime of power-law convergence. Due to this, the original technique in most regimes of spatially extended systems cannot generate enough data within the power-law convergence regime to provide an extrapolated calculation. Therefore, the optimised calculations are required for the extrapolation.

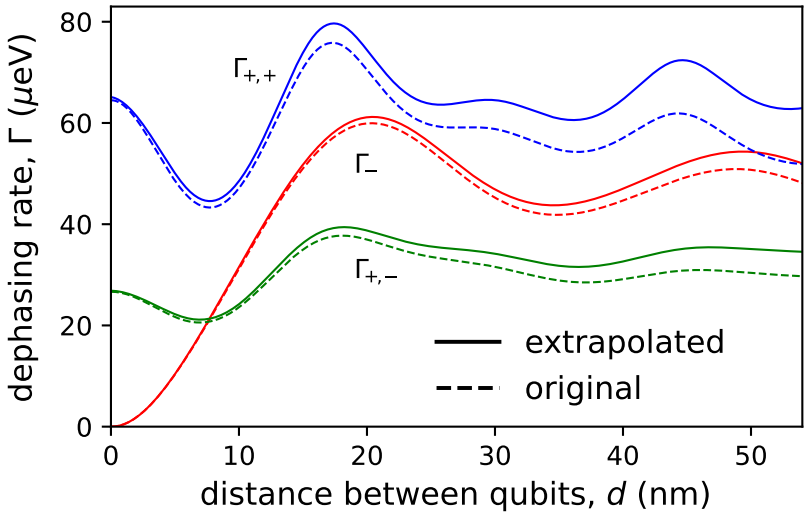

Figure 5.17: Dephasing rates $\Gamma_{+,\pm}$ and Γ_{-} of the hybridised states as a function of d. The extrapolation (solid lines) is compared with the original (dashed lines) for cavity-mediated coupled identical isotropic QDs with interaction strength $g_1 = g_2 = \bar{g} = 500\,\mu$eV, and zero detuning. The phonon bath temperature is $T = 20\,$K and the rest of the parameters are found in Table 2.1.

Fig. 5.17 shows the dephasing rates Γ_j extracted from the fit as functions of the QD separation d. The dephasing rates of the hybridised states $|+,\pm\rangle = (|1\rangle + |2\rangle)/2 \pm |C\rangle/\sqrt{2}$ and $|-\rangle = (|1\rangle - |2\rangle)/\sqrt{2}$ are denoted by $\Gamma_{+,\pm}$ and Γ_{-}, respectively. As the QD separation increases, the memory time increases, and the original calculation gradually becomes increasingly inaccurate, requiring the optimisation and extrapolation to accurately model the system.

5.8 Summary

In this chapter, an optimisation scheme has been developed for path-integral tensor-multiplication schemes and it has been applied to the Trotter decomposition with linked cluster expansion technique. The scheme is demonstrated by applying it to the linear polarisation in a quantum dot-cavity system, although it is applicable for any basis size and any density matrix element, e.g. populations. The scheme approximately doubles the achievable number of neighbouring connections within the tensor network structure, which is significant given the exponential scaling typically associated with tensor multiplication schemes. It should be noted that more memory-efficient representations for the tensors exist; however, the optimisation developed in this thesis enables the usage of an extrapolation scheme not available in other techniques. The increased number of neighbours paired with extrapolation gives access to previously inaccessible regimes, offering better convergence for systems with long memory times. For calculations already well converged using traditional approaches, the optimisation scheme offers greatly improved computational efficiency, shortening calculation times by up to two orders of magnitude.

Chapter 6

Conclusion

In Chapter 2, the theoretical framework was outlined by examining two fundamental models: the JC model describing QD-cavity interactions and the IB model characterising QD-phonon interactions. The JC model revealed how strong coupling between a QD and cavity leads to polariton formation with distinct energy branches separated by the Rabi splitting, and the coherent exchange of energy leads to Rabi oscillations. Meanwhile, the IB model introduced techniques for incorporating phonon effects, highlighting the non-Markovian dynamics characterised by the rapid initial decay of the linear polarisation. The important concept of the phonon memory time was introduced, which in the IB model corresponds to the polaron cloud formation time following an optical excitation in the QD. A key challenge identified was the combination of these exactly solvable models into a unified approach.

Chapter 3 addressed this challenge by utilising a path-integral approach to successfully combine the JC and IB models, resulting in a tensor-multiplication scheme. The Trotter decomposition with linked cluster expansion technique was focused on, and a generalisation was developed for multi-QD systems interacting with either shared or independent phonon baths. The propagator tensor emerged as

a central component of this technique, where each element contains a possible evolutionary path of the system within the finite memory time. This approach provides asymptotically exact calculations for any element of the density matrix, with accuracy improving as the number of neighbours increases, albeit at the cost of exponentially growing computational demands.

In Chapter 4, the asymptotically exact solution was used to investigate linear optical responses in a system of two coupled qubits interacting with a shared bath, using semiconductor QDs coupled to 3D acoustic phonons as a practical example. Despite only considering diagonal exciton-phonon coupling, which typically produces no ZPL broadening, the full calculation revealed ZPL broadening which is understood in terms of phonon-assisted transitions between the hybridised qubit states, analogous to the polariton states in the JC model. Importantly, we demonstrated that decoherence can be reduced by controlling the inter-qubit distance relative to the wavelength of the interacting bath modes. This effect is due to all QDs coupling to the same phonon modes, which is enabled by the coherent properties of the bath itself. Remarkably, the approximate calculation via FGR for real phonon-assisted transitions shows excellent agreement with the full calculation. For a 1D bath, we showed that decoherence can be eliminated entirely, with similar effects achievable for anisotropic qubits in a three-dimensional bath. The effect can be extended to multiple-qubit systems.

Finally, in Chapter 5, we developed an optimisation scheme which can be applied to path-integral tensor-multiplication techniques, specifically applying it to the Trotter decomposition with linked cluster expansion approach. This optimisation approximately doubles the number of neighbouring connections within the tensor network structure—a significant improvement given the exponential scaling characteristic of tensor multiplication schemes. This optimisation, which remaps and splits the tensor into *two* matrices, is a simple and natural stepping stone to a more sophisticated and advanced version of optimisation which has now been developed in parallel to the writing of this thesis. The new version represents the tensor as

an arbitrary number of matrices (limited by memory), where each matrix can contain a similar number of neighbours as the optimisation described in this chapter, providing a significant increase in the maximum number of neighbours achievable. While more memory efficient tensor representations exist, our approach enables an extrapolation scheme not available in other techniques. The combination of increased neighbour connections and extrapolation provides access to previously inaccessible regimes with improved convergence for systems with long memory times. As a demonstration of a system that can exhibit long memory times, we use a system of spatially separated quantum dots where increasing the separation increases the memory time. For already well-converged calculations, our optimisation scheme delivers substantial computational efficiency, reducing calculation time by up to two orders of magnitude.

Appendices

A Representations

A.1 Schrödinger representation

Starting with the time-dependent Schrödinger equation, the relation between the system Hamiltonian H and the wave function $\psi(t)$ is

$$i\frac{\partial}{\partial t}\psi(t) = H\psi(t), \tag{A.1}$$

for which the general solution is

$$\psi(t) = e^{-iHt}\psi(0), \tag{A.2}$$

where e^{-iHt} shows the time evolution of the wave function from $t = 0$. In the Schrödinger representation, the wave function is time-dependent, and the operators are time independent.

A.2 Heisenberg representation

An alternative representation is called the Heisenberg representation. In this representation, the wave function becomes independent of time and instead the operators absorb the time dependence. Consider the expectation value of a generic operator A,

$$\langle\psi(t)|\, A\, |\psi(t)\rangle = \left\langle e^{-iHt}\psi(0)\right|\, A\, \left|e^{-iHt}\psi(0)\right\rangle \tag{A.3}$$

$$= \langle\psi(0)|\, e^{iHt}Ae^{-iHt}\, |\psi(0)\rangle\,, \tag{A.4}$$

where we have extracted the explicit time dependence from the wave functions in the Schrödinger representation. Then, we are able to define an operator with the following time dependence

$$A(t) = e^{iHt}Ae^{-iHt}. \tag{A.5}$$

The time derivative of a general operator using these definitions is given by

$$\frac{d}{dt}A(t) = i\left[H, A(t)\right]. \tag{A.6}$$

A.3 Interaction representation

The interaction representation can be considered an intermediate case between the Schrödinger and Heisenberg representations since both the wave function and operators have time dependence. When the full Hamiltonian H is expressed as

$$H = H_0 + V, \tag{A.7}$$

where H_0 is the unperturbed Hamiltonian and V is a perturbation, the time-dependent Schrödinger equation is written as

$$H\left|\psi_S(t)\right\rangle = \left(H_0 + V\right)\left|\psi_S(t)\right\rangle = i\frac{\partial}{\partial t}\left|\psi_S(t)\right\rangle, \tag{A.8}$$

where the subscript S denotes the wave function in the Schrödinger representation. To find a solution to this equation, we introduce a new state vector $\psi_I(t)$ related to $\psi_S(t)$ by

$$\left|\psi_S(t)\right\rangle = e^{-iH_0t}\left|\psi_I(t)\right\rangle. \tag{A.9}$$

The subscript I refers to the interaction representation. Extracting the time dependence of operators can be done by finding the expectation value of an operator A,

$$\left\langle\psi_S(t)\right| A\left|\psi_S(t)\right\rangle = \left\langle e^{-iH_0t}\psi_I(t)\right| A\left|e^{-iH_0t}\psi_I(t)\right\rangle \tag{A.10}$$

$$= \left\langle\psi_I(t)\right| e^{iH_0t}Ae^{-iH_0t}\left|\psi_I(t)\right\rangle, \tag{A.11}$$

therefore, an operator in the interaction representation can be expressed as

$$\tilde{A}(t) = e^{iH_0t}Ae^{-iH_0t}, \tag{A.12}$$

where the tilde denotes an operator in the interaction picture. It is clear that the operators in the interaction representation have time-dependence governed by the unperturbed Hamiltonian, H_0. Then, substituting Eq.(A.9) into the time-dependent Schrödinger equation (A.8), we find

$$(H_0 + V)e^{-iH_0t} |\psi_I(t)\rangle = i\frac{\partial}{\partial t}\left(e^{-iH_0t} |\psi_I(t)\rangle\right), \tag{A.13}$$

and performing the partial differentiation gives

$$(H_0 + V)e^{-iH_0t} |\psi_I(t)\rangle = H_0\, e^{-iH_0t} |\psi_I(t)\rangle + ie^{-iH_0t}\frac{\partial}{\partial t} |\psi_I(t)\rangle, \tag{A.14}$$

then cancelling the common term and multiplying e^{iH_0t} on both sides of the equation, we find

$$e^{iH_0t}Ve^{-iH_0t} |\psi_I(t)\rangle = i\frac{\partial}{\partial t} |\psi_I(t)\rangle, \tag{A.15}$$

where $e^{iH_0t}Ve^{-iH_0t}$ is defined as the interaction representation of an operator in Eq.(A.12). Therefore the Schrödinger equation in the interaction representation is given by

$$i\frac{\partial}{\partial t} |\psi_I(t)\rangle = \tilde{V}(t) |\psi_I(t)\rangle, \tag{A.16}$$

which shows the time-dependence of the wave function in the interaction picture is governed by the perturbation V.

B Linear optical polarisation

The derivation below is a more general case with multiple possible system excitation/measurement channels and a phonon bath. In the JC model, there is no phonon bath, simplifying the derivation. And, in the IB model the derivation is similar, but the excitation and measurement channels are limited to $|X\rangle$ only since there is only one QD, rather than $|k\rangle$ and $|j\rangle$.

B.1 Multiple QDs coupled to a cavity with an acoustic phonon bath

The density matrix of the system in the fully unexcited state is given by

$$\rho(-\infty) = |0\rangle\langle 0| \otimes \rho_{\text{ph}}, \tag{B.1}$$

where the density matrix of the phonon subspace ρ_{ph} is

$$\rho_{\text{ph}} = \frac{e^{-\beta H_{\text{ph}}}}{\text{Tr}\{e^{-\beta H_{\text{ph}}}\}_{\text{ph}}}, \tag{B.2}$$

where $\beta = \frac{1}{k_B T}$, and the subscript ph on the trace refers to the trace being taken over all phonon states. Then, applying a pulsed excitation of the form

$$H_{\text{ext}}(t) = \mathcal{V}\delta(t), \tag{B.3}$$

where

$$\mathcal{V} = \mu(\tilde{c}^\dagger + \tilde{c}), \tag{B.4}$$

to the system, where $\tilde{c}^\dagger$ ($\tilde{c}$) is a general creation (destruction) operator results in the density matrix immediately after the pulsed excitation being described by the transformation

$$\rho(0_+) = e^{-i\int_{-\infty}^{\infty} H_{\text{ext}}(t')dt'}\rho(-\infty)e^{i\int_{-\infty}^{\infty} H_{\text{ext}}(t')dt'} = e^{-i\mathcal{V}}\rho(-\infty)e^{i\mathcal{V}}. \tag{B.5}$$

$\tilde{c}^\dagger$ ($\tilde{c}$) is given explicitly by $|k\rangle\langle 0|$ ($|0\rangle\langle k|$), where k represents the excitation channel, which can be any excitonic state $1, 2$ or the cavity channel C. The subsequent time evolution of $\rho(0_+)$ is given by the Schrödinger time evolution,

$$\rho(t) = e^{-iHt}\rho(0_+)e^{iHt}. \tag{B.6}$$

Substituting these into the expression for polarisation Eq.(2.1.7), we obtain:

$$\text{P}(t) = \text{Tr}\big\{e^{-iHt}(e^{-i\mathcal{V}}|0\rangle\langle 0|e^{i\mathcal{V}} \otimes \rho_{\text{ph}})e^{iHt}c\big\}, \tag{B.7}$$

where c is a general destruction operator explicitly given by $|0\rangle\langle j|$, where j is the chosen measurement channel ($j = 1, 2, C$), effectively extracting the chosen coherence term from the full density matrix.

The exponentials $e^{\pm i\mathcal{V}}$ can be expanded as a Taylor series, giving

$$\mathrm{P}(t) = \mathrm{Tr}\{e^{-iHt}\left(\left(1 - i\mu(\tilde{c}^\dagger + \tilde{c}) + ...\right)|0\rangle\langle 0|\left(1 + i\mu(\tilde{c}^\dagger + \tilde{c}) + ...\right) \otimes \rho_{\mathrm{ph}}\right) e^{iHt}c\}. \tag{B.8}$$

Writing $\tilde{c}^\dagger$, $\tilde{c}$ and c explicitly in terms of k and j and using the orthonormality of the states and keeping only terms linear in μ, the linear polarisation can be expressed as

$$\mathrm{P}(t) = \mathrm{Tr}\{e^{-iHt}(|k\rangle \otimes \rho_{\mathrm{ph}})e^{iH_{\mathrm{ph}}t}\langle j|\}. \tag{B.9}$$

In particular, we have used the fact that $\langle k| e^{iHt} |0\rangle$ is simply zero, due to the Hamiltonian H not having any way of causing the $|0\rangle$ state to undergo a transition to $|k\rangle$ and $\langle 0| e^{iHt} |0\rangle = e^{iH_{\mathrm{ph}}t}$.

Now evaluating this trace in a system basis $|n\rangle$ and phonon basis $|\alpha\rangle$,

$$\mathrm{P}(t) = \sum_{n,\alpha} \langle n| \otimes \langle \alpha| \left(e^{-iHt}(|k\rangle |j\rangle \otimes \rho_{\mathrm{ph}} e^{iH_{\mathrm{ph}}t})\right) |n\rangle \otimes |\alpha\rangle, \tag{B.10}$$

and using the fact that $|k\rangle\langle j|n\rangle = \delta_{j,n}|k\rangle$, we find

$$\mathrm{P}(t) = \sum_{\alpha} \langle j| \otimes \langle \alpha| e^{-iHt}(|k\rangle \otimes (\rho_{\mathrm{ph}} e^{iH_{\mathrm{ph}}t} |\alpha\rangle)). \tag{B.11}$$

Denoting $|k\rangle \otimes |\phi\rangle = |k\rangle \otimes (\rho_{\mathrm{ph}} e^{iH_{\mathrm{ph}}t} |\alpha\rangle)$, we have

$$\mathrm{P}(t) = \sum_{\alpha} (\langle j| \otimes \langle \alpha|) e^{-iHt}(|k\rangle \otimes |\phi\rangle). \tag{B.12}$$

Using the rule of tensor inner products

$$(\langle a| \otimes \langle b|)\hat{X}(|c\rangle \otimes |d\rangle) = \langle b| \left(\langle a| \hat{X} |c\rangle\right) |d\rangle, \tag{B.13}$$

the linear polarisation becomes

$$\mathrm{P}(t) = \sum_{\alpha} \langle\alpha| \left(\langle j|\, e^{-iHt}\, |k\rangle\right) \rho_{\mathrm{ph}} e^{iH_{\mathrm{ph}}t}\, |\alpha\rangle\,, \tag{B.14}$$

noting that $\langle j|\, e^{-iHt}\, |k\rangle$ is actually an operator in the phonon subspace (because it is what is remaining after contracting with the system states). Eq.B.14 is the definition of a trace over the phonon Hilbert space:

$$\mathrm{P}(t) = \mathrm{Tr}\big\{\langle j|\, e^{-iHt}\, |k\rangle\, \rho_{\mathrm{ph}} e^{iHt}\big\}, \tag{B.15}$$

and subsequently using the definition of the expectation value of an operator Eq.2.1.6, the final expression for the linear polarisation is given by

$$\mathrm{P}_{jk}(t) = \langle\langle j|\, U(t)\, |k\rangle\rangle_{\mathrm{ph}}, \tag{B.16}$$

with $U(t) = e^{iH_{\mathrm{ph}}t} e^{-iHt}$.

C Absorption

The absorption $\mathrm{A}(\omega)$ is the transition rate into all states from an initial state. Fermi's golden rule F, giving the transition rate from a single initial state $|i\rangle$ to a single final state $|f\rangle$ is defined as

$$F_{i\to f}(\omega) = 2\pi |\, \langle f|\, \mathcal{V}\, |i\rangle\, |^2 \delta(E_f - E_i - \omega), \tag{C.1}$$

where $\mathcal{V}$ is the pulsed excitation applied at time $t = 0$, given by Eq. (2.1.9). $E_{f(i)}$ is the energy of the final (initial) state, and the delta function enforces energy conservation, ensuring the photon energy ω matches the energy difference $E_f - E_i$. The absorption spectrum $A(\omega)$ is the total transition rate, summed over all possible initial and final states, weighted by the probability w_i of occupying the initial state

and is given by

$$\mathrm{A}(\omega) = \sum_{i,f} w_i F_{i\to f}(\omega) = 2\pi \sum_{i,f} w_i |\left\langle f\right| \mathcal{V} \left|i\right\rangle|^2 \delta(E_f - E_i - \omega). \tag{C.2}$$

In the frequency domain, the delta function is written as

$$\delta(E_f - E_i - \omega) = \frac{1}{2\pi}\int_{-\infty}^{\infty} e^{i(E_f - E_i - \omega)t} dt = \frac{1}{2\pi}\int_{-\infty}^{\infty} e^{i(E_f - E_i)t} e^{-i\omega t} dt, \tag{C.3}$$

Substituting into Eq. (C.2), we get

$$\mathrm{A}(\omega) = \sum_{i,f} \int_{-\infty}^{\infty} w_i |\left\langle f\right| \mathcal{V} \left|i\right\rangle|^2 e^{i(E_f - E_i)t} e^{-i\omega t} dt. \tag{C.4}$$

Using $|\left\langle f\right| \mathcal{V} \left|i\right\rangle|^2 = \left\langle i\right| \mathcal{V}^\dagger \left|f\right\rangle \left\langle f\right| \mathcal{V} \left|i\right\rangle$, this becomes

$$\mathrm{A}(\omega) = \sum_{i,f} w_i \left\langle i\right| \mathcal{V}^\dagger \left|f\right\rangle \left\langle f\right| \mathcal{V} \left|i\right\rangle \int_{-\infty}^{\infty} e^{i(E_f - E_i)t} e^{-i\omega t} dt. \tag{C.5}$$

We then use $e^{iHt}\left|f\right\rangle = e^{iE_f t}\left|f\right\rangle$, and so:

$$\mathrm{A}(\omega) = \sum_{i,f} w_i \int_{-\infty}^{\infty} \left\langle i\right| e^{-iHt} \mathcal{V}^\dagger e^{iHt} \left|f\right\rangle \left\langle f\right| \mathcal{V} \left|i\right\rangle e^{-i\omega t} dt. \tag{C.6}$$

Inserting the identity $\sum_f \left|f\right\rangle \left\langle f\right| = 1$ and expressing $w_i = \left\langle i\right| \rho(-\infty) \left|i\right\rangle$, the sum becomes a trace:

$$\mathrm{A}(\omega) = \int_{-\infty}^{\infty} dt\, e^{-i\omega t} \,\mathrm{Tr}\big\{\rho(-\infty) e^{-iHt} \mathcal{V}^\dagger e^{iHt} \mathcal{V}\big\}. \tag{C.7}$$

Using the cyclic property of the trace and expanding $\mathcal{V}$ as in Eq. (2.1.9), we get

$$\mathrm{A}(\omega) = \int_{-\infty}^{\infty} dt\, e^{-i\omega t} \left(\mu \,\mathrm{Tr}\big\{e^{-iHt} \mathcal{V} \rho(-\infty) e^{iHt} c\big\} + \mu^* \,\mathrm{Tr}\big\{e^{-iHt} \mathcal{V}^\dagger \rho(-\infty) e^{iHt} c^\dagger\big\}\right). \tag{C.8}$$

These two terms correspond to $\mathrm{P_L}(t)$ and $\mathrm{P_L^*}(t)$, respectively, as defined in Eq. (2.1.14). Further neglecting the unimportant μ terms, we find

$$\mathrm{A}(\omega) = \int_0^{\infty} e^{-i\omega t} [\mathrm{P_L}(t) + \mathrm{P_L^*}(t)] dt = 2\,\mathrm{Re}\left[\int_0^{\infty} e^{-i\omega t} \mathrm{P_L}(t) dt\right], \tag{C.9}$$

where we have used the fact that $\int_0^\infty e^{-i\omega t} P_L^*(t)dt = (\int_0^\infty e^{i\omega t} P_L(t)dt)^*$. This results in the final expression for the absorption spectrum,

$$\mathrm{A}(\omega) \propto \mathrm{Re}\left[\int_0^\infty e^{-i\omega t}\mathrm{P_L}(t)dt\right]. \tag{C.10}$$

It should be noted that in our expression for the linear polarisation, Eq. (2.1.14), we omitted the prefactor of $-i$. If this factor were retained, Eq. (C.10) would instead involve the imaginary part of the polarisation.

D Baker-Hausdorff lemma

The Baker-Campbell-Hausdorff (BCH) formula finds C such that $e^C = e^A e^B$ for when A and B are non-commuting operators. i.e. $[A, B] = AB - BA \neq 0$. A closely related identity, which is often a key step in proving the BCH formula, is the Baker-Hausdorff lemma (also sometimes called the Hadamard lemma). This lemma is particularly useful for computing expressions of the form $e^A B e^{-A}$. It states for operators A and B,

$$e^A B e^{-A} = B + [A, B] + \frac{1}{2!}[A, [A, B]] + \frac{1}{3!}[A, [A, [A, B]]] + \cdots . \tag{D.1}$$

This is an operator identity that expands the transformed operator B as an infinite series of nested commutators with A. In Eq.2.3.19, we have $A = iH_{\mathrm{ph}}t$, and V consists of $b_{\mathbf{q}}+b^\dagger_{-\mathbf{q}}$. Considering a single mode $\mathbf{q}$, to find the explicit time evolution of $b_{\mathbf{q}}$,

$$\tilde{b}_{\mathbf{q}}(t) = e^{iH_{\mathrm{ph}}t} b_{\mathbf{q}} e^{-iH_{\mathrm{ph}}t}, \tag{D.2}$$

we can use the Baker-Hausdorff lemma. The first commutator is $[A, B] = i[H_{\mathrm{ph}}, b_{\mathbf{q}}]t$, where

$$[H_{\mathrm{ph}}, b_{\mathbf{q}}] = \sum_{\mathbf{q}'} \omega_{q'} [b^\dagger_{\mathbf{q}'} b_{\mathbf{q}'}, b_{\mathbf{q}}], \tag{D.3}$$

and using the commutation relations $[b^\dagger_{\mathbf{q}'}, b_q] = -\delta_{\mathbf{q}',\mathbf{q}}$ and $[b_{\mathbf{q}'}, b_{\mathbf{q}}] = 0$, we compute:

$$[b^\dagger_{\mathbf{q}'} b_{\mathbf{q}'}, b_{\mathbf{q}}] = b^\dagger_{\mathbf{q}'}[b_{\mathbf{q}'}, b_{\mathbf{q}}] + [b^\dagger_{\mathbf{q}'}, b_{\mathbf{q}}] b_{\mathbf{q}'} = -\delta_{\mathbf{q}',\mathbf{q}} b_{\mathbf{q}'}. \tag{D.4}$$

So:

$$i[H_{\text{ph}}, b_{\mathbf{q}}]t = -i\omega_q b_{\mathbf{q}}, \tag{D.5}$$

and similarly with the next commutator,

$$[iH_{\text{ph}}t, [iH_{\text{ph}}t, b_{\mathbf{q}}]] = [iH_{\text{ph}}t, -i\omega_q b_{\mathbf{q}}] = (i\omega_q t)^2 b_{\mathbf{q}}. \tag{D.6}$$

Continuing, the n^{th} commutator is given by $(-i\omega_q t)^n b_{\mathbf{q}}$, and the lemma becomes:

$$\tilde{b}_{\mathbf{q}}(t) = b_{\mathbf{q}} + (-i\omega_q t) b_{\mathbf{q}} + \frac{1}{2!}(-i\omega_q t)^2 b_{\mathbf{q}} + \ldots, \tag{D.7}$$

which is a Taylor series for an exponential,

$$\tilde{b}_{\mathbf{q}}(t) = b_{\mathbf{q}} e^{-i\omega_q t}. \tag{D.8}$$

Similarly, for $b^\dagger_{-\mathbf{q}}$, the time evolution in the interaction representation is:

$$\tilde{b}^\dagger_{-\mathbf{q}}(t) = b^\dagger_{-\mathbf{q}} e^{-i\omega_q t}. \tag{D.9}$$

Therefore, the time evolution of V in the interaction representation is,

$$\tilde{V}(t) = \sum_{\mathbf{q}} \lambda_{\mathbf{q}} (b_{\mathbf{q}} e^{-i\omega_q t} + b^\dagger_{-\mathbf{q}} e^{-i\omega_q t}). \tag{D.10}$$

E The time evolution operator $U(t)$

The time evolution operator is defined to be an operator that generates the interaction representation wave function at a time t from the wave function at $t = 0$, defined as (see Appendix A.3),

$$\psi_I(t) = e^{iH_0 t} e^{-iHt} \psi_S(0), \tag{E.1}$$

hence, the time evolution operator $U(t)$ is given by

$$U(t) = e^{iH_0 t} e^{-iHt}. \tag{E.2}$$

Replacing $\psi_I(t)$ in Eq.A.16 by $U(t)\psi_I(0)$ gives the Schrödinger equation in terms of $U(t)$,

$$\frac{d}{dt}U(t) = -i\tilde{V}(t)U(t). \tag{E.3}$$

Integrating both sides from 0 to t, we find

$$U(t) = 1 - i\int_0^t \tilde{V}(t_1)U(t_1)dt_1, \tag{E.4}$$

which can be solved using an iterative approach (Dyson series). Noting that $U(t=0) = 1$, $U(t_1)$ can be substituted back into itself, giving:

$$U(t) = 1 - i\int_0^t \tilde{V}(t_1)\,dt_1 + (-i)^2\int_0^t \tilde{V}(t_1)\left(\int_0^{t_1}\tilde{V}(t_2)\,dt_2\right)dt_1 + \cdots. \tag{E.5}$$

Paying attention the nested integral, which runs from 0 to t_1 with $t_1 \leq t$, we continue this iterative process, where the next term has an extra nested integral and the integration limits would be $t_3 \leq t_2$. This structure of the integration limits ensures time-ordering automatically. To convert this into a time-ordered exponential, we need to transform these nested integrals into integrals over the same range. This is achieved in the following way,

$$U(t) = \sum_0^\infty \frac{(-i)^n}{n!}\int_0^t dt_1 ... \int_0^t dt_n \mathcal{T}\tilde{V}(t_1)...\tilde{V}(t_n) \tag{E.6}$$

$$= \mathcal{T}\left\{\exp\left\{-i\int_0^t \tilde{V}(t_1)dt_1\right\}\right\}, \tag{E.7}$$

where $\mathcal{T}$ denotes the time ordering operator, which places an arbitrary number of operators, each acting at different times into their proper order, placing the operators acting at earlier times to the right of those acting at later times. The $1/n!$ factor appears because we're replacing the restricted integration domain (where times are ordered) with the full hypercube of possible time values, and then ex-

plicitly imposing time ordering with the time evolution operator. By considering all possible permutations of the time variables, there is a corresponding integration region with its own time ordering. Due to the symmetry of the integrand after applying the time ordering operator, the integral over each permutation is the same, and there are $n!$ total permutations. Therefore, any of these ordered integrals equals $1/n!$ of the integral over the entire hypercube. In other words, the factor $1/n!$ compensates for the over counting due to permutations of the time variables, since all orderings are equivalent under the time evolution operator.

F Using linked cluster expansion in the IB model

This section shows how to use linked cluster expansion to re-express the expectation value of the time-evolution operator $\langle U(t)\rangle$ compactly as a cumulant in the IB model. We start from Eq.2.3.18,

$$\langle U(t)\rangle = \left\langle \mathcal{T}\Big[\exp\Big(-i\int_0^t dt_1 \tilde{V}(t_1)\Big)\Big]\right\rangle, \tag{F.1}$$

where $\mathcal{T}$ denotes the time ordering operator and $\langle ...\rangle$ denotes the expectation value taken over all phonon states. The tilde denotes the interaction representation of V (see Appendix A.3):

$$\tilde{V}(t) = e^{iH_{\mathrm{ph}}t} V e^{-iH_{\mathrm{ph}}t}. \tag{F.2}$$

To bring Eq.(F.2) into a usable form, the Baker-Hausdorff lemma (Appendix D) is used, which allows for a more explicit form of the time dependence to be found, resulting in

$$\tilde{V}(t) = \sum_{\mathbf{q}} \lambda^*_{\mathbf{q}} b_{\mathbf{q}} e^{-i\omega_q t} + \lambda_{\mathbf{q}} b^\dagger_{-\mathbf{q}} e^{i\omega_q t}. \tag{F.3}$$

Next, let us consider the perturbation series generated by expanding Eq.(F.1),

$$\left\langle \mathcal{T}\Big[\exp\Big(-i\int_0^t dt_1 \tilde{V}(t_1)\Big)\Big]\right\rangle = \sum_{n=0}^{\infty} \frac{(-i)^n}{n!}\int_0^t dt_1 \int_0^t dt_2 ... \int_0^t dt_n \langle \mathcal{T}\tilde{V}(t_1)\tilde{V}(t_2)...\tilde{V}(t_n)\rangle, \tag{F.4}$$

derived in Appendix E. In Eq. (F.4), $\tilde{V}(t)$ consists of phonon creation and annihilation operators $b^\dagger_{\mathbf{q}}$ and $b_{\mathbf{q}}$, so, within the expectation value, there must be an equal number of phonon creation and destruction operators to give a non-zero result in each term in the series. This condition is only possible if there is an even number of $\tilde{V}$ operators. Consider the second-order term:

$$
\begin{aligned}
&-\frac{1}{2}\int_0^t dt_1 \int_0^t dt_2 \langle \mathcal{T}\tilde{V}(t_1)\tilde{V}(t_2)\rangle \\
&= -\frac{1}{2}\int_0^t dt_1 \int_0^t dt_2 \sum_{\mathbf{q},\mathbf{q}'} \left\langle \mathcal{T}\left(\lambda^*_{\mathbf{q}} b_{\mathbf{q}} e^{-i\omega_q t_1} + \lambda_{\mathbf{q}} b^\dagger_{-\mathbf{q}} e^{i\omega_q t_1}\right)\left(\lambda^*_{\mathbf{q}'} b_{\mathbf{q}'} e^{-i\omega_{q'} t_2} + \lambda_{\mathbf{q}'} b^\dagger_{-\mathbf{q}'} e^{i\omega_{q'} t_2}\right)\right\rangle
\end{aligned}
\tag{F.5}
$$

which will be denoted $K(t)$, and is the building block for all higher order terms, as we will see. Let us consider higher order terms, such as the fourth order term of the series in Eq.(F.4), $\langle \mathcal{T}\tilde{V}(t_1)\tilde{V}(t_2)\tilde{V}(t_3)\tilde{V}(t_4)\rangle$. Wick's theorem is used to reduce the products of operators to sums of time-ordered pairs products of the operators, taking into account all possible combinations. Using Wick's theorem, Eq.(F.4) becomes

$$
\begin{aligned}
&\left\langle \mathcal{T}\Big[\exp\Big(-i\int_0^t dt_1 \tilde{V}(t_1)\Big)\Big]\right\rangle \\
&= 1 - \frac{1}{2}\int_0^t dt_1 \int_0^t dt_2 \langle \mathcal{T}\tilde{V}(t_1)\tilde{V}(t_2)\rangle + \frac{1}{24}\int_0^t dt_1 \int_0^t dt_2 \int_0^t dt_3 \int_0^t dt_4 \times \\
&\Bigg(\langle \mathcal{T}\tilde{V}(t_1)\tilde{V}(t_2)\rangle\langle \mathcal{T}\tilde{V}(t_3)\tilde{V}(t_4)\rangle + \langle \mathcal{T}\tilde{V}(t_1)\tilde{V}(t_3)\rangle\langle \mathcal{T}\tilde{V}(t_2)\tilde{V}(t_4) \\
&+ \langle \mathcal{T}\tilde{V}(t_1)\tilde{V}(t_4)\rangle\langle \mathcal{T}\tilde{V}(t_2)\tilde{V}(t_3)\rangle \Bigg) + \dots .
\end{aligned}
\tag{F.6}
$$

Let us focus on the first pairing in the fourth order term, $\langle \mathcal{T}\tilde{V}(t_1)\tilde{V}(t_2)\rangle\langle \mathcal{T}\tilde{V}(t_3)\tilde{V}(t_4)\rangle$. Since the integrals in Eq. (F.6) all contain the same limits, this product of pairs is therefore identical to a product of two second-order terms, $K(t)^2$. Therefore, all second order and beyond terms in the series can be represented in terms of the second-order term $K(t)$:

$$
\left\langle \mathcal{T}\Big[\exp\Big(-i\int_0^t dt_1 \tilde{V}(t_1)\Big)\Big]\right\rangle = 1 + K(t) + \frac{1}{2}K^2(t) + \dots = e^{K(t)}, \tag{F.7}
$$

where $K(t)$ is known as the cumulant. In fact, this cancellation of higher order terms is a special feature of the IB model and a consequence of diagonal and bilinear phonon coupling. Thus, the IB model is exactly solvable and the linear optical polarisation, Eq.(2.3.17), can be compactly written as

$$\mathrm{P}(t) = \theta(t) e^{-i\omega_X t} e^{K(t)}. \tag{F.8}$$

G Evaluating the cumulant $K(t)$

The expectation value in the cumulant $K(t)$, Eq.(2.3.21), where $\tilde{V}(t)$ is defined in Eq.(2.3.19), is evaluated in the following way,

$$\langle \mathcal{T}\tilde{V}(t_1)\tilde{V}(t_2)\rangle = \sum_{\mathbf{q},\mathbf{q}'} \Big\langle \mathcal{T}\Big(\lambda^*_{\mathbf{q}} b_{\mathbf{q}} e^{-i\omega_q t_1} + \lambda_{\mathbf{q}} b^\dagger_{-\mathbf{q}} e^{i\omega_q t_1}\Big)\Big(\lambda^*_{\mathbf{q}'} b_{\mathbf{q}'} e^{-i\omega_{q'} t_2} + \lambda_{\mathbf{q}'} b^\dagger_{-\mathbf{q}'} e^{i\omega_{q'} t_2}\Big)\Big\rangle. \tag{G.1}$$

Then, multiplying out the brackets and considering the case where $t_1 > t_2$, we have

$$\sum_{\mathbf{q}} |\lambda_{\mathbf{q}}|^2 \Big(\langle b_{\mathbf{q}} b^\dagger_{\mathbf{q}}\rangle e^{-i\omega_q(t_1-t_2)} + \langle b^\dagger_{\mathbf{q}} b_{\mathbf{q}}\rangle e^{i\omega_q(t_1-t_2)}\Big), \tag{G.2}$$

and similarly, when $t_2 > t_1$,

$$\sum_{\mathbf{q}} |\lambda_{\mathbf{q}}|^2 \Big(\langle b_{\mathbf{q}} b^\dagger_{\mathbf{q}}\rangle e^{-i\omega_q(t_2-t_1)} + \langle b^\dagger_{\mathbf{q}} b_{\mathbf{q}}\rangle e^{i\omega_q(t_2-t_1)}\Big), \tag{G.3}$$

where the orthogonality of states has been used i.e. $\langle b_{\mathbf{q}} b_{\mathbf{q}}\rangle = \langle b^\dagger_{\mathbf{q}} b^\dagger_{\mathbf{q}}\rangle = 0$ and $\langle b_{\mathbf{q}} b_{-\mathbf{q}'}\rangle = \delta_{\mathbf{q},-\mathbf{q}'}\langle b_{\mathbf{q}} b^\dagger_{\mathbf{q}}\rangle$. Combining Eq. (G.2) and Eq. (G.3), the general case is expressed as:

$$\sum_{\mathbf{q}} |\lambda_{\mathbf{q}}|^2 \Big(\langle b_{\mathbf{q}} b^\dagger_{\mathbf{q}}\rangle e^{-i\omega_q|t_1-t_2|} + \langle b^\dagger_{\mathbf{q}} b_{\mathbf{q}}\rangle e^{i\omega_q|t_1-t_2|}\Big). \tag{G.4}$$

By using the Bose commutation relation, and the fact that $b^\dagger_{\mathbf{q}} b_{\mathbf{q}}$ is the number operator $N(\omega_q)$ for phonons, we can write,

$$\sum_{\mathbf{q}} |\lambda_{\mathbf{q}}|^2 \Big((1+N(\omega_q)) e^{-i\omega_q|t_1-t_2|} + N(\omega_q) e^{i\omega_q|t_1-t_2|}\Big), \tag{G.5}$$

where $N(\omega)$ is the Bose-distribution function defined in Eq.2.3.24. This results in the cumulant, explicitly given by

$$K(t) = -\frac{1}{2}\int_0^t dt_1 \int_0^t dt_2 \sum_{\mathbf{q}} |\lambda_{\mathbf{q}}|^2 \Big((1+N(\omega)) e^{-i\omega_q |t_1 - t_2|} + N(\omega) e^{i\omega_q |t_1 - t_2|} \Big). \quad \text{(G.6)}$$

Analytically performing the double integration over time gives Eq. (2.3.23).

H Exciton-phonon coupling elements and phonon spectral density

Throughout this work, we consider semiconductor QDs as candidates for qubits, using typical InGaAs parameters outlined in [37, 46]. At low temperatures, the exciton-phonon interaction is primarily governed by the deformation potential coupling with longitudinal acoustic phonons. Assuming that the phonon parameters within the QDs closely resemble those of the surrounding material, and further assuming that the acoustic phonons exhibit linear dispersion, $\omega_q = v_s q$, where $q = |\mathbf{q}|$ and v_s is the sound velocity in the material, the exciton-phonon matrix coupling element for an exciton in qubit $j = 1, 2$ is given by

$$\lambda_{\mathbf{q},j} = \frac{\sqrt{q}\, \mathcal{D}_j(\mathbf{q})}{\sqrt{2\rho_m v_s \mathcal{V}}}, \quad \text{(H.1)}$$

where ρ_m is the mass density of the material, $\mathcal{V}$ is the sample volume, and

$$\mathcal{D}_j(\mathbf{q}) = \int d\mathbf{r}_e \int d\mathbf{r}_h |\Psi_{X,j}(\mathbf{r}_e, \mathbf{r}_h)|^2 \left(D_c e^{i\mathbf{q}\cdot\mathbf{r}_e} - D_v e^{i\mathbf{q}\cdot\mathbf{r}_h} \right) \quad \text{(H.2)}$$

is the coupling form-factor [37, 46], with $D_{c(v)}$ being the deformation potential of the conduction (valence) band. Assuming a factorisable form of the exciton wave functions, $\Psi_{X,j}(\mathbf{r}_e, \mathbf{r}_h) = \psi_{e,j}(\mathbf{r}_e)\psi_{h,j}(\mathbf{r}_h)$, where $\psi_{e(h),j}(\mathbf{r})$ is the confined electron (hole) ground state wave function in QD j, the form-factor simplifies to

$$\mathcal{D}_j(\mathbf{q}) = \int d\mathbf{r} \left[D_c |\psi_{e,j}(\mathbf{r})|^2 - D_v |\psi_{h,j}(\mathbf{r})|^2 \right] e^{i\mathbf{q}\cdot\mathbf{r}}. \quad \text{(H.3)}$$

H.1 Isotropic QDs

Choosing spherically symmetric parabolic confinement potentials, the ground-state wave functions of the carriers take Gaussian form, which in the simpler case of equal electron and hole confinement lengths, $l_{e,j} = l_{h,j} = l_j$, is given by

$$\psi_j(\mathbf{r}) = \frac{1}{\pi^{3/4} l_j^{3/2}} \exp\left\{-\frac{(\mathbf{r}-\mathbf{d}_j)^2}{2l_j^2}\right\}, \tag{H.4}$$

where $\mathbf{d}_j$ is the coordinate of the center of QD j. Substituting Eq. (H.4) into Eq. (H.3), performing the integration over the whole space and substituting the result into Eq. (H.1), we obtain

$$\lambda_{\mathbf{q},j} = \sqrt{q}\lambda_0 \exp\{-l_j^2 q^2/4\} e^{i\mathbf{q}\cdot\mathbf{d}_j}, \tag{H.5}$$

where

$$\lambda_0 = \frac{D_c - D_v}{\sqrt{2\rho_m v_s \mathcal{V}}}. \tag{H.6}$$

Choosing the first QD located at the origin ($\mathbf{d}_1 = 0$) we find $\mathbf{d}_2 = \mathbf{d}$, where $\mathbf{d}$ is the distance vector between the QDs. Converting the summation over $\mathbf{q}$ to an integration, $\sum_{\mathbf{q}} \to \frac{\mathcal{V}}{(2\pi)^3}\int d\mathbf{q}$, and using spherical coordinates, the spectral density $J_{jj'}(\omega)$ defined by Eq. (3.3.15) takes the form

$$\begin{aligned} J_{jj'}(\omega) =& \frac{J_0 v_s^4}{2}\int_0^\infty dq\, q^3 \exp\{-q^2 l^2\}\delta(\omega - v_s q) \\ &\times \int_0^\pi d\theta \sin\theta \begin{cases} 1 & j = j' \\ \exp\{iqd\cos\theta\} & j < j' \\ \exp\{-iqd\cos\theta\} & j > j', \end{cases} \end{aligned} \tag{H.7}$$

where

$$J_0 = \frac{(D_c - D_v)^2}{4\pi^2 \rho_m v_s^5}, \tag{H.8}$$

$d = |\mathbf{d}|$, and $l^2 = (l_j^2 + l_{j'}^2)/4$ (for brevity omitting the indices j and j' in the new length l introduced). Note that the reason for defining J_0 in this way, not absorbing the other constant factors $v_s^4/2$ is because J_0 is the constant factor in

the single QD case, i.e. in [43]. Performing the integration over the polar angle θ, we finally find

$$J_{jj'}(\omega) = J_0\,\omega^3 \exp\left\{-\frac{\omega^2 l^2}{v_s^2}\right\} \times \begin{cases} 1 & j = j' \\ \mathrm{sinc}\left(\frac{\omega d}{v_s}\right) & j \neq j' \,, \end{cases} \tag{H.9}$$

where $\mathrm{sinc}(x) = \sin(x)/x$.

H.2 Anisotropic QDs

For anisotropic QDs with in-plane confinement length l_j and perpendicular confinement length $l_{j,\perp}$, the Gaussian ground-state wave functions Eq. (H.4) are modified to

$$\begin{aligned} \psi_j(x,y,z) &= \frac{1}{\pi^{3/4} l_j l_{\perp,j}^{1/2}} \exp\left\{-\frac{(x-d_{x,j})^2 + (y-d_{y,j})^2}{2l_j^2}\right\} \\ &\quad \times \exp\left\{-\frac{(z-d_{z,j})^2}{2l_{\perp,j}^2}\right\}, \end{aligned} \tag{H.10}$$

where we have again taken the case of identical electron and hole localisation lengths, $l_{e,j} = l_{h,j} = l_j$ and $l_{\perp,e,j} = l_{\perp,h,j} = l_{\perp,j}$, and used the components $(d_{x,j}, d_{y,j}, d_{z,j})$ of the vector $\mathbf{d}_j$. Following the same procedure as for isotropic qubits, we obtain

$$\lambda_{\mathbf{q},j} = \sqrt{q}\lambda_0 \exp\left\{-l_j^2(q_x^2+q_y^2)/4 - l_{\perp,j}^2 q_z^2/4\right\} e^{i\mathbf{q}\cdot\mathbf{d}_j} \,. \tag{H.11}$$

The above equation is assuming that both QDs have the same anisotropy axis (along z). Assuming further that the centers of the QDs lie on the z-axis, so that $d_{x,j} = d_{y,j} = 0$ and $d_{z,j} = d_j$, we find in spherical coordinates

$$\lambda_{\mathbf{q},j} = \sqrt{q}\lambda_0 \exp\left(-q^2(l_j^2 \sin^2(\theta) + l_{\perp,j}^2 \cos^2(\theta))/4 + iqd_j\cos(\theta)\right), \tag{H.12}$$

using $q_x = q\sin(\theta)\cos(\phi)$, $q_y = q\sin(\theta)\sin(\phi)$, and $q_z = q\cos(\theta)$. The spectral density is then given by

$$J_{jj'}(\omega) = \frac{J_0 v_s^4}{2}\int_0^\infty dq\, q^3\delta(\omega - v_s q)\int_0^\pi d\theta\sin(\theta)\exp\left\{-q^2 l^2\sin^2(\theta) - q^2 l_\perp^2\cos^2(\theta)\right\} \times \begin{cases} 1 & j = j' \\ \exp\{iqd\cos(\theta)\} & j < j' \\ \exp\{-iqd\cos(\theta)\} & j > j' \,, \end{cases} \tag{H.13}$$

where $l^2 = (l_j^2 + l_{j'}^2)/4$ and $l_\perp^2 = (l_{\perp,j}^2 + l_{\perp,j'}^2)/4$. Performing the integration over the polar angle θ, we obtain

$$J_{jj'}(\omega) = J_0\,\omega^3 e^{-q^2 l_\perp^2} \times \begin{cases} F\left(0, q\sqrt{l_\perp^2 - l^2}\right) & j = j' \\ F\left(\frac{d}{2\sqrt{l_\perp^2 - l^2}}, q\sqrt{l_\perp^2 - l^2}\right) & j \neq j' \end{cases} \tag{H.14}$$

with $q = \omega/v_s$, where

$$F(\alpha,\beta) = \frac{\sqrt{\pi}}{4\beta}\left[e^{-2i\alpha\beta}w(\alpha - i\beta) - e^{2i\alpha\beta}w(\alpha + i\beta)\right] , \tag{H.15}$$

and $w(z)$ is the Faddeeva function. Note that Eq. (H.14) is valid for both $l_\perp > l$ and $l_\perp < l$, and in the isotropic case $l_\perp = l$ simplifies to Eq. (H.9), as shown in Sec. H.3 below.

H.3 Faddeeva function and some properties of $F(\alpha, \beta)$

The Faddeeva function $w(z)$ is defined as

$$w(z) = \frac{2}{\sqrt{\pi}}\int_0^\infty e^{2izt}e^{-t^2}dt\,, \tag{H.16}$$

for any complex number z. Physically, it has the meaning of a convolution of Gaussian and complex Lorentzian functions. In fact, for $\mathrm{Im}\, z > 0$, Eq. (H.16) is

equivalent to

$$w(z) = \frac{i}{\pi} \int_{-\infty}^{\infty} \frac{e^{-t^2}}{z-t}\, dt\,. \tag{H.17}$$

The Faddeeva function has the properties

$$w(-z) = 2e^{-z^2} - w(z) \quad \text{and} \quad [w(z)]^* = w(-z^*)\,, \tag{H.18}$$

and is linked to the error function $\mathrm{erf}(z)$ by

$$w(z) = e^{-z^2}\left[1 + \mathrm{erf}(iz)\right]\,, \tag{H.19}$$

where

$$\mathrm{erf}(z) = \frac{2}{\sqrt{\pi}} \int_0^z e^{-t^2} dt\,. \tag{H.20}$$

It can also be expressed in terms of the Dawson function $D(z)$ as

$$w(z) = e^{-z^2} + \frac{2i}{\sqrt{\pi}} D(z) \tag{H.21}$$

where

$$D(z) = \int_0^{\infty} e^{-t^2} \sin(2zt) dt = e^{-z^2} \int_0^z e^{t^2} dt\,. \tag{H.22}$$

Clearly, all three functions, $w(z)$, $\mathrm{erf}(iz)$, and $D(z)$, are equivalent in the sense that they can be expressed by each other. Analytically, the error function has an advantage that it is an entire function, so that $[\mathrm{erf}(z)]^* = \mathrm{erf}(z^*)$, in addition to being an odd function, $\mathrm{erf}(-z) = -\,\mathrm{erf}(z)$. However, numerically, the Faddeeva function (as well the Dawson function) is generally more accurate and stable, since the error function $\mathrm{erf}(z)$ diverges at large imaginary values of z, but the Faddeeva and Dawson functions do not.

The function $F(\alpha, \beta)$, introduced in Eq. (H.15) can also be written as

$$F(\alpha, \beta) = \frac{1}{2} \int_{-1}^{1} e^{\beta^2(1-x^2)} e^{2i\alpha\beta x} dx\,, \tag{H.23}$$

reflecting the integration over the polar angle in Eq. (H.13). It has the properties

$$F(\alpha,\beta) = F(-\alpha,\beta) = F(\alpha,-\beta) = F^*(\alpha,\beta)\,, \tag{H.24}$$

which are a easy to show using the definition Eq. (H.23), but can be obtained also from the analytic form Eq. (H.15) and the properties of the Faddeeva function, Eq. (H.18).

For $\alpha = 0$, corresponding to $d = 0$ in Eq. (H.14), one has

$$F(0,\beta) = \frac{\sqrt{\pi}}{4}\,\frac{w(-i\beta) - w(i\beta)}{\beta} = \frac{\sqrt{\pi}}{2}\,e^{\beta^2}\,\frac{\mathrm{erf}(\beta)}{\beta} \tag{H.25}$$

and in the limit $\beta \to 0$, corresponding to isotropic dots ($l_\perp = l$) or zero-frequency ($q = 0$),

$$\lim_{\beta\to 0} F(0,\beta) = 1\,, \tag{H.26}$$

so that Eq. (H.14) simplifies to Eq. (H.9).

In the isotropic limit ($l_\perp = l$), $\beta \to 0$ and $\alpha = qd/(2\beta) \to \infty$, and we obtain from Eq. (H.15)

$$\lim_{\beta\to 0} F\left(\frac{qd}{2\beta},\beta\right) = -\frac{\sqrt{\pi}}{4}\left(e^{iqd} - e^{-iqd}\right)\lim_{\beta\to 0}\frac{1}{\beta}w\left(\frac{qd}{2\beta}\right) = \mathrm{sinc}\,(qd)\,, \tag{H.27}$$

using

$$\lim_{z\to\infty} zw(z) = \lim_{z\to\infty}\frac{1}{\sqrt{\pi}}\int_0^\infty e^{iz'}\exp\left\{-\frac{z'^2}{2z^2}\right\}dz' = \frac{i}{\sqrt{\pi}} \tag{H.28}$$

with z'/z being real, as it follows from the definition Eq. (H.16), again, in agreement with Eq. (H.9).

Let us finally consider the limit of a strong anisotropy, $l \gg l_\perp$ which is used at the end of Sec. J.1.2 below. In this limit,

$$\alpha = \frac{d}{2\sqrt{l_\perp^2 - l^2}} \approx \frac{-id}{2l} \quad \text{and} \quad \beta = q\sqrt{l_\perp^2 - l^2} \approx iql\,, \tag{H.29}$$

with $2\alpha\beta = qd$. Under the condition that $|\alpha| \ll |\beta|$ (equivalent to $d \ll 2l^2q$) one can then obtain from Eq. (H.15)

$$\begin{aligned} F(0,\beta) - F(\alpha,\beta) &\approx -\frac{\sqrt{\pi}}{4iql}\left[(1-e^{iqd})w(-ql) - (1-e^{-iqd})w(ql)\right] \\ &= \frac{\sqrt{\pi}}{4iql}\left[4w(ql)\sin^2\frac{qd}{2} - (1-e^{iqd})e^{-q^2l^2}\right], \end{aligned} \tag{H.30}$$

using Eq. (H.18). Clearly, this function vanishes if $\sin(qd/2) = 0$. In the case of $ql \gg 1$ this simplifies to just

$$F(0,\beta) - F(\alpha,\beta) \approx \frac{\sqrt{\pi}}{iql} w(ql)\sin^2\frac{qd}{2} \approx \frac{1}{q^2l^2}\sin^2\frac{qd}{2}, \tag{H.31}$$

using the limit Eq. (H.28).

I Choosing the time step in the Trotter decomposition approach

The energy separation R between the hybridised states determines the timescale

$$\tau_0 = \frac{2\pi}{R}, \tag{I.1}$$

which is the period of the corresponding Rabi rotations. In the discretisation used in the LN approach described in Sec. 3.3.4, this timescale should be much larger than the time step Δt of discretisation, $\Delta t \ll \tau_0$. In the cavity-coupled two-qubit system, R can take three different values, and the above condition should be fulfilled for all of them. For example, at zero detuning ($\Omega_1 = \Omega_2 = \Omega_C$), the same coupling to the cavity ($g_1 = g_2 = \bar{g}$), and no dipolar coupling ($g = 0$), the largest energy separation is evaluated as $R = 2\sqrt{2}\bar{g}$, see the inset in Fig. 4.3. In the case of the dipolar coupled QDs without a cavity, there are only two hybridised states and therefore only one Rabi splitting, evaluated to $R = 2g$ at zero detuning ($\Omega_1 = \Omega_2$). At the same time, the polaron timescale τ_{IB} is given by [43]

$$\tau_{\mathrm{IB}} \approx \frac{\pi\sqrt{l^2 + l_\perp^2}}{v_s} \tag{I.2}$$

for anisotropic QDs with in-plane (l) and perpendicular ($l_\perp$) Gaussian lengths. The polaron timescale characterises the time to form or disperse a polaron cloud following the creation or destruction of an exciton in a QD. The selected time step Δt must be large enough such that for a given number of $L+1$ time steps within the memory kernel, the resulting memory time of $(L+1)\Delta t$ is larger than τ_{IB}. Specifically, the total time considered via the time steps must cover the dynamics of the cumulant $\mathcal{K}_{i_n i_m}$ defined in Eq.(3.3.19), which is dependent on the cumulant elements C_{11}, C_{12}, and C_{22}, with the full temporal evolution defined in Eq. (3.3.20).

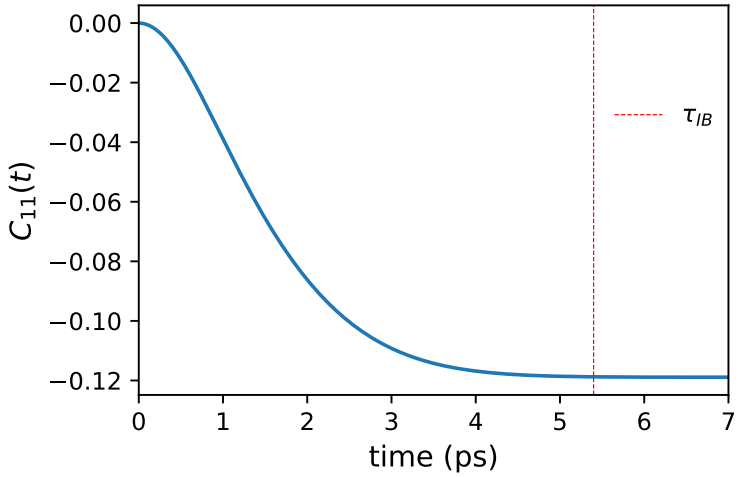

Figure I.1: Temporal evolution of $C_{11}(t)$ (blue line) and the phonon memory time τ_{IB} (vertical red dashed line). The parameters are as in Fig. 4.1(c) resulting in $\tau_{\mathrm{IB}} = 5.39\,\mathrm{ps}$.

Focusing on the cumulant element $C_{11}(t)$, we see from Fig. I.1 that $(L+1)\Delta t \geq \tau_{\mathrm{IB}}$ is in fact sufficient to fully cover the dynamics due to this element $C_{11}(t)$. In practice, however, one should perform a convergence test for the chosen parameters, to ensure the full memory time is taken into account. In the case of identical QDs, $C_{11}(t) = C_{22}(t)$, otherwise the larger τ_{IB} of the two QDs should be used. However since both QD excitons couple to the same phonons, there are extra cumulant elements $K_{12}(s)$ which depend on the distance d separating the QDs. The effect of this distance dependence is the introduction of a delay time before $C_{12}(t)$ starts to change, this can be seen in the inset of Fig. I.2. Physically this delay time is due to the time it takes a phonon to travel between the QDs, which is approximately d/v_s. For consistency, we define in the calculations the delay time

t_D to be the time at which $C_{12}(t)$ change is equal to a half of its minimum value, i.e. $C_{12}(t_D) = C_{12}(\infty)/2$. The values of t_D are shown in Fig. I.2 (red curve) as function of the interdot distance, along with its rough estimate d/v_s (red dashed line) working well at large distances.

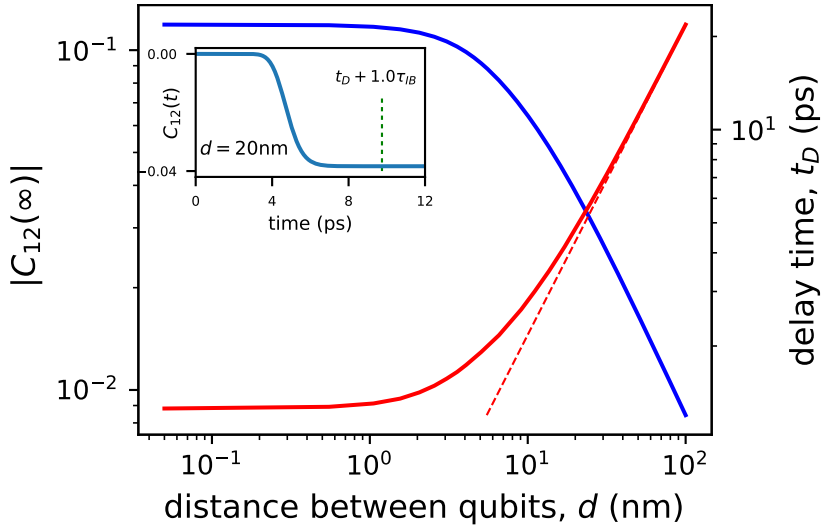

Figure I.2: The asymptotic value of $|C_{12}(t)|$ (blue line, left axis) and the delay time t_D (red line, right axis) as functions of the interdot distance d, with the red dashed line being the estimate d/v_s of the time taken for a phonon to travel between the QDs. The inset shows the temporal evolution of $B(t)$ at $d = 20\,\mathrm{nm}$, demonstrating the delay time, decay and saturation at a minimum value. The green vertical dashed line in the inset shows the full memory time considered. The parameters used are the same as in Fig. I.1.

The presence of the delay time t_D in the cumulant function $C_{12}(t)$ implies that the time step in discretisation must be increased to cover the full memory time of $C_{12}(t)$, so the condition $\Delta t = \tau_{\mathrm{IB}}/(L+1)$ suitable for a QD-cavity system [43] is no longer sufficient for distant coupled QDs with increasing QD separation d. We therefore modify this condition to

$$\Delta t = \frac{t_D + \tau_{\mathrm{IB}}}{L+1}\,, \tag{I.3}$$

which takes the delay time into account, thus covering the memory time for all cumulant elements. The green vertical dashed line in the inset of Fig. I.2 demonstrates that all changes of the cumulant functions, $C_{ij}(t)$, are covered over the memory time $\Delta t(L+1)$.

As the memory time increases due to the increase in delay time with increasing d, the accuracy of the calculation decreases for a given L due to the increase in time step. As seen from the inset, $C_{12}(t)$ saturates at a minimum value $C_{12}(\infty)$, and the blue line in Fig. I.2 shows the decrease of $|C_{12}(\infty)|$ as d increases, implying that $C_{12}(t) \to 0$ as $d \to \infty$. This means in the limit of $d \to \infty$, the full shared phonon bath calculation becomes equivalent to the independent bath case, which is naturally expected, whereby the result is now independent of the distance between the QDs and therefore $\Delta t = \tau_{\mathrm{IB}}/(L+1)$ is again sufficient since there is no delay time through the $K_{12}(s)$ cumulant elements.

J Fermi's golden rule

J.1 Fermi's golden rule: Dipolar coupled qubits

In this appendix, we apply a unitary transformation to the full Hamiltonian Eq. (3.2.1) of the system in *Case A*, considering two directly coupled QDs without cavity. Following this transformation, we use FGR to calculate the phonon-assisted transition rates between the hybridised QD states, as illustrated in Fig. J.1, and consequently the dephasing rates of the linear polarisation.

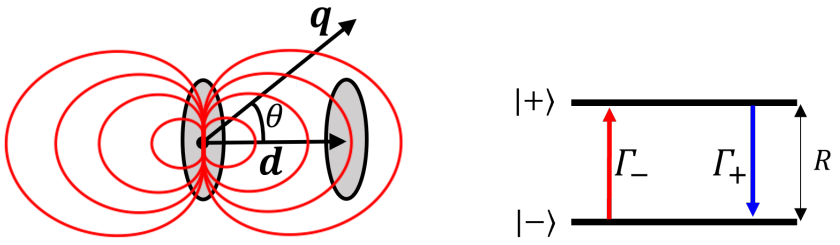

(a) (b)

Figure J.1: (a) Schematic of the system for a pair of dipole-dipole coupled anisotropic QDs separated by distance d and a phonon with the wave vector $\mathbf{q}$ emitted or absorbed at an angle θ (for clarity the dipole-dipole interaction is shown only for the left QD acting on the right QD). (b) Nonzero-detuning energy level diagram for the hybridised states $|\pm\rangle$ composed from the basis states $|1\rangle$ and $|2\rangle$ of isolated QDs. Red and blue arrows show phonon-assisted transitions between the hybridised states, resulting in the line broadening Γ_- and Γ_+ of the lower and upper states, respectively.

Let us consider the full Hamiltonian $H = H_0 + H_{\mathrm{IB}}$, defined in Eqs. (3.2.2) and

(3.2.3) with the cavity coupling $g_1 = g_2 = 0$. In the basis of pure QD states, $|1\rangle$ and $|2\rangle$, H_0 has the following matrix form

$$H_0 = \begin{pmatrix} \Omega_1 & g \\ g & \Omega_2 \end{pmatrix}. \tag{J.1}$$

This matrix can be diagonalised by a unitary transformation $S^\dagger H_0 S = \Lambda$, where

$$S = S^{-1} = S^\dagger = \begin{pmatrix} D_- & D_+ \\ D_+ & -D_- \end{pmatrix}, \tag{J.2}$$

with $D_\pm$ given by Eq. (4.2.4) and

$$\Lambda = \begin{pmatrix} \Omega_+ & 0 \\ 0 & \Omega_- \end{pmatrix} \tag{J.3}$$

being a diagonal matrix of the eigenvalues Eq. (4.2.7).

Applying this transformation to the full Hamiltonian, we obtain

$$\begin{aligned} \tilde{H} &= S^\dagger H S = \begin{pmatrix} \Omega_+ & 0 \\ 0 & \Omega_- \end{pmatrix} + \begin{pmatrix} D_- & D_+ \\ D_+ & -D_- \end{pmatrix} \begin{pmatrix} V_1 & 0 \\ 0 & V_2 \end{pmatrix} \begin{pmatrix} D_- & D_+ \\ D_+ & -D_- \end{pmatrix} + H_{\mathrm{ph}} \mathbb{1} \\ &= \begin{pmatrix} \Omega_+ + V_+ & V \\ V & \Omega_- + V_- \end{pmatrix} + H_{\mathrm{ph}} \mathbb{1}, \end{aligned} \tag{J.4}$$

with $V_\pm$ defined in Sec.4.2.2, and $\mathbb{1}$ is the 2×2 identity matrix. The main outcome of this transformation is the off-diagonal coupling to phonons given by $V = D_+ D_- (V_1 - V_2)$. This coupling is responsible for the phonon-assisted transitions between the hybridised states and ultimately for the long-time dephasing of the optical polarisation.

J.1.1 Isotropic QDs

Here we evaluate the rate Γ_{ph} in FGR Eq. (4.2.21) for isotropic QDs, substituting Eq. (H.5) into Eq. (4.2.22), converting the summation over $\mathbf{q}$ to an integration and

further expressing the integration in spherical coordinates, we find

$$\begin{aligned}\Gamma_{\rm ph} &= \frac{D_+^2 D_-^2 (D_c - D_v)^2}{8\pi\rho_m v_s} \int_0^\infty dq\, q^3 e^{-q^2 l^2} \\ &\times \int_0^\pi d\theta\, \sin(\theta)(2 - e^{iqd\cos\theta} - e^{-iqd\cos\theta})\delta(v_s q - R)\,,\end{aligned} \tag{J.5}$$

where $l^2 = (l_1^2 + l_2^2)/4$ (for identical QDs $l_1 = l_2 = l\sqrt{2}$). Integrating over θ, we obtain

$$\Gamma_{\rm ph} = \frac{D_+^2 D_-^2 (D_c - D_v)^2}{2\pi\rho_m v_s^5} R^3 e^{-\frac{R^2 l^2}{v_s^2}} \left[1 - \mathrm{sinc}\left(\frac{Rd}{v_s}\right)\right]. \tag{J.6}$$

In the case of zero detuning, $R = 2g$ and $D_+ = D_- = 1/\sqrt{2}$. In the limit of $d \to \infty$, $\mathrm{sinc}(Rd/v_s) \to 0$, so that $\Gamma_{\rm ph}$ becomes independent of d. In the limit of $d \to 0$, $\mathrm{sinc}(x) \approx 1 - x^2/6$, leading to a d^2 dependence at small distances and vanishing dephasing rates at $d = 0$.

Let us note also that for a 1D phonon bath which is for example the case of a QD embedded in a quantum wire, the latter providing a 2D quantum confinement of phonon modes, Eq. (4.2.22) would give instead, for the same coupling matrix element Eqs. (H.1) and (H.2) and the linear phonon dispersion $\omega = v_s q$, the following dependence on the Rabi splitting R and interdot distance d:

$$\Gamma_{\rm ph} \propto R\, e^{-\frac{R^2 l_\perp^2}{v_s^2}} \sin^2\left(\frac{Rd}{2v_s}\right), \tag{J.7}$$

where $l_\perp$ is the Gaussian length of the electron and hole confinement in the direction of the phonon propagation.

J.1.2 Anisotropic QDs

Performing a similar calculation for anisotropic QDs, we find, after substituting the exciton-phonon coupling element Eq. (H.12) into Eq. (4.2.22):

$$\begin{aligned}\Gamma_{\rm ph} &= \frac{D_+^2 D_-^2 (D_c - D_v)^2}{8\pi\rho_m v_s} \int_0^\infty dq\, q^3 \\ &\times \int_0^\pi d\theta\, \sin(\theta) e^{-q^2 l^2 \sin^2\theta} e^{-q^2 l_\perp^2 \cos^2\theta} \\ &\times \left(2 - e^{iqd\cos\theta} - e^{-iqd\cos\theta}\right)\delta(v_s q - R)\,,\end{aligned} \tag{J.8}$$

where $l^2 = (l_1^2 + l_2^2)/4$ and $l_\perp^2 = (l_{\perp,1}^2 + l_{\perp,2}^2)/4$ (for identical QDs $l_1 = l_2 = l\sqrt{2}$ and $l_{\perp,1} = l_{\perp,2} = l_\perp\sqrt{2}$). Performing the integration, we obtain

$$\Gamma_{\rm ph} = \frac{D_+^2 D_-^2 (D_c - D_v)^2}{2\pi\rho_m v_s^5} R^3 e^{-q^2 l_\perp^2} \left[F\left(0, q\sqrt{l_\perp^2 - l^2}\right) - F\left(\frac{d}{2\sqrt{l_\perp^2 - l^2}}, q\sqrt{l_\perp^2 - l^2}\right)\right], \tag{J.9}$$

where $q = R/v_s$ and the function $F(\alpha, \beta)$ is given by Eq. (H.15).

For strongly anisotropic QDs with $l \gg l_\perp$, $Rl/v_s \gg 1$ (small phonon wavelength) and $d \ll 2l^2 q$ ($|\alpha| \ll |\beta|$), we find using Eq. (H.31)

$$\Gamma_{\rm ph} = \frac{D_+^2 D_-^2 (D_c - D_v)^2}{2\pi\rho_m v_s^3} \frac{R}{l^2} e^{-\frac{R^2 l_\perp^2}{v_s^2}} \sin^2\left(\frac{Rd}{2v_s}\right), \tag{J.10}$$

which has the same dependence on the distance d and the Rabi splitting R as in the model of 1D phonons Eq. (J.7).

J.2 Fermi's golden rule: Cavity-mediated coupled qubits

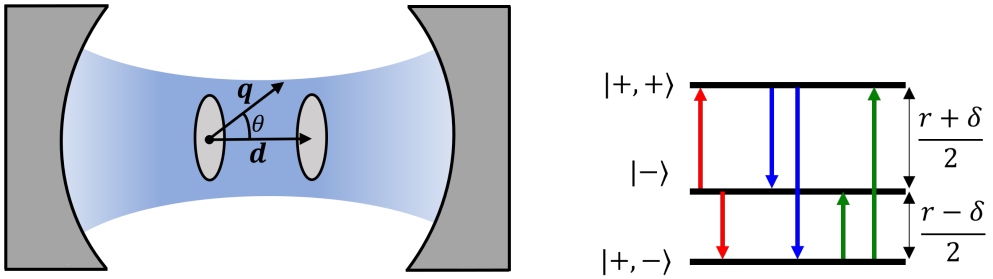

(a) (b)

Figure J.2: (a) Schematic of the system for a pair of anisotropic QDs separated by distance d each interacting independently with the cavity mode and a phonon with the wave vector $\mathbf{q}$ emitted or absorbed at an angle θ. (b) The $g_1 = g_2 = \bar{g}$ and nonzero-detuning ($\delta \neq 0$) energy level diagram for the hybridised states $|+,\pm\rangle$ and $|-\rangle$ composed from the basis of $|1\rangle$, $|2\rangle$ and $|C\rangle$, of the isolated QDs and the cavity with a single photon. The transitions indicated by the red, blue and green arrows result in the line broadening (dephasing rates) of the central, upper, and lower states, denoted by Γ_-, $\Gamma_{+,+}$, and $\Gamma_{+,-}$, respectively.

Let us now focus on the other special case (*Case B*) of no direct dipolar coupling

of two QD qubits, i.e. $g = 0$, but a indirect coupling mediated by their interaction with a common cavity mode with the coupling constants g_1 and g_2. Reducing the full basis to pure QD states, $|1\rangle$ and $|2\rangle$, and the single-photon cavity state $|C\rangle$, which is sufficient for the linear polarisation, the Hamiltonian of the cavity-mediated system takes the form

$$H = H_0 + V_1 |1\rangle \langle 1| + V_2 |2\rangle \langle 2| + H_{\text{ph}} \,, \tag{J.11}$$

where

$$\begin{aligned} H_0 \;=\; & \Omega_1 |1\rangle \langle 1| + \Omega_2 |2\rangle \langle 2| + \Omega_C |C\rangle \langle C| \\ & + g_1(|1\rangle \langle C| + |C\rangle \langle 1|) + g_2(|2\rangle \langle C| + |C\rangle \langle 2|) \,, \end{aligned} \tag{J.12}$$

and H_{ph} and V_i are given by Eq. (3.2.3). We apply a transformation diagonalising H_0 as $S^\dagger H_0 S = \Lambda$, so the full Hamiltonian transforms to

$$\begin{aligned} \tilde{H} \;&=\; S^\dagger H S \\ &=\; \mathbb{1} H_{\text{ph}} + S^\dagger \begin{pmatrix} \Omega_1 & 0 & g_1 \\ 0 & \Omega_2 & g_2 \\ g_1 & g_2 & \Omega_C \end{pmatrix} S + S^\dagger \begin{pmatrix} V_1 & 0 & 0 \\ 0 & V_2 & 0 \\ 0 & 0 & 0 \end{pmatrix} S \,, \end{aligned} \tag{J.13}$$

where $\mathbb{1}$ is the 3×3 identity matrix. In general, H_0 is diagonalised numerically, providing the hybridised state energy eigenvalues Λ_j. The transformation of the exciton-phonon coupling generates off-diagonal elements responsible for phonon-assisted transition between hybridised QD-cavity states which we account for below using FGR.

Focusing on the analytically solvable case of zero detuning between the QD qubit states, $\Omega_1 = \Omega_2 = \Omega$ (e.g. for identical qubits), and the same coupling of both qubits to the cavity, $g_1 = g_2 = \bar{g}$, the transformation matrix has the following

explicit form

$$S = \begin{pmatrix} d_- & \frac{1}{\sqrt{2}} & d_+ \\ d_- & -\frac{1}{\sqrt{2}} & d_+ \\ \sqrt{2}d_+ & 0 & -\sqrt{2}d_- \end{pmatrix}, \tag{J.14}$$

where

$$d_\pm = \frac{1}{2}\sqrt{1 \pm \frac{\delta}{r}} \tag{J.15}$$

with

$$r = \sqrt{\delta^2 + 8\bar{g}^2} \quad \text{and} \quad \delta = \Omega_C - \Omega\,, \tag{J.16}$$

the latter being the cavity-QD detuning. The Hamiltonian Eq. (J.11) then transforms to

$$\tilde{H} = S^\dagger H S = \mathbb{1} H_{\text{ph}} + \begin{pmatrix} \Omega + \frac{\delta+r}{2} + U_+ d_-^2 & \frac{U_- d_-}{\sqrt{2}} & U_+ d_+ d_- \\ \frac{U_- d_-}{\sqrt{2}} & \Omega + \frac{U_+}{2} & \frac{U_- d_+}{\sqrt{2}} \\ U_+ d_+ d_- & \frac{U_- d_+}{\sqrt{2}} & \Omega + \frac{\delta - r}{2} + U_+ d_+^2 \end{pmatrix}, \tag{J.17}$$

where $U_\pm = V_1 \pm V_2$. By applying this transformation, we go from the $|1\rangle$, $|2\rangle$, $|C\rangle$ basis to the hybridised state basis

$$\begin{aligned} |+,\pm\rangle &= d_\mp(|1\rangle + |2\rangle) \pm \sqrt{2} d_\mp |C\rangle\,, \\ |-\rangle &= (|1\rangle - |2\rangle)/\sqrt{2}\,, \end{aligned} \tag{J.18}$$

analogous to that in the polariton transformation of a qubit-cavity system outlined in [43]. Figure J.2 illustrates the level structure of the hybridised states for nonzero detuning ($\delta \neq 0$) and the phonon-assisted transitions due to the off-diagonal elements in Eq. (J.17). The rates of these transitions are estimated below via FGR, similar to Sec. 4.2.2:

$$\Gamma_{\uparrow,\pm} = N(R)\Gamma_{\text{ph},\pm} \quad \text{and} \quad \Gamma_{\downarrow,\pm} = (N(R)+1)\Gamma_{\text{ph},\pm}\,, \tag{J.19}$$

respectively, for the upwards and downwards transitions, where

$$\Gamma_{\text{ph},\pm} = \pi \sum_{\mathbf{q}} |c_0(\lambda_{\mathbf{q},1} \pm \lambda_{\mathbf{q},2})|^2 \delta(\omega - R)\,. \tag{J.20}$$

There are six possible transitions corresponding to the six off-diagonal matrix elements in Eq. (J.17). $N(R)$ is the Bose distribution function taken at the energy R, which is the separation of the energy levels of the mixes states involved in the transition and c_0 is the corresponding factor. These energy levels are given by $\Lambda_{+,\pm} = \Omega + (\delta \pm r)/2$ and $\Lambda_- = \Omega$, according to Eq. (J.17). In particular, for $|+,-\rangle \leftrightarrow |-\rangle$ transitions, $R = (r-\delta)/2$ and $c_0 = d_+/\sqrt{2}$; for $|-\rangle \leftrightarrow |+,+\rangle$ transitions, $R = (r+\delta)/2$ and $c_0 = d_-/\sqrt{2}$; finally, for $|+,-\rangle \leftrightarrow |+,+\rangle$ transitions, $R = r$ and $c_0 = d_+ d_-$. Note that for the phonon-assisted transitions between the neighbouring levels ($|+,-\rangle \leftrightarrow |-\rangle$ and $|-\rangle \leftrightarrow |+,+\rangle$), the exciton-phonon coupling matrix elements $\lambda_{\mathbf{q},j}$ contribute to Eq. (J.20) as a difference due to U_-, thus giving $\Gamma_{\mathrm{ph},-}$, and for transitions between the distant levels ($|+,-\rangle \leftrightarrow |+,+\rangle$) as a sum due to U_+, thus giving $\Gamma_{\mathrm{ph},+}$, see Eq. (J.17).

Using the same procedure as in Appendix J.1, we evaluate the transition rates Eq. (J.20) for identical isotropic and anisotropic QD cubits. For isotropic dots, Eq. (J.20) yields

$$\Gamma_{\mathrm{ph},\pm} = \frac{c_0^2 (D_c - D_v)^2}{2\pi\rho_m v_s^5} R^3 e^{-\frac{R^2 l^2}{v_s^2}} \left[1 \pm \mathrm{sinc}\left(\frac{Rd}{v_s}\right)\right], \tag{J.21}$$

where the difference to Eq. (J.6) are the constant factors, the energy distance R, and most importantly the presence of the $\pm$ sign before the sinc function, differentiating the neighbouring ($-$) and the distant ($+$) level transitions. Note that the contribution of the distant level transitions to the decoherence is typically less significant due to the factor $e^{-R^2 l^2/v_s^2}$ in which R^2 is four times larger (for zero detuning) than for the neighbouring level transitions. Similarly, for anisotropic QDs we find

$$\begin{aligned} \Gamma_{\mathrm{ph},\pm} \;=\; & \frac{c_0^2 (D_c - D_v)^2}{2\pi\rho_m v_s^5} R^3 e^{-q^2 l_\perp^2} \left[F\left(0, q\sqrt{l_\perp^2 - l^2}\right) \right. \\ & \left. \pm F\left(\frac{d}{4\sqrt{l_\perp^2 - l^2}}, q\sqrt{l_\perp^2 - l^2}\right) \right] \end{aligned} \tag{J.22}$$

with $q = R/v_s$.

Using Eq. (J.21) or Eq. (J.22) in combination with Eq. (J.19), the contribution to the line broadening for a specific phonon-assisted transition can be found. The line broadening $\Gamma_{+,\pm}$ and Γ_{-} of the hybridised states is the sum of the broadening by the two available transitions.

K Triexponential fit of the polarisation for cavity-mediated coupled QD qubits

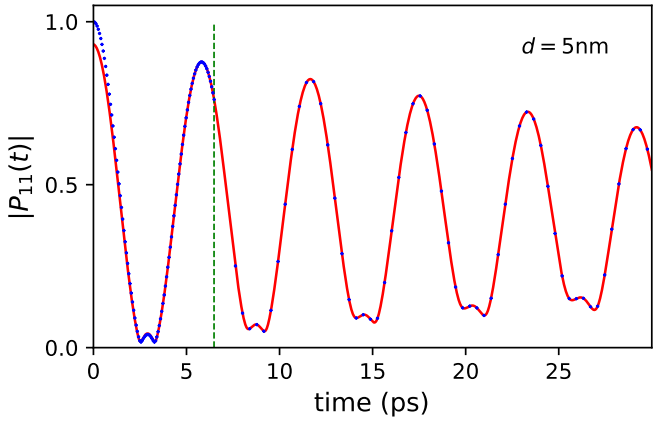

Figure K.1: Linear optical polarisation $|\mathrm{P}_{11}(t)|$ (blue dots) and its complex triexponential fit (red lines) for cavity mediated coupled anisotropic QD qubits at zero detuning, separated by a distance $d = 5\,\mathrm{nm}$, with excitation and measurement in QD 1. The parameters are as in Fig. 4.3 with $\bar{g} = 0.5\,\mathrm{meV}$.

We show in Fig. K.1 the optical linear polarisation $|\mathrm{P}_{11}(t)|$ for *Case B* in the main text. The linear polarisation (blue dots) for cavity-coupled QD qubits again starts from unity due to the excitation and measurement of the same QD state and have the temporal oscillations now at three frequencies due to addition of a cavity mode. We apply a complex triexponential fit (red curve) of the form $\sum_j C_j e^{-i\omega_j t}$, extracting the complex amplitudes C_j, energies Re ω_j, and dephasing rates $\Gamma_j = -\,\mathrm{Im}\,\omega_j$ of the phonon-dressed hybridised states. The fit is applied after the phonon-memory cut-off (dashed green vertical line), beyond the polaron cloud formation time. The dephasing rates are then extracted across a range of distances, providing Fig. 4.3.

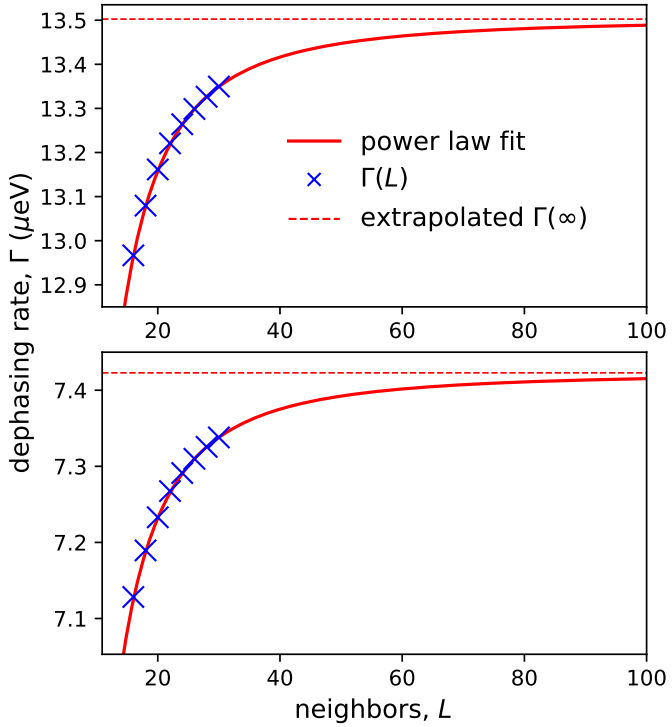

Figure L.1: Power law fit applied to the $\Gamma_+(L)$ ($\Gamma_-(L)$) values across a range of neighbours, L, for $d = 5\,\text{nm}$ is shown in the upper (lower) figure. The blue crosses are the extracted $\Gamma(L)$ values, the red curve is the power law model with $\beta = 2$, and the red horizontal dashed line is the estimated value of $\Gamma(\infty)$. The parameters are as in Fig. 4.1(b) with $T = 20\,\text{K}$.

L Extrapolation of fit parameters

As detailed in Sec. 5.6, Figs. 4.1 and 4.3 are created by calculating the linear optical polarisation for a given number of neighbours (L), then applying a fit to the long time data and extracting the fit parameters. The parameters corresponding to the line broadening, $\Gamma(L)$, are extracted across a range of neighbours, and the convergence of $\Gamma(L)$ to the exact ($L = \infty$) value is assumed to follow a power law model, given by,

$$\Gamma(L) = \Gamma(\infty) + CL^{-\beta}. \tag{L.1}$$

Fig. L.1 shows the $\Gamma(L)$ calculated values (blue crosses) for directly coupled QD qubits treated in *Case A*, with the power law model applied (red curve), and the extrapolated $\Gamma(\infty)$ is shown as a red dashed line. The value of $\Gamma(\infty)$ is estimated for the eight valued of $\Gamma(L)$ shown in Fig. 5.11, by minimising the root mean square

deviation from the power law Eq. (L.1) for $\beta = 2$.

Bibliography

[1] U. Woggon, "Optical properties of semiconductor quantum dots", Springer Tracts in Modern Physics Vol. 136 (Springer, Berlin ; New York, 1997).

[2] L. Jacak, P. Hawrylak, and A. Wójs, "Quantum dots" (Springer, Berlin ; New York, 1998).

[3] P. Michler, ed., "Single quantum dots: fundamentals, applications, and new concepts", Topics in Applied Physics Vol. 90 (Springer, Berlin Heidelberg, 2003).

[4] D. Bimberg, M. Grundmann, and N. N. Ledencov, "Quantum dot heterostructures", Reprinted (Wiley, Chichester, 2001).

[5] E. Flagg, A. Muller, S. Polyakov, A. Ling, A. Migdall, and G. Solomon, "Interference of Single Photons from Two Separate Semiconductor Quantum Dots", Phys. Rev. Lett. **104**, 137401 (2010).

[6] R. B. Patel, A. J. Bennett, I. Farrer, C. A. Nicoll, D. A. Ritchie, and A. J. Shields, "Two-photon interference of the emission from electrically tunable remote quantum dots", Nat. Phot. **4**, 632–635 (2010).

[7] L. Zhai, G. N. Nguyen, C. Spinnler, J. Ritzmann, M. C. Löbl, A. D. Wieck, A. Ludwig, A. Javadi, and R. J. Warburton, "Quantum interference of identical photons from remote GaAs quantum dots", Nat. Nanotechnol. **17**, 829–833 (2022).

[8] J. Majer, J. M. Chow, J. M. Gambetta, J. Koch, B. R. Johnson, J. A. Schreier, L. Frunzio, D. I. Schuster, A. A. Houck, A. Wallraff, A. Blais, M. H.

Devoret, S. M. Girvin, and R. J. Schoelkopf, "Coupling Superconducting Qubits via a Cavity Bus", Nature **449**, 443–447 (2007).

[9] A. Imamoglu, D. D. Awschalom, G. Burkard, D. P. DiVincenzo, D. Loss, M. Sherwin, and A. Small, "Quantum Information Processing Using Quantum Dot Spins and Cavity QED", Phys. Rev. Lett. **83**, 4204–4207 (1999).

[10] M. Delbecq, L. Bruhat, J. Viennot, S. Datta, A. Cottet, and T. Kontos, "Photon-mediated interaction between distant quantum dot circuits", Nat. Comm. **4**, 1400 (2013).

[11] G. Massimo Palma, K.-A. Suominen, and A. K. Ekert, "Quantum Computers and Dissipation", Proceedings of the Royal Society of London Series A **452**, 567–584 (1996).

[12] M. Schlosshauer, "Quantum decoherence", Physics Reports **831**, 1–57 (2019).

[13] B. Krummheuer, V. M. Axt, and T. Kuhn, "Theory of pure dephasing and the resulting absorption line shape in semiconductor quantum dots", Phys. Rev. B **65**, 195313 (2002).

[14] B. Krummheuer, V. M. Axt, T. Kuhn, I. D'Amico, and F. Rossi, "Pure dephasing and phonon dynamics in GaAs- and GaN-based quantum dot structures: Interplay between material parameters and geometry", Phys. Rev. B **71**, 235329 (2005).

[15] I. Wilson-Rae and A. Imamoglu, "Quantum Dot Cavity-QED in the Presence of Strong Electron-Phonon Interactions", Phys. Rev. B **65**, 235311 (2002).

[16] D. P. S. McCutcheon and A. Nazir, "Quantum dot Rabi rotations beyond the weak exciton-phonon coupling regime", New J. Phys. **12**, 113042 (2010).

[17] P. Kaer, T. R. Nielsen, P. Lodahl, A.-P. Jauho, and J. Mørk, "Non-Markovian Model of Photon-Assisted Dephasing by Electron-Phonon Interactions in a Coupled Quantum-Dot–Cavity System", Phys. Rev. Lett. **104**, 157401 (2010).

[18] U. Hohenester, A. Laucht, M. Kaniber, N. Hauke, A. Neumann, A. Mohtashami, M. Seliger, M. Bichler, and J. J. Finley, "Phonon-assisted tran-

sitions from quantum dot excitons to cavity photons", Phys. Rev. B **80**, 201311 (2009).

[19] U. Hohenester, "Cavity quantum electrodynamics with semiconductor quantum dots: Role of phonon-assisted cavity feeding", Phys. Rev. B **81**, 155303 (2010).

[20] C. Roy and S. Hughes, "Phonon-Dressed Mollow Triplet in the Regime of Cavity Quantum Electrodynamics: Excitation-Induced Dephasing and Nonperturbative Cavity Feeding Effects", Phys. Rev. Lett. **106**, 247403 (2011).

[21] K. H. Madsen, S. Ates, T. Lund-Hansen, A. Löffler, S. Reitzenstein, A. Forchel, and P. Lodahl, "Observation of Non-Markovian Dynamics of a Single Quantum Dot in a Micropillar Cavity", Phys. Rev. Lett. **106**, 233601 (2011).

[22] E. Stock, M.-R. Dachner, T. Warming, A. Schliwa, A. Lochmann, A. Hoffmann, A. I. Toropov, A. K. Bakarov, I. A. Derebezov, M. Richter, V. A. Haisler, A. Knorr, and D. Bimberg, "Acoustic and optical phonon scattering in a single In(Ga)As quantum dot", Phys. Rev. B **83**, 041304 (2011).

[23] M. Glässl, L. Sörgel, A. Vagov, M. D. Croitoru, T. Kuhn, and V. M. Axt, "Interaction of a quantum-dot cavity system with acoustic phonons: Stronger light-matter coupling can reduce the visibility of strong coupling effects", Phys. Rev. B **86**, 035319 (2012).

[24] A. Nazir and D. P. S. McCutcheon, "Modelling exciton–phonon interactions in optically driven quantum dots", J. Phys.: Condens. Matter **28**, 103002 (2016).

[25] G. Hornecker, A. Auffèves, and T. Grange, "Influence of phonons on solid-state cavity-QED investigated using nonequilibrium Green's functions", Phys. Rev. B **95**, 035404 (2017).

[26] M. Calic, P. Gallo, M. Felici, K. A. Atlasov, B. Dwir, A. Rudra, G. Biasiol, L. Sorba, G. Tarel, V. Savona, and E. Kapon, "Phonon-Mediated Coupling of InGaAs / GaAs Quantum-Dot Excitons to Photonic Crystal Cavities", Phys. Rev. Lett. **106**, 227402 (2011).

[27] D. Valente, J. Suffczyński, T. Jakubczyk, A. Dousse, A. Lemaître, I. Sagnes, L. Lanco, P. Voisin, A. Auffèves, and P. Senellart, "Frequency cavity pulling induced by a single semiconductor quantum dot", Phys. Rev. B **89**, 041302 (2014).

[28] F. Ishikawa, Y. Akamatsu, K. Watanabe, F. Uesugi, S. Asahina, U. Jahn, and S. Shimomura, "Metamorphic GaAs/GaAsBi Heterostructured Nanowires", Nano Lett. **15**, 7265–7272 (2015).

[29] K. Müller, K. A. Fischer, A. Rundquist, C. Dory, K. G. Lagoudakis, T. Sarmiento, Y. A. Kelaita, V. Borish, and J. Vučković, "Ultrafast Polariton-Phonon Dynamics of Strongly Coupled Quantum Dot-Nanocavity Systems", Phys. Rev. X **5**, 031006 (2015).

[30] D. E. Reiter, T. Kuhn, and V. M. Axt, "Distinctive characteristics of carrier-phonon interactions in optically driven semiconductor quantum dots", Advances in Physics: X **4**, 1655478 (2019).

[31] H. M. Cammack, P. Kirton, T. M. Stace, P. R. Eastham, J. Keeling, and B. W. Lovett, "Coherence protection in coupled quantum systems", Phys. Rev. A **97**, 022103 (2018).

[32] A. Strathearn, P. Kirton, D. Kilda, J. Keeling, and B. W. Lovett, "Efficient non-Markovian quantum dynamics using time-evolving matrix product operators", Nat. Comm. **9**, 3322 (2018).

[33] F. Grosse, E. A. Muljarov, and R. Zimmermann, "Phonons in Quantum Dots and Their Role in Exciton Dephasing", in *Semiconductor Nanostructures*, edited by P. Avouris, B. Bhushan, D. Bimberg, K. Von Klitzing, H. Sakaki, R. Wiesendanger, and D. Bimberg (Springer Berlin Heidelberg, Berlin, Heidelberg, 2008), pp. 165–187.

[34] J. Förstner, C. Weber, J. Danckwerts, and A. Knorr, "Phonon-Assisted Damping of Rabi Oscillations in Semiconductor Quantum Dots", Phys. Rev. Lett. **91**, 127401 (2003).

[35] D. E. Reiter, T. Kuhn, M. Glässl, and V. M. Axt, "The role of phonons for exciton and biexciton generation in an optically driven quantum dot", J. Phys.: Condens. Matter **26**, 423203 (2014).

[36] E. A. Muljarov and R. Zimmermann, "Exciton Dephasing in Quantum Dots due to LO-Phonon Coupling: An Exactly Solvable Model", Phys. Rev. Lett. **98**, 187401 (2007).

[37] E. A. Muljarov and R. Zimmermann, "Dephasing in Quantum Dots: Quadratic Coupling to Acoustic Phonons", Phys. Rev. Lett. **93**, 237401 (2004).

[38] P. Machnikowski, "Change of Decoherence Scenario and Appearance of Localization due to Reservoir Anharmonicity", Phys. Rev. Lett. **96**, 140405 (2006).

[39] R. Heitz, H. Born, F. Guffarth, O. Stier, A. Schliwa, A. Hoffmann, and D. Bimberg, "Existence of a phonon bottleneck for excitons in quantum dots", Phys. Rev. B **64**, 241305 (2001).

[40] J. Urayama, T. B. Norris, J. Singh, and P. Bhattacharya, "Observation of Phonon Bottleneck in Quantum Dot Electronic Relaxation", Phys. Rev. Lett. **86**, 4930–4933 (2001).

[41] L. Besombes, K. Kheng, L. Marsal, and H. Mariette, "Acoustic phonon broadening mechanism in single quantum dot emission", Phys. Rev. B **63**, 155307 (2001).

[42] P. Borri, W. Langbein, S. Schneider, U. Woggon, R. Sellin, D. Ouyang, and D. Bimberg, "Ultralong Dephasing Time in InGaAs Quantum Dots", Phys. Rev. Lett. **87**, 157401 (2001).

[43] A. Morreau and E. A. Muljarov, "Phonon-induced dephasing in quantum-dot–cavity QED", Phys. Rev. B **100**, 115309 (2019).

[44] L. S. Sirkina and E. A. Muljarov, "Impact of the phonon environment on the nonlinear quantum-dot–cavity QED: Path-integral approach", Phys. Rev. B **108**, 115312 (2023).

[45] L. M. J. Hall, L. S. Sirkina, A. Morreau, W. Langbein, and E. A. Muljarov, "Controlling dephasing of coupled qubits via shared-bath coherence", arXiv: `2405.14685` (cond-mat), (2024).

[46] E. A. Muljarov, T. Takagahara, and R. Zimmermann, "Phonon-Induced Exciton Dephasing in Quantum Dot Molecules", Phys. Rev. Lett. **95**, 177405 (2005).

[47] P. Zanardi and M. Rasetti, "Noiseless Quantum Codes", Phys. Rev. Lett. **79**, 3306–3309 (1997).

[48] D. A. Lidar, I. L. Chuang, and K. B. Whaley, "Decoherence-Free Subspaces for Quantum Computation", Phys. Rev. Lett. **81**, 2594–2597 (1998).

[49] P. Zanardi and F. Rossi, "Quantum Information in Semiconductors: Noiseless Encoding in a Quantum-Dot Array", Phys. Rev. Lett. **81**, 4752–4755 (1998).

[50] R. J. Glauber, "Coherent and Incoherent States of the Radiation Field", Phys. Rev. **131**, 2766–2788 (1963).

[51] E. Jaynes and F. Cummings, "Comparison of quantum and semiclassical radiation theories with application to the beam maser", Proc. IEEE **51**, 89–109 (1963).

[52] J. Kasprzak, S. Reitzenstein, E. A. Muljarov, C. Kistner, C. Schneider, M. Strauss, S. Höfling, A. Forchel, and W. Langbein, "Up on the Jaynes–Cummings ladder of a quantum-dot/microcavity system", Nat. Mat. **9**, 304–308 (2010).

[53] E. M. Purcell, "Spontaneous emission probabilities at radio frequencies", in *Confined electrons and photons*, Vol. 340, edited by E. Burstein and C. Weisbuch, Series Title: NATO ASI Series (Springer US, Boston, MA, 1995), pp. 839–839.

[54] G. D. Mahan, "Many-Particle Physics" (Springer US, Boston, MA, 2000).

[55] H.-P. Breuer and F. Petruccione, "The theory of open quantum systems" (Oxford University Press, Oxford ; New York, 2002).

[56] G. Lindwall, A. Wacker, C. Weber, and A. Knorr, "Zero-Phonon Linewidth and Phonon Satellites in the Optical Absorption of Nanowire-Based Quantum Dots", Phys. Rev. Lett. **99**, 087401 (2007).

[57] I. De Vega and D. Alonso, "Dynamics of non-Markovian open quantum systems", Rev. Mod. Phys. **89**, 015001 (2017).

[58] H.-P. Breuer, E.-M. Laine, J. Piilo, and B. Vacchini, "*Colloquium* : Non-Markovian dynamics in open quantum systems", Rev. Mod. Phys. **88**, 021002 (2016).

[59] A. J. Ramsay, A. V. Gopal, E. M. Gauger, A. Nazir, B. W. Lovett, A. M. Fox, and M. S. Skolnick, "Damping of Exciton Rabi Rotations by Acoustic Phonons in Optically Excited InGaAs / GaAs Quantum Dots", Phys. Rev. Lett. **104**, 017402 (2010).

[60] S. Hughes, P. Yao, F. Milde, A. Knorr, D. Dalacu, K. Mnaymneh, V. Sazonova, P. J. Poole, G. C. Aers, J. Lapointe, R. Cheriton, and R. L. Williams, "Influence of electron-acoustic phonon scattering on off-resonant cavity feeding within a strongly coupled quantum-dot cavity system", Phys. Rev. B **83**, 165313 (2011).

[61] R. P. Feynman and A. R. Hibbs, "Quantum mechanics and path integrals", International Series in Pure and Applied Physics (McGraw-Hill, New York, NY, 1995).

[62] D. E. Makarov and N. Makri, "Path integrals for dissipative systems by tensor multiplication. Condensed phase quantum dynamics for arbitrarily long time", Chem. Phys. Lett. **221**, 482–491 (1994).

[63] N. Makri and D. E. Makarov, "Tensor propagator for iterative quantum time evolution of reduced density matrices. I. Theory", J. Chem. Phys. **102**, 4600–4610 (1995).

[64] N. Makri and D. E. Makarov, "Tensor propagator for iterative quantum time evolution of reduced density matrices. II. Numerical methodology", J. Chem. Phys. **102**, 4611–4618 (1995).

[65] N. Makri, "Numerical path integral techniques for long time dynamics of quantum dissipative systems", J. Math. Phys. **36**, 2430–2457 (1995).

[66] J. Shao and N. Makri, "Iterative path integral calculation of quantum correlation functions for dissipative systems", Chem. Phys. **268**, 1–10 (2001).

[67] J. Shao and N. Makri, "Iterative path integral formulation of equilibrium correlation functions for quantum dissipative systems", J. Chem. Phys. **116**, 507–514 (2002).

[68] E. Sim and N. Makri, "Filtered propagator functional for iterative dynamics of quantum dissipative systems", Computer Physics Communications **99**, 335–354 (1997).

[69] E. Sim, "Quantum dynamics for a system coupled to slow baths: On-the-fly filtered propagator method", J. Chem. Phys. **115**, 4450–4456 (2001).

[70] R. Lambert and N. Makri, "Memory propagator matrix for long-time dissipative charge transfer dynamics", Mol. Phys. **110**, 1967–1975 (2012).

[71] L. Liu, J. Ren, and W. Fang, "Improved Memory Truncation Scheme for Quasi-Adiabatic Propagator Path Integral via Influence Functional Renormalization", arXiv: `2406.01978` (physics), (2024).

[72] M. Richter and B. P. Fingerhut, "Coarse-grained representation of the quasi adiabatic propagator path integral for the treatment of non-Markovian long-time bath memory", J. Chem. Phys. **146**, 214101 (2017).

[73] N. Makri, "Blip decomposition of the path integral: Exponential acceleration of real-time calculations on quantum dissipative systems", J. Chem. Phys. **141**, 134117 (2014).

[74] N. Makri, "Iterative blip-summed path integral for quantum dynamics in strongly dissipative environments", J. Chem. Phys. **146**, 134101 (2017).

[75] D. Gribben, A. Strathearn, J. Iles-Smith, D. Kilda, A. Nazir, B. W. Lovett, and P. Kirton, "Exact quantum dynamics in structured environments", Phys. Rev. Research **2**, 013265 (2020).

[76] G. E. Fux, P. Fowler-Wright, J. Beckles, E. P. Butler, P. R. Eastham, D. Gribben, J. Keeling, D. Kilda, P. Kirton, E. D. C. Lawrence, B. W. Lovett, E. O'Neill, A. Strathearn, and R. de Wit, "OQuPy: A Python package to efficiently simulate non-Markovian open quantum systems with process tensors", J. Chem. Phys. **161**, 124108 (2024).

[77] M. Cygorek and E. M. Gauger, "ACE: A general-purpose non-Markovian open quantum systems simulation toolkit based on process tensors", J. Chem. Phys. **161**, 074111 (2024).

[78] M. Richter and S. Hughes, "Enhanced TEMPO algorithm for quantum path integrals with off-diagonal system-bath coupling: applications to photonic quantum networks", Phys. Rev. Lett. **128**, 167403 (2022).

[79] L. S. Sirkina, L. M. J. Hall, A. Morreau, W. Langbein, and E. A. Muljarov, "Förster transfer between quantum dots in a shared phonon environment:

A rigorous approach, revealing the role of pure dephasing (In Preparation)", Unpublished.

[80] A. O. Govorov, "Spin-Förster transfer in optically excited quantum dots", Phys. Rev. B **71**, 155323 (2005).

[81] E. Rozbicki and P. Machnikowski, "Quantum Kinetic Theory of Phonon-Assisted Excitation Transfer in Quantum Dot Molecules", Phys. Rev. Lett. **100**, 027401 (2008).

[82] A. Thilagam and M. A. Lohe, "Decoherence of excitonic qubits in Förster coupled quantum dots", J. Phys.: Condens. Matter **20**, 315205 (2008).

[83] S. Reitzenstein, A. Löffler, C. Hofmann, A. Kubanek, M. Kamp, J. P. Reithmaier, A. Forchel, V. D. Kulakovskii, L. V. Keldysh, I. V. Ponomarev, and T. L. Reinecke, "Coherent photonic coupling of semiconductor quantum dots", Opt. Lett. **31**, 1738 (2006).

[84] F. Albert, K. Sivalertporn, J. Kasprzak, M. Strauß, C. Schneider, S. Höfling, M. Kamp, A. Forchel, S. Reitzenstein, E. Muljarov, and W. Langbein, "Microcavity controlled coupling of excitonic qubits", Nat. Comm. **4**, 1747 (2013).

[85] D. J. Van Woerkom, P. Scarlino, J. H. Ungerer, C. Müller, J. V. Koski, A. J. Landig, C. Reichl, W. Wegscheider, T. Ihn, K. Ensslin, and A. Wallraff, "Microwave Photon-Mediated Interactions between Semiconductor Qubits", Phys. Rev. X **8**, 041018 (2018).

[86] J. I. Climente, A. Bertoni, G. Goldoni, and E. Molinari, "Phonon-induced electron relaxation in weakly confined single and coupled quantum dots", Phys. Rev. B **74**, 035313 (2006).

[87] P. Nalbach, J. Eckel, and M. Thorwart, "Quantum coherent biomolecular energy transfer with spatially correlated fluctuations", New J. Phys. **12**, 065043 (2010).

[88] P. Kumar, C. Jennings, M. Scheibner, A. S. Bracker, S. G. Carter, and D. Gammon, "Spectral broadening of optical transitions at tunneling resonances in InAs/GaAs coupled quantum dot pairs", Phys. Rev. B **102**, 085423 (2020).

[89] V. N. Stavrou, "Spin qubits: spin relaxation in coupled quantum dots", J. Phys.: Condens. Matter **30**, 455301 (2018).

[90] V. Ardizzone, Y. Chassagneux, F. Vialla, G. Delport, C. Delcamp, N. Belabas, E. Deleporte, P. Roussignol, I. Robert-Philip, C. Voisin, and J. S. Lauret, "Strong reduction of exciton-phonon coupling in single-wall carbon nanotubes of high crystalline quality: Insight into broadening mechanisms and exciton localization", Phys. Rev. B **91**, 121410 (2015).

[91] A. Jeantet, Y. Chassagneux, T. Claude, P. Roussignol, J. S. Lauret, J. Reichel, and C. Voisin, "Exploiting One-Dimensional Exciton–Phonon Coupling for Tunable and Efficient Single-Photon Generation with a Carbon Nanotube", Nano Lett. **17**, 4184–4188 (2017).

[92] S. Lüker, T. Kuhn, and D. E. Reiter, "Phonon impact on optical control schemes of quantum dots: The role of quantum dot geometry and symmetry", Phys. Rev. B **96**, 245306 (2017).

[93] P. Zanardi and F. Rossi, "Subdecoherent information encoding in a quantum-dot array", Phys. Rev. B **59**, 8170–8181 (1999).

[94] A. W. Chin, J. Prior, R. Rosenbach, F. Caycedo-Soler, S. F. Huelga, and M. B. Plenio, "The role of non-equilibrium vibrational structures in electronic coherence and recoherence in pigment–protein complexes", Nat. Phys. **9**, 113–118 (2013).

[95] M. D. Rey, A. W. Chin, S. F. Huelga, and M. B. Plenio, "Exploiting Structured Environments for Efficient Energy Transfer: The Phonon Antenna Mechanism", J. Phys. Chem. Lett. **4**, 903–907 (2013).

[96] A. Blais, R.-S. Huang, A. Wallraff, S. M. Girvin, and R. J. Schoelkopf, "Cavity quantum electrodynamics for superconducting electrical circuits: An architecture for quantum computation", Phys. Rev. A **69**, 062320 (2004).

[97] H. Zheng and H. U. Baranger, "Persistent Quantum Beats and Long-Distance Entanglement from Waveguide-Mediated Interactions", Phys. Rev. Lett. **110**, 113601 (2013).

[98] I. Yeo, P.-L. De Assis, A. Gloppe, E. Dupont-Ferrier, P. Verlot, N. S. Malik, E. Dupuy, J. Claudon, J.-M. Gérard, A. Auffèves, G. Nogues, S. Seidelin,

J.-P. Poizat, O. Arcizet, and M. Richard, "Strain-mediated coupling in a quantum dot–mechanical oscillator hybrid system", Nat. Nanotechnol. **9**, 106–110 (2014).

[99] L. Childress, M. V. Gurudev Dutt, J. M. Taylor, A. S. Zibrov, F. Jelezko, J. Wrachtrup, P. R. Hemmer, and M. D. Lukin, "Coherent Dynamics of Coupled Electron and Nuclear Spin Qubits in Diamond", Science **314**, 281–285 (2006).

[100] E. A. Zibik, T. Grange, B. A. Carpenter, R. Ferreira, G. Bastard, N. Q. Vinh, P. J. Phillips, M. J. Steer, M. Hopkinson, J. W. Cockburn, M. S. Skolnick, and L. R. Wilson, "Intersublevel polaron dephasing in self-assembled quantum dots", Phys. Rev. B **77**, 041307 (2008).